Light Scattering Study of Highly Swollen Lyotropic Liquid Crystal

by

Chao-Yang Zhang
Alternative Name: Zhang Zhao

Submitted to the Department of Physics
in partial fulfillment of the requirements for the degree of

Doctor of Philosophy

at the

MASSACHUSETTS INSTITUTE OF TECHNOLOGY

January 1994

Author .....
Department of Physics
January 21 1994

Certified by .....
J. David Litster
Professor of Physics
Thesis Supervisor

Accepted by .....
George F. Koster
Chairman, Departmental Committee

Light Scattering Study of Highly Swollen Lyotropic Liquid Crystal

by

Chao-Yang Zhang

Alternative Name: Zhang Zhao

Submitted to the Department of Physics
on January 21 1994, in partial fulfillment of the
requirements for the degree of
Doctor of Philosophy

Abstract

We have conducted a dynamic light scattering study of the homeotropically aligned highly swollen lamellar phase (layer separation $d \sim$ 180nm) of a non-ionic binary system (C12E5/water) where the steric and entropic repulsion is the dominant inter-membrane force stabilizing the lamellar order. We have identified a hydrodynamic mode in the two momentum transfer limits available to light scattering. Based on previous models, we have found an explicit expression for the dispersion relation of this "baroclinic" or "slip" mode for systems with large layer spacing which successfully explains our experimental results. When d is large, the bilayer curvature elasticity and the viscous coupling between water and the bilayers become more important to the understanding of the baroclinic mode. We found the curvature elastic constant $k_c \simeq k_B T$, consistent with generally accepted values for flexible membranes.

We have successfully swelled lyotropic lamellar phase of OBS/pentnol/water/decane from $180nm$ to $1\mu m$ in layer spacing d, using a phase separation method. Moreover, each of these lamellar phases evolves into a continuous distribution of phases with different layer spacing when being put in a vertical container. By using Bragg powder light scattering, we found a linear dependence of the depth from the top of the fluid h vs. $1/d$. We interpret our finding as the result of force balance between gravity and the Helfrich interaction.

Furthermore, a layer spacing distribution over depth in one sample enables us to to measure consistently the Bragg peak lineshapes at different layer spacings. We have discussed the framework of the Landau-Peierls instability as applied to highly swollen lamellar phase, the effects of finite size and powder averaging and are able to fit our experimental data with a Kummer's function, which is a good approximation to describe the Landau-Peierls instability in our system. We find that the power law

exponent $\eta = 0.47 \pm 0.09$, independent of the layer spacing within our experimental accuracy, in the range of $d = 4000\mathring{A}$ to $d = 1\mu m$.

Finally, we have conducted dynamic light scattering near the Bragg peak at one layer spacing and find an approximate relation, $\omega \sim (q - q_0)^2$, where ω is the imaginary decay frequency of the dynamic process measured.

Thesis Supervisor: J. David Litster
Title: Professor of Physics

Acknowledgments

The years I have spent at MIT have been quite a learning and rewarding experience. I'd like to thank all the people who have contributed to this experience.

First, I want to express my thanks and appreciation to my advisor Prof. David Litster for his insightful guidance and active involvement in this research project. I also want to thank him for giving me the privilege to observe a truly effective leader at work. From him I have gained the courage to meet the challenges of difficult tasks, and to demand quality in all that I do. These are the most important lessons I have learned at MIT.

I would like to thank Dr. Sam Sprunt for teaching me many skills in doing condensed matter experiments, Prof. Sow-Hsin Chen for the many stimulating discussions at the early stage of my research project which were so crucial to me, and Prof. Mehran Kardar for his inspiring teaching of statistical mechanics, and much advice. Thanks to Don Heiman for his expert help with the experimental instruments and to George Nounesis for his frequent advice on career and life. I am indebted to Prof. Aron Bernstein who advised me in my first year of MIT research which I had enjoyed.

I also want to thank Peggy Berkovitz for her plentiful help since the first day I arrived in Cambridge about 5 years ago. Her fine personality and dedication to graduate students has made so many of us feel at home. Thanks to Irene Ferriabough and Magaret O'Meara for their excellent support at the Magnet Lab.

My MIT experience has been so much enriched, thanks to my office-mates, classmates and friends, Lou, Brian, Reiko, Mark, Lushalan and Gervais. Thanks to Tom Chen for the many discussions on research from which I have benefited; thanks to Chinghua, Qin, Dezhen, Zhaohui, Yongqing, Yongmei, Canwen, Yong, Bernadette, my sister Jing and many of my Chinese friends who have made my life away from my homeland so wonderful.

Finally I want to dedicate my work at MIT to my father Zhang Hongbin and

mother Li Ming who are always the happiest persons in the world for any of my accomplishments. I am grateful to my parents for teaching me the value of learning and for motivating me to excel at an early age, and for their deep, self-less love throughout my life.

To my parents

and

To my motherland

Approach is the moment of truth.

J. D. Litster

Experimental physics is not only
about knowledge and intuition,
but also about craftsmanship.

the author

Contents

List of Figures

Chapter 1

What We Have Accomplished in This Thesis Research

At the beginning of this thesis we will have an overview about the goals we have accomplished in this thesis research. We will answer questions like: 'What new understandings have you gained about lyotropic liquid crystals through your research?'; 'What have you found?'; Or 'What is the significance of your research?'.

1.1 The First Result: Sample Making

The first goal we accomplished is: we have made two highly swollen samples. Highly swollen lyotropic liquid crystals are relatively a new class of liquid crystal structures that have been discovered only in recent years. The phase diagrams are not well established. In addition, their dilute nature makes them much less stable and more difficult to align than conventional thermotropic or lyotropic liquid crystals. Sometimes it takes a lot of work simply to reproduce a sample whose phase diagram has already been published.

Based on Strey *et al.*'s phase diagram [1], we have been able to make an oriented C12E5/Water lamellar phase of layer spacing $d \sim 1800\mathring{A}$. The evidence of lamellar order is that the phase can have high magnetic birefringence but at the same time can be aligned to have optical distinction under a cross-polarized microscope. We found a method of avoiding phase separation and quickly aligning the sample.

Based on the work of Larche *et al.* [10], we obtained a non-oriented lamellar phase of 4-component OBS system with layer spacing d from $1800\mathring{A}$ to $1\mu m$. We used a phase separation method which is a little different from the method of Larche *et al.*'s. Larche *et al.*'s system has a maximum layer spacing $d \sim 6000\mathring{A}$. We were able to see brilliant color and beautiful Bragg ring from these lamellar phases as the absolute evidence of lamellar order up to this large scale.

Moreover, we discovered for the first time a layer spacing distribution in a column cell of the OBS lamellar liquid.

Our 'hands-on' experiences and experimental realizations of the two highly swollen lamellar phases, especially the OBS system, open a new avenue for more systematic and thoroughly conducted research in this direction for the MIT lyotropic liquid crystal research.

1.2 The Second Result: Confirmation of Helfrich Interaction

We have tested the Hefrich formulation of membrane-membrane interaction in highly swollen systems in several ways.

In experiments of C12E5 and water system, Helfrich formulation combined with Brochard and de Gennes's hydrodynamic model [7] of lipid-water system can explain our dynamic light scattering results. This part of work has been published in Ref. [22].

In experiments of the OBS system, Helfrich interaction is related to an external force (gravity) to explain the observed layer spacing distribution. Finally, in the Bragg peak measurements, the calculated power law exponent η based on the Helfrich interaction is expected to be independent of the layer spacing. This is approximately confirmed.

1.3 The Third Result: Dynamic and Static Behaviors of Highly Swollen Lamellar Phase

In the courses of analyzing our experiments, we have gained new understandings of the dynamic and static behaviors of highly swollen lamellar system. We have extended the Brochard and de Gennes' hydrodynamic model in describing the thermal fluctuations of largely spaced membrane system and applied the model to the C12E5/Water system to study the baroclinic mode of this system. We found $k_c \simeq k_B T$, consistent with generally accepted values for flexible membranes.

We have reconfirmed the Bragg peak lineshape due to the combined effect of the Landau-Peierls instability, the finite size and the powder averaging in the powder sample of the OBS system, with layer spacing ranging from $4000\mathring{A}$ to $1\mu m$.

Finally, we have conducted dynamic light scattering near the Bragg peak and find that the imaginary decay frequency $\omega \sim (q - q_0)^2$.

1.4 Research in Perspective

First of all, the structures of the OBS system need to be further investigated. What kind of lamellar phases are they? Do they look like 'onions'? What exactly are their sizes? What are the boundaries of the lamellar pieces like?

Secondly, we should be able to obtain oriented OBS sample fairly easily. With an aligned sample, both the static intensity measurement of the Bragg peak and the dynamic light scattering near Bragg peak will be very interesting.

Finally, experiments can also be conducted in high magnetic field which is available in the Francis Bitter National Magnet Lab. The large magnetic susceptibility of OBS molecule (which contains a benzane ring) makes the high field experiment more desirable. Magnetic field can serve as a controlled external parameter in studying the thermal fluctuations of the OBS system.

Chapter 2

Introduction to Complex Fluid

The basic building block of our system is a surfactant molecule with a polar head group and a hydro-carbon tail group as shown in Fig. 2-1. When being put in water, the atoms in the head group that have strong negative electric affinity such as oxygen atoms or nitrogen atoms tend to form hydrogen bonds with hydrogen atoms of water. On the other hand, the hydrocarbon tail can not form such bonds with the water molecules; the existing hydrogen bonds of water have to be bent to leave extra room for the tail to stay in water. So the energy cost for the head group staying in water is much less than that for the tail group. If there is an interface between water and oil (whose molecular structure is similar to the hydrocarbon tail), the surfactant molecules tend to stay in the interface with their head groups in the water side and their tails sticking to the oil side to keep the free energy of the whole system the lowest. So the head group is *hydrophilic* and the tail group is *hydrophobic*. Furthermore, since the hydrogen bond energy depends on temperature, both the *hydrophilicity* and *hydrophobicity* depend very much on temperature. Therefore, depending on the molecular types, temperature and compositions of the phase, surfactants can form various complex structures in solutions. These structures have defined a new field of

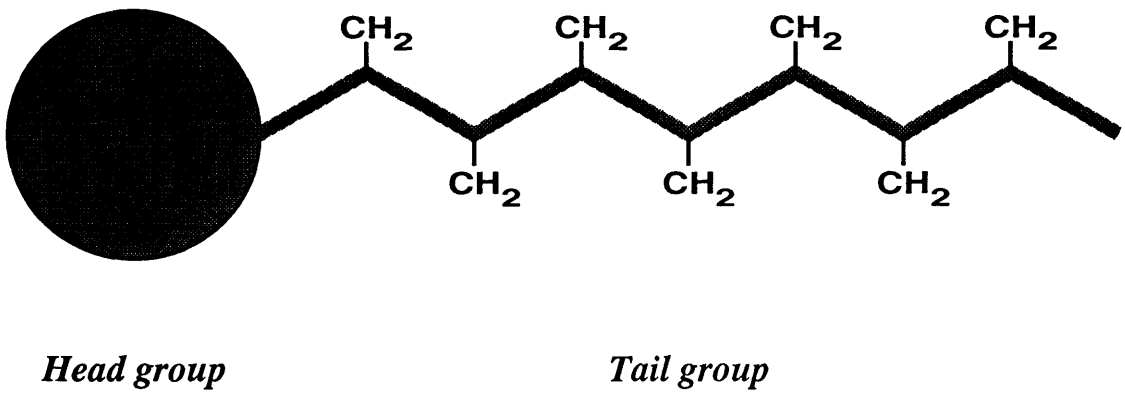

Figure 2-1: A sketch of a surfactant molecule

research called *complex fluid.* In the following paragraphs, we will have a brief tour in the field of complex fluid using some specific examples.

A typical non-ionic surfactant used in our experiment is dodecylpentoglycol(C12E5). Its molecular properties are listed in Appendix A . It is non-ionic in the sense that the head group does not contain ionic particles. First, let us examine the structures of C12E5/water binary system. Its phase diagram is shown in Fig 2-2. At low concentration, the surfactants can aggregate into spherical or cylindrical objects called micelles where the tail groups hide themselves inside micelles to reduce their exposure to water (see Fig. 2-3). Although the entropy of a solution in micellar form is less than that of a solution with free swimming surfactants, the lower energy cost of micellar state make it a more favorable state for the system to stay. Micelle is a relatively loose structures because surfactant molecules in a micelle constantly exchange positions with those free in solution; the system is in a dynamic equilibrium. At another

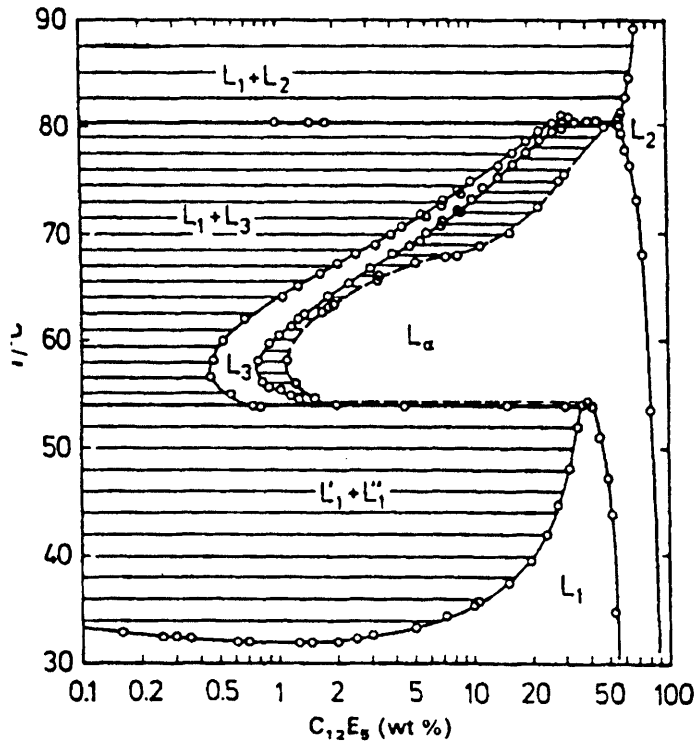

Figure 2-2: C12E5/water phase diagram (from Strey*et al.*[1])

region of the phase diagram (Fig. 2-2), surfactants forms bilayers to squeeze water out of the interiors of the bilayers and these bilayers stack to a lamellar structure called L_α phase that can have layer spacing up to several thousands angstroms (see Fig. 3-1 in Chapter 3). A close neighbor of the L_α phase is the L_3 phase. Instead of stacking to a lamellar structure, the bilayers curve up to form an isotropic, non-birefringent phase that is believed to be of connected cubic structures [3]. Fig. 2-4 shows a schematic visualization of the L_3 topology.

For ternary system of C12E5/water/decane (or a 4-component system when co-surfactants are added), analogies can be drawn to corresponding structures in the two component system. Microemulsions are similar to, but more stable than micelles. Three component lamellar phase is much like the binary lamellar phase except that

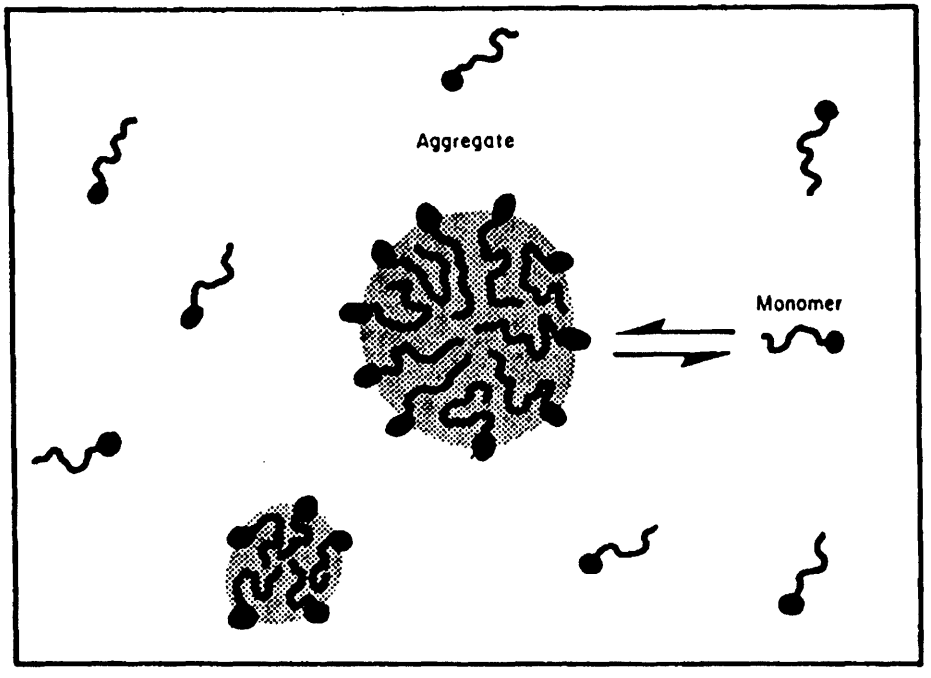

Figure 2-3: Micellar solution (from [2])

it can be swelled both by water and by oil (called inversely swelling). Bicontinuous phase resembles the L_3 phase except that the symmetry regarding the two sides of the layers is not conserved.

Vesicles are another interesting neighbor of L_α phase. A vesicle comprises one or several bilayers surrounding a pocket of fluid (see Fig.2-5). It is the closest resemblance of a living cell thus of the most biological importance among the complex fluid members. The volume ratio of head to tail is often crucial to the formation of vesicles. Vesicles made of C12E5 molecules have not been observed. In Chapter 5, we come across one kind of vesicle made of SDBS, CTAT and water[5].

A more recently discovered structure is tubules that can be as long as $1\mu m$. The wall of the tubes is of bilayer structures.

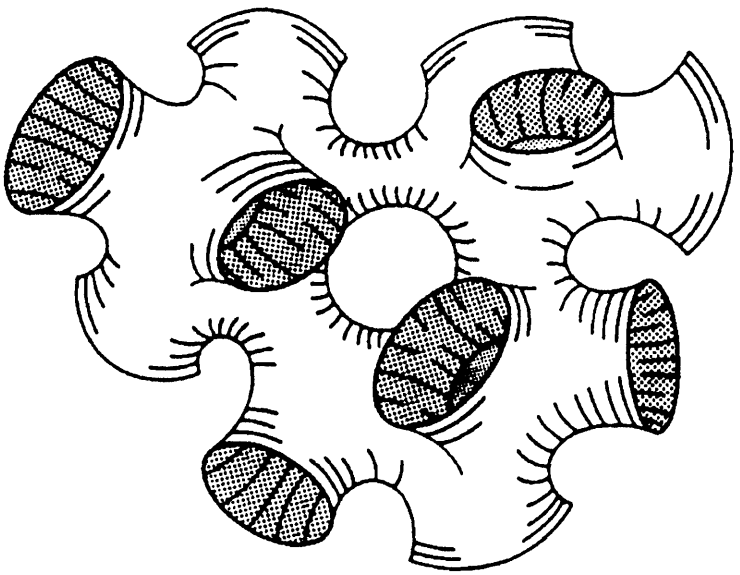

Figure 2-4: L_3 topology (from [4])

It is clear that membranes (mostly bilayers) are important components in many of the complex fluid structures and widely exist in biological system. From a physics point of view, membranes provide a good system to test certain law of physics

Our goal of research was to study the most regular phase of complex fluid, the lamellar phase (also called neat phase) in its highly swollen range, thus to gain knowledge about the properties of membranes and the interaction mechanism between them in this phase. These knowledge can be applied to other membrane structures such as vesicles and tubules.

As results, we have been able to obtain experimentally two highly swollen lamellar phases, an oriented C12E5/Water system with layer spacing $d \sim 1800\mathring{A}$ and a non-oriented OBS/pentanol/water/decane system, with $d \sim 1800\mathring{A}$ to $1\mu m$. The OBS

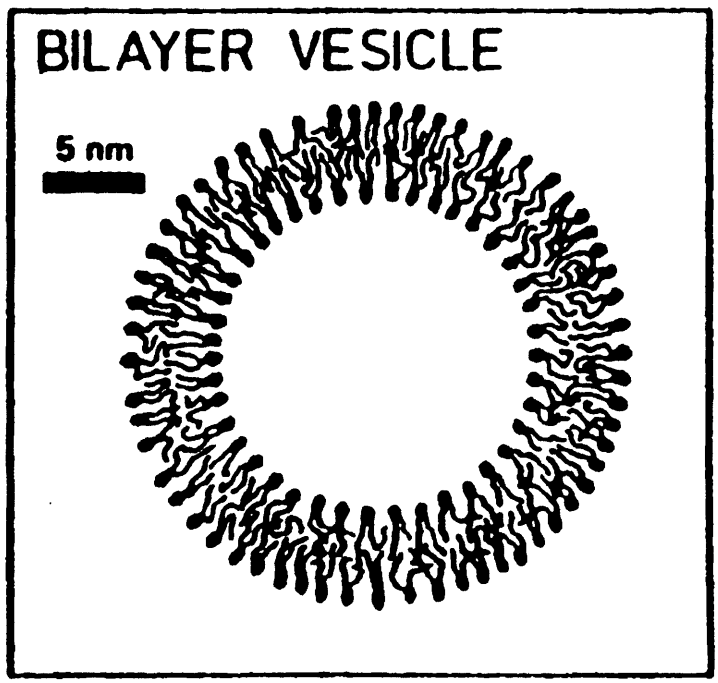

Figure 2-5: Vesicle (from [2])

system is a inversely swollen lamellar phase with oil (decane) as its diluent.

In the first system, we did dynamic light scattering from a well aligned sample on a vertical scattering geometry. We identified a hydrodynamic mode in the two momentum transfer limits available to light scattering and conclude that the hydrodynamic model of Brochard and de Gennes [7] combined with Helfrich interaction [6] mechanism can be applied to this highly swollen system. We also illustrated more important roles of the bilayer curvature elasticity and the viscous coupling between water and the bilayers in this swollen range.

In the second system, with layer spacings matching the wavelength of visible light, we were able to see the Bragg powder ring with light. This is a direct evidence of the lamellar order. Being able to measure precisely the layer spacing, We found that the

OBS lamellar phase evolved into a continuous distribution of subphases with varying layer spacings when being put in a vertical container. There is a linear dependence of $1/d$ on the depth h of the subphase from the top of the fluid. We attempted to explain this dependence as the result of gravitational compression. This layer spacing distribution over depth in a single sample also enabled us to measure consistently the Bragg peak as d changes. We confirmed the Bragg peak lineshapes due to the Landau-Peierls instability[8] for powder sample with layer spacings from $4000\mathring{A}$ to $1\mu m$.

Led by Dr. Sam Sprunt, we have conducted birefringence study of C12E5/water/octane microemulsion and lamellar to L_3 phase transition in high magnetic field. This part of work is not included in this thesis. It is being published.

The outline of this thesis is: In Chapter 3, we will describe the experimental procedures to make the above mentioned two kinds of lamellar phases. In Chapter 4, we will discuss the Helfrich formulation of layer-layer interaction and the hydrodynamics based on Brochard and de Gennes' model. In Chapter 5, we will discuss the basics of dynamic light scattering and the scattering results from solutions of polystyrene latex sphere and vesicles using a vertical light scattering setup. In Chapter 6 we will discuss the light scattering results from the C12E5/water system using the vertical setup. In Chapter 7, we will discuss the layer spacing distribution of the OBS system and the Bragg peak lineshapes due to Landau-Peierls instability in layered structure system.

Chapter 3

The Making of Lamellar Phases

3.1 C12E5/Water System

In this section we will have a close examination of the phase behavior of the binary system of C12E5/Water system, based on the previous work of Strey *et al.* [1], and discuss our experiences in making this highly swollen lamellar phase.

3.1.1 Phase Behavior

The phase diagram of C12E5/Water has been studied by Strey *et al.* and is shown in Fig. 2-2. They find that lamellar structure can exist at dilution as high as 99 wt.% water, yielding a lamellar phase with layer spacing d exceeding 3000$\mathring{A}$. A sketch of the structure of C12E5/water lamellar phase is shown in Fig. 3-1. The surfactants form bilayers with thickness ζ=3.75nm [1]; geometrically, d is determined by the surfactant volume fraction ϕ according to the simple relation:

$$d \simeq \frac{\zeta}{\phi} \tag{3.1}$$

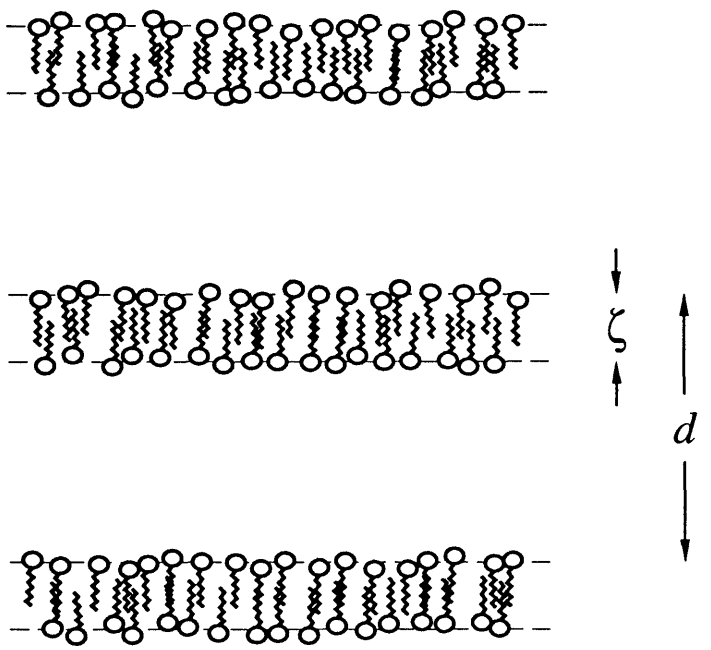

Figure 3-1: A sketch of the structure of a binary lamellar phase

The C12E5 we used was obtained from Fluka and used without further purification. The water was triply distilled. Observations under microscope for several samples ranging from 1.5 wt.% to 7 wt.% surfactant basically match Strey *et al.*'s phase diagram.

Take a sample of 2 wt.% C12E5 and 98 wt.% water for example. At room temperature, sample looks isotropic and transparent, there is no birefringence under cross polarizer. It is believed to be in micellar phase. As we raise temperature slowly to T = 31 C°, clouds appear. The phase is experiencing phase separation. The clouds consist of numerous small droplets of a new phase emerging from the background of the older phase. As temperature gets higher, droplets get larger, the two phases

separate macroscopically. Both phases show no birefringence under cross polarizers. They co-exist until T = 53 C°. These two phases are designated by Strey *et al.* as L_1' and L_1''. As T is higher than $53\,C°$, they tend to rejoin each other and form lamellar clusters that have strong birefringence (dark and white texture under cross polarizer). This rejoining process takes a long time and the resulting lamellar phase is not uniform at all. It often happens that certain regions have a higher concentration of C12E5 than its neighbors and form local metastable phases with unknown concentrations. This cause problems when we want to get uniformly aligned lamellar phase. We will discuss a way to solve this problem in the next section. These lamellar pieces are kept until T = 61 C°. Right above this temperature, they start to melt into a isotropic, non-birefringent liquid. This is the L_3 phase, about 3 C° wide. When temperature reaches 65 C°, clouds appear again, similar to the earlier clouds. This indicates that L_1 phase is emerging from the background of L_3 phase.

3.1.2 Sample Cell and Temperature Control

The sample cell is made of two fused silica windows separated by a $0.4mm$ teflon spacer which also serves as a gasket to seal the cell (see Fig. 3-2). The shaded area in Fig. 3-2 is the cross section of stainless steel (which is non-magnetic for future experiments in the magnetic field) container which serves to hold the windows together. The stainless steel container is in direct contact with the walls of our light scattering oven. The oven is electrically heated through a feedback bridge circuit so that the resistance of a high precision thermistor is compared with a pre-set value of another resistor for the desired temperature. A third ultra stable precision thermistor provides a separate measurement of the actual temperature inside the oven. This measurement is pre-calibrated with a standard quarts thermometer. The temperature measured by the quartz thermometer should be related to the resistance of the third

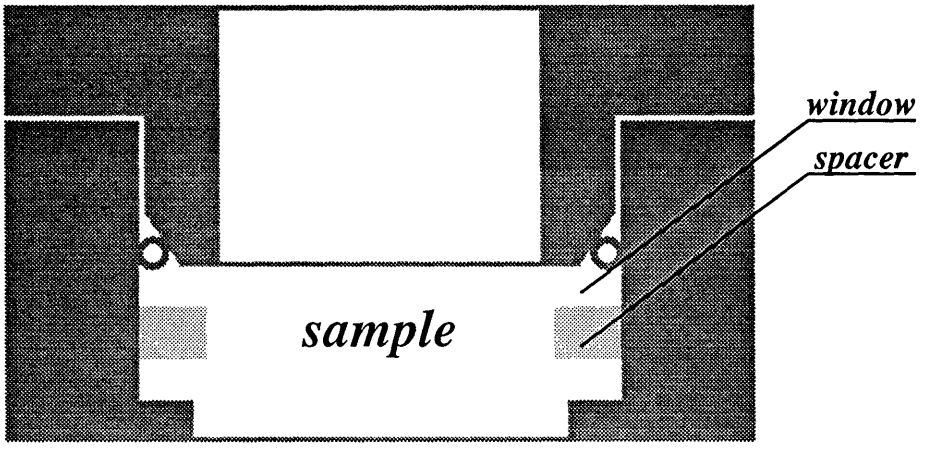

Figure 3-2: Cell used to make C12E5 sample andto do light scattering experiment

thermistor by,

$$T = [a_0 + a_1 log\,(R)]^{-1} + a_2\,[log\,(R)]^2 + a_3\,[log\,(R)]^3 - 273.15 \qquad (3.2)$$

where T is in $C°$, R is in *ohms*. a_0, a_1, a_2, a_3 are found by fitting the measured data using the above equation. The fit is shown in Fig.3-3. It should be emphasized that the coefficients depend on the structure of the oven and the effectiveness of the insulation. So, new calibration should be conducted for oven under new conditions, even though the ultra-stable thermistor is still the same.

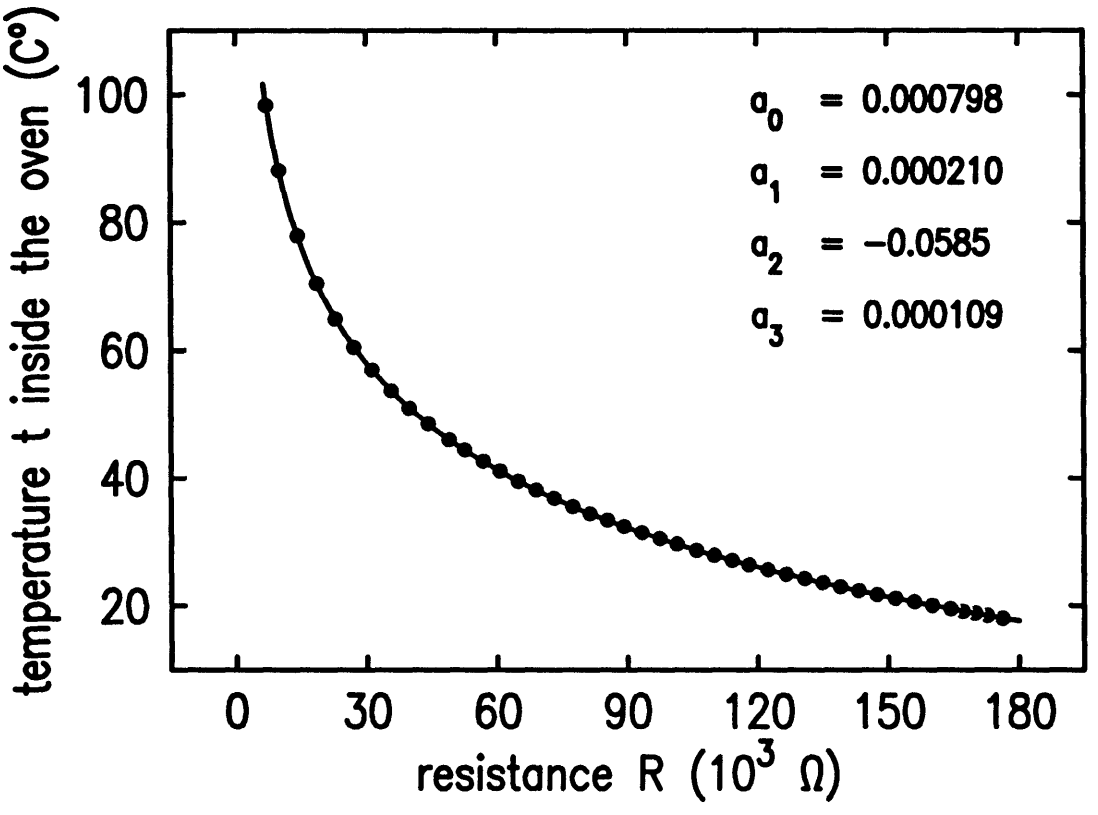

Figure 3-3: Oven temperature calibration from a quarts thermometer

3.1.3 Making a Uniformly Aligned Lamellar Phase

To get uniformly aligned lamellar phase, we use a what we call temperature "shock" and "cycling" treatment. We load the 2 wt.% sample to the cell at room temperature, and bring T suddenly to T = 57 C°, so that the sample skips the $L_1' + L_1''$ region as quickly as possible not to cause macroscopic phase separation. Local phase separation does occur, but they quickly rejoin each other and forms lamellar texture with non-uniform region much smaller than that in the slow process described in the last section. Then we allow the sample to stay in this L_α phase to equilibrate for 24 hrs. Under cross polarizers, we see evenly spreaded dark/white textures. The white region are the region where the lamellar layers are not completely aligned along the silica plates.

Finally, the sample is brought to the narrow isotropic L_3 region and is slowly cooled (0.1 C°/minute) back to the L_α phase. This final process can be done more than once, until we see uniform darkness under microscope and cross polarizers, well aligned L_α is finally achieved. The whole process is done with the cell being put horizontally, so that gravity plays the minimum role in phase separation. In the following chapters on light scattering from this phase, the scattering plane has to be vertical to satisfy this requirement for sample position.

The layer spacing d is slightly larger than calculated from Eq. (3.1) according to Strey *et al.*. They claims that thermally induced undulations of bilayers cause the increase of average layer spacing. The increased average layer spacing of 2 wt. % sample is estimated to be 1800$\mathring{A}$.

3.2 OBS/Pentanol/Water/Decane System

Sodium p-benzenesulfonate (OBS) is an ionic surfactant which can be used to form lyotropic liquid crystals together with long chain alcohol molecules (e.g. pentanol) and water. According to Marignan *et al.* [9], the lamellar liquid crystal which contains, by weight, 39.5% OBS, 18% pentanol, and 42.5% water has a layer spacing 35$\mathring{A}$. According to Larche *et al.*[10, 11], it can be swollen by a diluent of 92% decane and 8% pentanol by weight, up to 0.7% volume fraction of the initial liquid crystal, yet still keeps its smectic order. This corresponds to a maximum layer spacing of 6000$\mathring{A}$. Fig. 3-4 show the structure of this inversely swollen lamellar phase. Our goal is to obtain a lamellar phase with layer spacing greater than 3000$\mathring{A}$ so that light scattering can be used to study the Bragg peak. First, we calculated the weight percentage of each component to make a sample of desired layer spacing of several thousands anstroms based on the recipe of Ref [11]. Then we put the four components needed into a bottle at room temperature (25 $C°$). OBS was 4-benzenesulfonate obtained

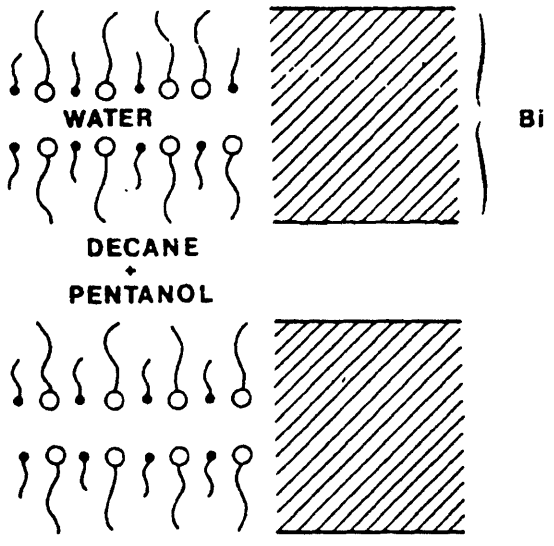

Figure 3-4: Inversely swollen OBS lamellar structure (from Larche *et al.*[11])

from Aldrich Chem. Co. (98% pure). Water was triply distilled, 1-pentanol(99% pure) and decane(98% pure) are both from Fluka. But we could not get a lamellar phase, because after being mixed thoroughly, there appeared many colorful strips. These strips are the crystallizations of OBS together with small amount of water and pentanol.

Then we tried to swell the original liquid crystal step by step, using the same diluent of decane/pentanol as Ref [10]. We found that at least from 20 to 50 times volume swelling, the mixture tends to have phase separation into two phases, an upper transparent phase and a lower non-transparent white phase. The upper phase is proved to be lamellar phase by Bragg light scattering. This phenomenon can be qualitatively understood from the phase triangle in Fig. 3-5 quoted from Ref. [12]

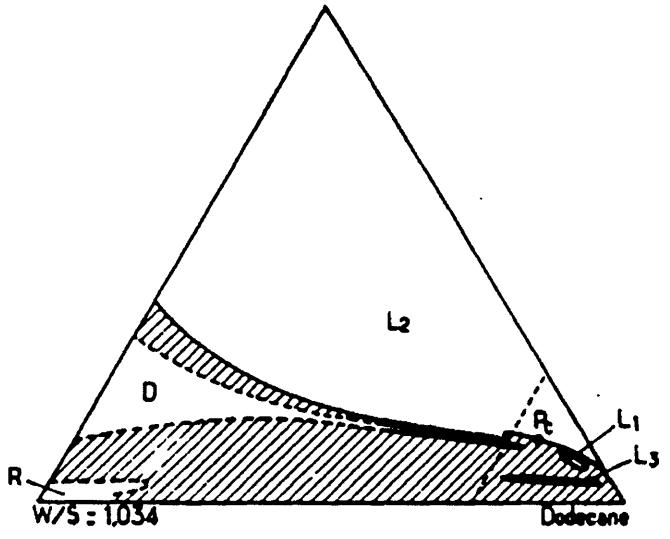

Figure 3-5: Phase triangle (from Bellocq *et al.*[12])

where SDS and dodecane were used instead of OBS and decane (we expect SDS and OBS have similar properties). The D phase is the lamellar phase, the shaded areas are multi-phase regions. Because the lamellar phase occupies only a narrow strip in the phase triangle, especially toward the dodecane corner, the mixture has large chance to enter the multi-phase region (the bottom white phase in our container) to accommodate excessive components unnecessaray for the formation of lamellar phase. These components include certain amount of surfactants in our case, because we found that the upper lamellar phase has a much less surfactant concentration with a layer spacing much larger than that being calculated if we assume a one phase volume swelling. For example, with 24 times dilution (OBS 1.605 wt%, pentanol 9.103 wt%, water 1.738 wt%, decane 87.554 wt%) of the original liquid crystal, the upper lamellar

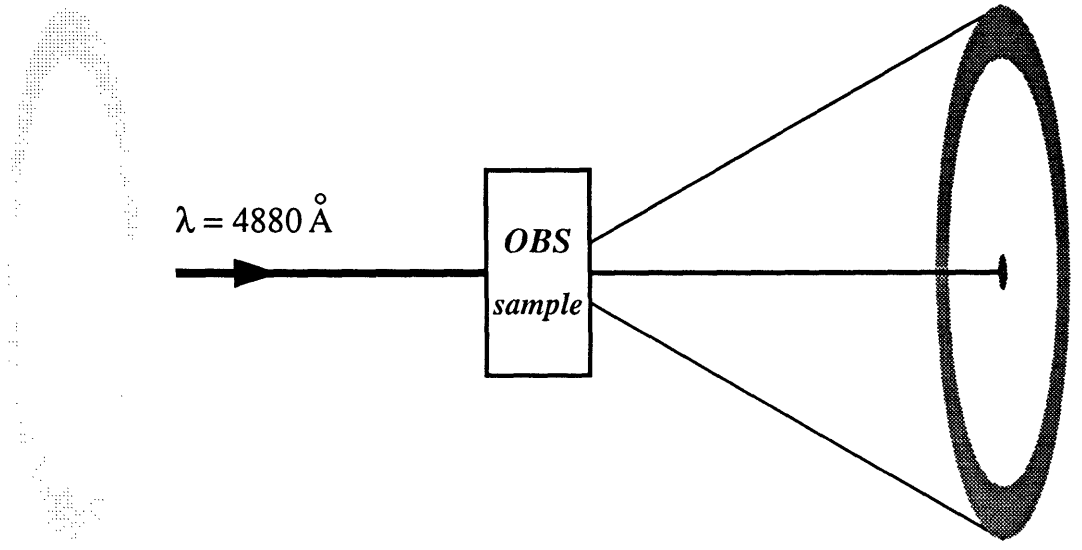

Figure 3-6: A sketch of the Bragg powder light scattering from the OBS sample

phase has a layer spacing $d \sim 3000\mathring{A}$. By changing the amount of water or pentanol slightly near the given phase point, we can change the layer spacing of the upper phase significantly. We are able to get a lamellar phase of $d \sim 1800\mathring{A}$ to $1\mu m$.

This unaligned lamellar phase (analogous to the powder sample of crystal in x-ray scattering) scatters laser light into a distinctive ring shape on a screen. Fig 3-6 schematically shows the experimental setup. The dimmer ring on the left is the Bragg ring from the reflected beam by the glass window. When d is greater than $4000\mathring{A}$, the sample displays a brilliant purple or blue color under white light, especially after being gently shaken(not strips, but colorful cloud). These are the direct evidence of the existence of lamellar order.

According to Ref. [11], their swollen lamellar phase has a strong tendency to align

and can align along the glass wall of a $10mm$ diameter tube, while our lamellar phase of comparable layer spacing stays as powder form even in a rectangular cell of path length of 2 mm.

We suck out a fraction of the upper phase into a tall square light scattering cell. The inside dimension of the cell is: $2mm \times 10mm \times 30mm$. After about 4 weeks, we see a continuous distribution of ring sizes, corresponding to a distribution of inter-layer spacings, as we move laser beam along the vertical direction. We take photographs of the two rings at two different beam height and put them at the end of this chapter. The beam spot is at a higher position in the first picture than that in the second picture. The wave length of light is the same in both pictures, the diferent colors are due to different exposure times in taking the two pictures. The ring size does not change along the horizontal direction. It is worth noting that similar effect has been observed in a crystallized suspensions of polystyrene spheres [13]. We will examine this phenomenon in detail in Chapter 7.

Chapter 4

Theory of Swollen Lamellar Phases

4.1 Helfrich Interaction

As we see in Chapter 3, both ionic and non-ionic lamellar phase can be swollen to several thousands angstroms. In this swollen range, hydration effect vanishes since it is very short ranged. Van der Waals interaction between bilayers is also very small, since it scales as $1/d^4$.

So, for a non-ionic highly swollen lamellar phase such as C12E5/water, what force holds stack of layers together so that they do not collapse into vesicles or other colloidal forms?

For the ionic system of OBS, there was an electrostatic interaction that could be long ranged, but by choosing oil (decane) dilution, this force is very much reduced to insignificance [9, 14]. So, we can ask the same question that is yet to be answered for the non-ionic system.

The answer is that the membranes of these highly swollen lamellar phase are very

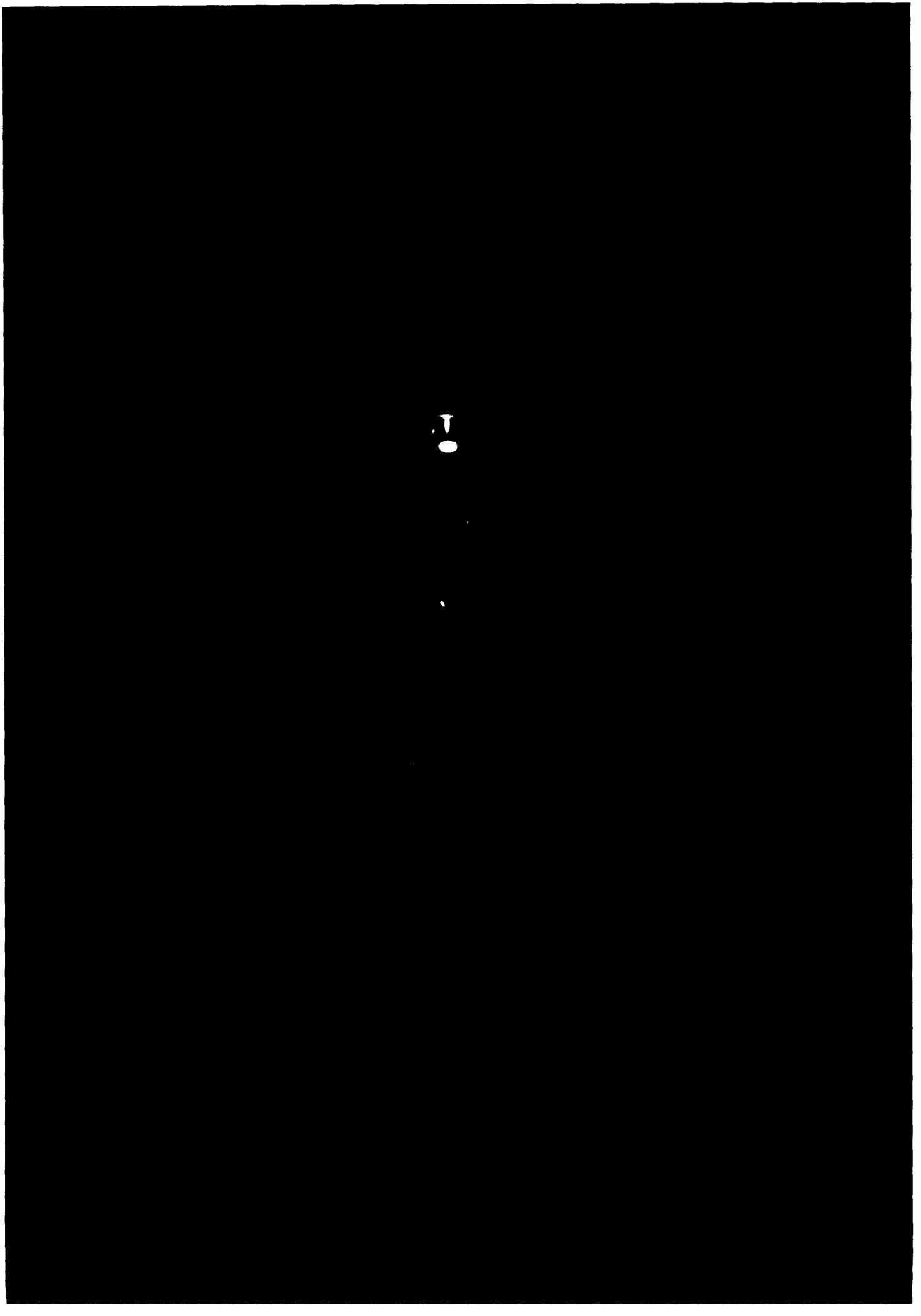

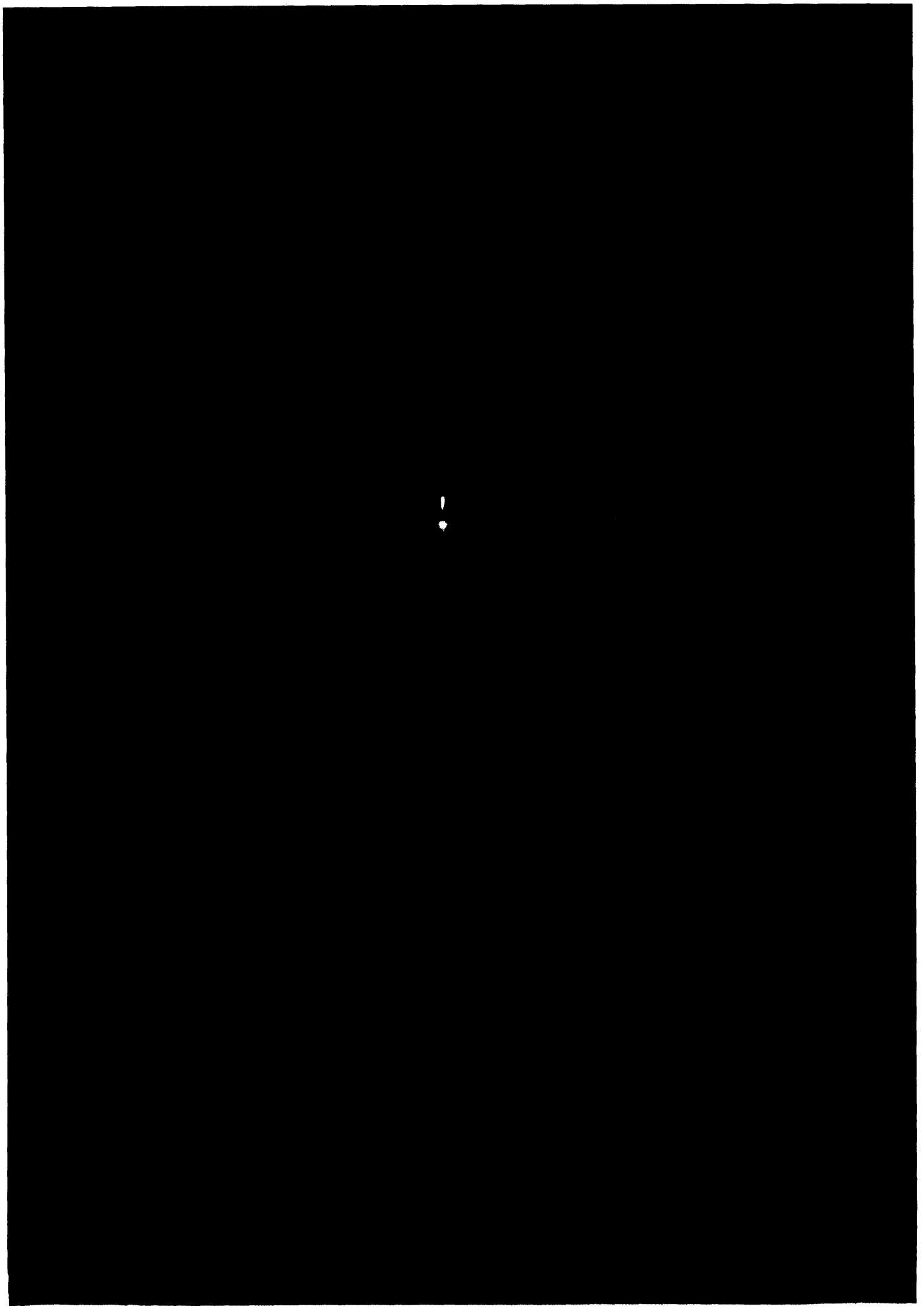

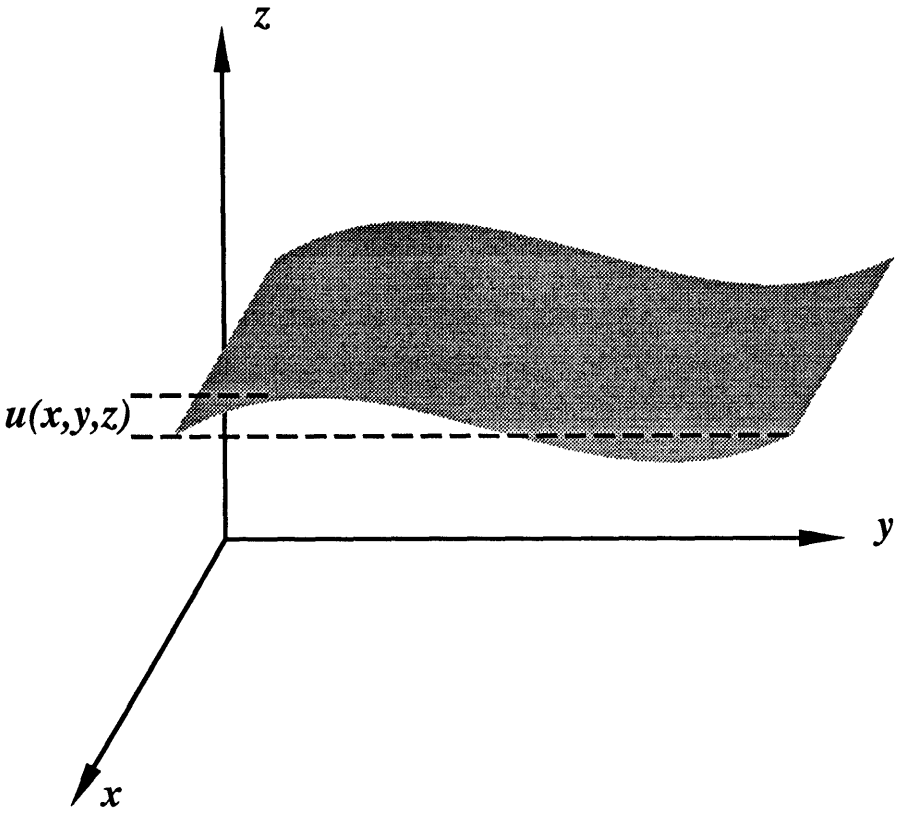

Figure 4-1: Membrane displacement from equilibrium

flexible and thermal fluctuations of membranes cause them to repel each other. It is this repulsion formulized by Helfrich [6] that stabilizes the lamellar order up to very large scale.

We use a slightly different approach from Helfrich's in the formulation of the steric and entropic repulsion. For a stack of lamellar membranes, let $u(x, y, z)$ be the displacement function of each layer in the z direction from its equilibrium (Fig. 4-1). At any instant, the energy E that is related to compression in the z direction as well

as splay in the x, y direction can be written as:

$$E = \int_V \left[\frac{1}{2} B \left(\frac{\partial u}{\partial z} \right)^2 + \frac{1}{2} K \left(\frac{\partial^2 u}{\partial x^2} + \frac{\partial^2 u}{\partial y^2} \right)^2 \right] d^3 \boldsymbol{r} \tag{4.1}$$

where V is the sample volume. B is the compression modulus and $K = k_c/d$, k_c being the curvature elastic constant of a single membrane.

It is easier to describe the system in momentum coordinate $\boldsymbol{q}$ than in spatial coordinate $\boldsymbol{r}$. If sample volume V is large enough, we take the Fourier transformation:

$$u(\boldsymbol{r}) = \int u(\boldsymbol{q}) \, exp(i\boldsymbol{q} \cdot \boldsymbol{r}) \, d^3 \boldsymbol{q} \tag{4.2}$$

Therefore Eq. (4.1) changes to

$$E = \int \left(\frac{1}{2} B q_z^2 + \frac{1}{2} K q_\perp^4 \right) u^*(\boldsymbol{q}) \, u(\boldsymbol{q}) \, d^3 \boldsymbol{q} \tag{4.3}$$

At constant temperature T (in unit $K°$), we treat the whole membrane system as a canonical ensemble. Its statistical state can be described by each element of a functional group $\{ u_j(\boldsymbol{q}) \}$. We have used a discrete function $u_j(\boldsymbol{q})$ instead of a continuous function $u(\boldsymbol{q})$, for the convenience of later derivation.

Similarly, we also change the momentum coordinate into a discrete form $\{ \boldsymbol{q}_i \}$, Eq. (4.3) becomes a summation,

$$E_j = \sum_i \left(\frac{1}{2} B q_{iz}^2 + \frac{1}{2} K q_{i\perp}^4 \right) u_j^*(\boldsymbol{q}_i) \, u_j(\boldsymbol{q}_i) \tag{4.4}$$

The partition function can be written as:

$$\Xi = \sum_j exp(-\beta E_j)$$

$$= \sum_j exp\left[-\beta \sum_i f_j(\boldsymbol{q}_i)\right] \tag{4.5}$$

where $\beta = 1/k_B T$ and

$$f_j(\boldsymbol{q}) = \left(\frac{1}{2}Bq_z^2 + \frac{1}{2}Kq_\perp^4\right) u_j^*(\boldsymbol{q})\, u_j(\boldsymbol{q}) \tag{4.6}$$

Change the exponential in Eq. (4.5) into a product form,

$$\Xi = \sum_j \prod_i exp\left[-\beta f_j(\boldsymbol{q}_i)\right] \tag{4.7}$$

Since u_j can be an arbitrary function, the exchange of the summation sign and the product sign only introduces change of a factor, that is,

$$\Xi \sim \prod_i \sum_j exp\left[-\beta f_j(\boldsymbol{q}_i)\right] \tag{4.8}$$

Now we change the summation in the above equation into a integral over a continuous varible $u(\boldsymbol{q})$, the free energy of the system can be found as:

$$\begin{aligned} F &= -k_B T \ln \Xi \\ &= -k_B T \sum_{\boldsymbol{q}} \ln \int_0^\infty du(\boldsymbol{q})\, exp\left[-\beta\left(\frac{1}{2}Bq_z^2 + \frac{1}{2}Kq_\perp^4\right) \mid u(\boldsymbol{q}) \mid^2\right] + constant \\ &= \frac{1}{2}k_B T \sum_{\boldsymbol{q}} \ln\left(Bq_z^2 + Kq_\perp^4\right) + constant \end{aligned} \tag{4.9}$$

At infinite separation between membranes, the compression modulus B vanishes, so the cost of free energy to bring membranes from infinite separation to a stack of

membranes with separation d is :

$$\Delta F = -\frac{1}{2}k_B T \sum_{\boldsymbol{q}} \ln \frac{K q_\perp^4}{B q_z^2 + K q_\perp^4} \tag{4.10}$$

Eq. (4.10) is exactly the same as the result obtained by Hefrich [6]. For the rest, we follow Helfrich's derivation and get the first order approximation of the free energy potential of steric interaction per unit area of membrane in a multi-layer system in terms of d, k_c and T,

$$\frac{\Delta F}{A} \equiv V_h = \frac{3\pi^2}{128}\frac{(k_B T)^2}{k_c d^2} \tag{4.11}$$

where A is the membrane area of the sample.

Knowing the potential of interaction, we can find the compression modulus B which is also equivalent to the compression coefficient D_{22} in the free energy expansion discussed in the next section,

$$B \equiv D_{22} = \frac{9\pi^2}{64}\frac{(k_B T)^2}{k_c d^3} \tag{4.12}$$

It is worth noting that the Helfrich interaction describes an average entropic effect for large scale structures compared with molecular length scale, its fundamental origin is still the electromagnetic interaction. But this entropic effect exists widely in nature. Two polymer chains repelling each other at finite temperature is an analogy of Helfrich effect in one dimension.

4.2 Hydrodynamics of Highly Swollen Lamellar Phase

A hydrodynamic model of fluid lamellar phase of surfactant/water was first proposed by Brochard and de Gennes [7] for system with $d \sim 200\mathring{A}$. A more explicit study of the hydrodynamic modes by experiments was done by Nallet *et al.*[15] on SDS/pentanol/water/dodecane system with $d \sim 400\mathring{A}$ recently. In treating the energy involved in bilayer deformation, Brochard and de Gennes assumed a stretching in the plane of the layers, producing a change in the area per surfactant molecule. Nallet *et al.* introduced a layer compression which results in a change in bilayer thickness.

We based our choices of variables on the phenomenological approach of Brochard and de Gennes and extend the theory to system with large layer spacing. We view the lyotropic lamellar phase as consisting of two components, membranes and background solution. At constant temperature we need three variables to describe the behavior. These may be the total density dilation Θ, the dilation of the layer spacing $\gamma = (d - d_{eq})/d_{eq} = \partial u/\partial z$ and the dilation of the surfactant concentration (here, surfactants means all the components that make the membranes) $\varepsilon = (c_0 - c)/c_0 = -\delta c/c_0$ where d_{eq} is the layer spacing at equilibrium. Since Θ involves the first sound, which is much faster than the membrane fluctuations we are considering and couples little to them, We may take Θ as zero. That means we assume that the total content of lamellar phase is incompressible. For the third variable, instead of using ε, one may use the relative change of the area per polar head $\delta = (A - A_{eq})/A_{eq}$ where A_{eq} is the area per polar head at equilibrium. We have assumed that concentration variation of surfactants (number of molecules per unit volume) comes from either the compression of inter-membrane distance, or the

stretching of membrane themselves. Therefor it can be readily proved that $\varepsilon = \gamma + \delta$. Using strain of the area of surfactant molecules as one of our variables is similar to a more recent theoretical approach by Lubensky *et al.* [16] where a picture of crumpling membrane is introduced.

Therefore, we only have two independent variables γ and δ to describe the system. For convenience, we will use the specific example of C12E5/water system at $d \sim 2000\mathring{A}$ for our analysis, with the understanding that theory developed here can be applied to other ternary or quarnary lamellar phases in the Hefrich regime with layer spacing on the same order of magnitude.

The free energy density can be expanded as

$$\begin{aligned} f &= \frac{1}{2}D_{22}\gamma^2 + D_{23}\gamma\delta + \frac{1}{2}D_{33}\delta^2 + \frac{1}{2}K\left(\frac{\partial^2 u}{\partial x^2}\right)^2 \\ &\equiv f_1 + \frac{1}{2}K\left(\frac{\partial^2 u}{\partial z^2}\right)^2 \end{aligned} \tag{4.13}$$

where the last term is the membrane curvature elastic energy and $K = k_c/d$. D_{22} should be the constant of inter-membrane compression. As we shall see later, because of the week Hefrich interaction between largely spaced membranes in our system, we expect a smaller value of D_{22} than traditional liquid crystals. In fact, it is so small that we can no longer afford to treat the curvature elastic energy as higher order correction.

Following [7], the equations of motion of the fluid are:

$$\begin{aligned} \rho\frac{\partial v_x}{\partial t} &= -\frac{\partial p}{\partial x} + \frac{\partial}{\partial x}\left(\frac{\partial f_1}{\partial \delta}\right)_\gamma \\ &\quad +\eta\left(2\frac{\partial^2 v_x}{\partial x^2} + \frac{\partial^2 v_x}{\partial z^2} + \frac{\partial^2 v_z}{\partial x \partial z}\right) \\ \rho\frac{\partial v_z}{\partial t} &= -\frac{\partial p}{\partial z} + \frac{\partial}{\partial z}\left(\frac{\partial f_1}{\partial \gamma}\right)_\delta - K\left(\frac{\partial^4 u}{\partial x^4}\right) \end{aligned} \tag{4.14}$$

$$+\eta\left(2\frac{\partial^2 v_z}{\partial z^2}+\frac{\partial^2 v_z}{\partial x^2}+\frac{\partial^2 v_x}{\partial x \partial z}\right) \tag{4.15}$$

where we have included the force due to curvature elasticity, and p and $\boldsymbol{v}$ are the local pressure and velocity of the fluid. Water is assumed not to cross the bilayers, and the surfactant molecules are assumed not to leave them; that is, no permeation occurs. With no permeation $v_z = \partial u/\partial t$, and the x component of the lipid velocity is given by $v_{Lx} = \partial\delta/\partial t$. Under these conditions, and with the material 98% water, it is appropriate to use an isotropic shear viscosity η equal to the viscosity of water in Eqs. (4.14) and (4.15). (Equations including permeation and anisotropic expressions for the shear viscosity can be found in [7] and [15].) Water may, however, flow between the bilayers in the x direction. This is described by the phenomenological equation [7]

$$(v_{Lx} - v_x) = \mu\frac{\partial}{\partial x}\left(\frac{\partial f_1}{\partial \delta}\right)_\gamma \tag{4.16}$$

where v_{Lx} is the x component of lipid velocity. μ is called the slip coefficient[7] and has an expression[15],

$$\mu = \frac{(d-\zeta)^2}{12\eta} \tag{4.17}$$

From the conservation of surfactant molecules, there is,

$$\nabla \cdot \boldsymbol{v}_L = \partial\varepsilon/\partial t \tag{4.18}$$

The incompressibility of the phase means,

$$\nabla \cdot \boldsymbol{v} = 0 \tag{4.19}$$

Combining Eq. (4.18) and Eq. (4.19), we have,

$$\frac{\partial \varepsilon}{\partial t} = \mu \frac{\partial^2}{\partial x^2} \left(\frac{\partial f_1}{\partial \delta} \right)_\gamma \tag{4.20}$$

If we assume the Fourier components of u and ε have the time and space dependence $e^{i\boldsymbol{q}\cdot\boldsymbol{r}-i\omega t}$ we may use Eqs. (4.15) and (4.20), combined with the incompressibility and impermeability conditions to arrive at the characteristic determinant for non-trivial u and ε

$$\begin{vmatrix} \left(\omega^2 - i\omega\eta q^2/\rho - \omega_0^2\right) & (i\omega + \mu q_x^2 D_{33}) \\ & -\omega_1^2 \left(i\omega + \mu q_x^2 D_{23}\right) \end{vmatrix} = 0 \tag{4.21}$$

where

$$\omega_0^2 = \frac{1}{\rho}\left(\frac{q_x q_z}{q}\right)^2 \left(D_{22} - D_{23} + K\frac{q_x^4}{q_z^2}\right) \tag{4.22}$$

$$\omega_1^2 = \frac{1}{\rho}\left(\frac{q_x q_z}{q}\right)^2 (D_{33} - D_{23}) \tag{4.23}$$

Before solving Eq. (4.21), it is useful to estimate the magnitudes of D_{22}, D_{23}, and D_{33}. Physically, f_1 in Eq. (4.13) arises from the effects of the Helfrich repulsion and layer stretching; these may be described by the phenomenological free energy density

$$\mathcal{F} = \frac{V_h(d)}{d_{eq}} + \frac{1}{2}\chi c (A - A_0)^2 \tag{4.24}$$

where χ is a coefficient of layer resistance to stretching [7], and A_0 is the area per polar head in an unstretched bilayer. In order to expand $\mathcal{F}$ in terms of γ and δ, let us imagine a static process(with no long range fluctuations) in which such bilayers are assembled to a lamellar phase of separation d_0. The concentration of surfactant

will be $c_0 = 2/A_0 d_0$ molecules per unit volume. When such lamellar phase relaxes to equilibrium, the repulsion between the layers will cause an increase in layer spacing to $d_{eq} = d_0(1 + \gamma_0)$; we expect $\gamma_0 \ll 1$. Since the surfactant concentration does not change during this process, $A_{eq}\, d_{eq} = A_0\, d_0$ and there will be a corresponding reduction of A to $A_{eq} = A_0/(1 + \gamma_0)$. To find γ_0, we minimize $\mathcal{F}$ while keeping both the surfactant concentration fixed at c_0 and the number of layers fixed. This requires

$$\frac{1}{d_{eq}} \frac{\partial V_h(d)}{\partial d} + \frac{1}{2} \chi c_0\, A_0^2 \frac{\partial}{\partial d} (1 - d_0/d)^2 = 0 \tag{4.25}$$

The solution to Eq. (4.25) gives the value for d_{eq}, from which we may calculate γ_0, A_{eq}, and $\mathcal{F}_{eq}$. The result is $\gamma_0 \simeq V_h/\chi A_{eq}$. With $\gamma + \delta + \gamma\delta = 0$ to maintain constant surfactant concentration, we calculate

$$\begin{aligned} f_1 &= \mathcal{F}(\gamma, \delta) - \mathcal{F}_{eq} \\ &= \frac{9\pi^2}{128} \frac{(k_B T)^2}{k_c d_{eq}^3} \gamma^2 + \chi c_o A_{eq}^2 \gamma_0\, \gamma\delta + \frac{1}{2} \chi c_0 A_{eq}^2\, \delta^2 \end{aligned} \tag{4.26}$$

Thus,

$$D_{22} = \frac{9\pi^2}{64} \frac{(k_B T)^2}{k_c d_{eq}^3} \tag{4.27}$$

$$D_{33} = \chi c_0 A_{eq}^2 = 2\chi A_{eq}/d_{eq} \tag{4.28}$$

and

$$D_{23} = \chi c_0 A_{eq}^2 \gamma_0 = 2\, V_h/d_{eq} = D_{22}/3 \tag{4.29}$$

The cross term D_{23} arises because in equilibrium each bilayer is slightly compressed in order to reduce the repulsion between the layers. For our system with $d_{eq} \simeq 180\,\mathrm{nm}$, and $k_c \sim k_B T = 4.58 \times 10^{-12}\,\mathrm{nJ}$, we estimate $D_{22} \sim 0.8\,\mathrm{Pa}$, or $8\,\mathrm{erg\,cm^{-3}}$. We might naively estimate D_{33} using typical values [2] for $\chi \simeq 2 \times 10^{18}\,\mathrm{Pa\,m^{-1}}$ and $A_{eq} \simeq 0.6\,\mathrm{nm^2}$; for our sample we would obtain $D_{33} \simeq 1.2 \times 10^6$ Pa, or $1.2 \times 10^7\,\mathrm{erg\,cm^{-3}}$.

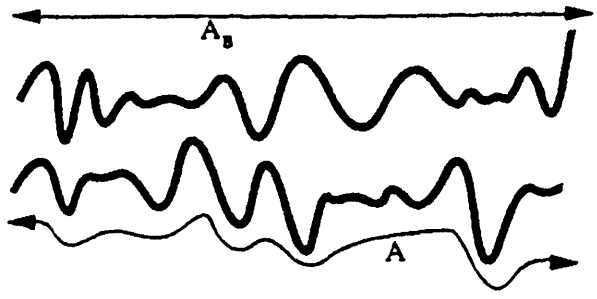

Figure 4-2: Crumpled Membrane

However, the large thermal fluctuations responsible for the Helfrich force mean that the layers are substantially crumpled, although flat on average at long wavelengths. The coefficient D_{33} is therefore greatly reduced, in the same way that crepe paper is much easier to stretch than smooth paper. Fig. 4-2 shematically shows a crumpled membrane. The degree of crumpling can be described by the crumpling ratio which is the ratio of the projected area A_B to its total area A[16]. The magnitude of this effect has been calculated by Lubensky, Prost, and Ramaswamy [16], who estimate $D_{33} \sim 200 - 400\, D_{22}$, that is $D_{33} \simeq 160 - 320\,\mathrm{Pa}$. This leads to $\gamma_0 \simeq 2 \times 10^{-3}$, which is indeed $\ll 1$ as assumed.

We now return to solve Eq. (4.21). There are three roots to the cubic equation and it is not easy to find the analytical solutions to all of them. Our first approach is to find the purely imaginary root which has the lowest frequency, in order to explain the diffusive modes in our experiment. It turns out that when $D_{33} \gg D_{22}$, D_{23} and $\omega \leq 10^3\,\mathrm{sec}^{-1}$, we can drop the terms in Eq. (4.21) which contain ω^2 and ω^3, we

obtain

$$i\omega = \Gamma = \mu \frac{D_{22}q_z^2 + Kq_x^4}{q_z^2 + \mu\eta q^4 + (K/D_{33})q_x^4} q_x^2 \tag{4.30}$$

It is gratifying to see in the following that Eq. (4.30) can be reduced to two simpler dispersion relations that has been predicted both by Brochard*et al.* and Nallet*et al.*

When $q_z \to 0$, Eq. (4.30) becomes,

$$i\omega = \frac{K}{\eta} q_x^2 \tag{4.31}$$

This is the mode of undulation [15] which does not involve concentration variation in the z direction. In Chapter 7, we will see that to observe this mode by light scattering, we have to set the detector out of the scattering plane.

In the other limit, when q_z is not small compared with q_x(called oblique case), if d becomes smaller, the second terms in both the numerator and the denominator become unimportant, since K/D_{22} and μ are both proportional to d^2. We get,

$$i\omega = \mu D_{22} q_x^2 \tag{4.32}$$

Nallet *et al.* call this mode the baroclinic mode. This mode involves strong concentration fluctuation, and is readily observed in light scattering experiment.

In both cases, the third term in the denominator of Eq. (4.30) are small enough to be neglected.

Chapter 5

Dynamic Light Scattering

5.1 Light Scattering Theory

In this section, we begin with the theory of light scattering[17, 18] in an isotropic medium. Light is scattered by changing electric dipoles in matter. The radiation field at point $\boldsymbol{r}$ due to a classical electric dipole $\boldsymbol{p}(t)$ located at the origin is,

$$\boldsymbol{E}(\boldsymbol{r},t) = \frac{1}{c^2 r k^2}\left[\boldsymbol{k}\times\left[\boldsymbol{k}\times\frac{\partial^2\boldsymbol{p}(t')}{\partial t'^2}\right]\right]_{t'=t-r/c} \tag{5.1}$$

where $\boldsymbol{k}$ is the wave vector along the direction of propagation of the radiation. Consider a nonmagnetic, nonconducting, non-absorbing medium shown in Fig. 5-1 with an average dielectric constant ϵ_0 and its local dielectric tensor

$$\tilde{\epsilon} = \epsilon_0\tilde{I} + \delta\tilde{\epsilon}(\boldsymbol{r},t) \tag{5.2}$$

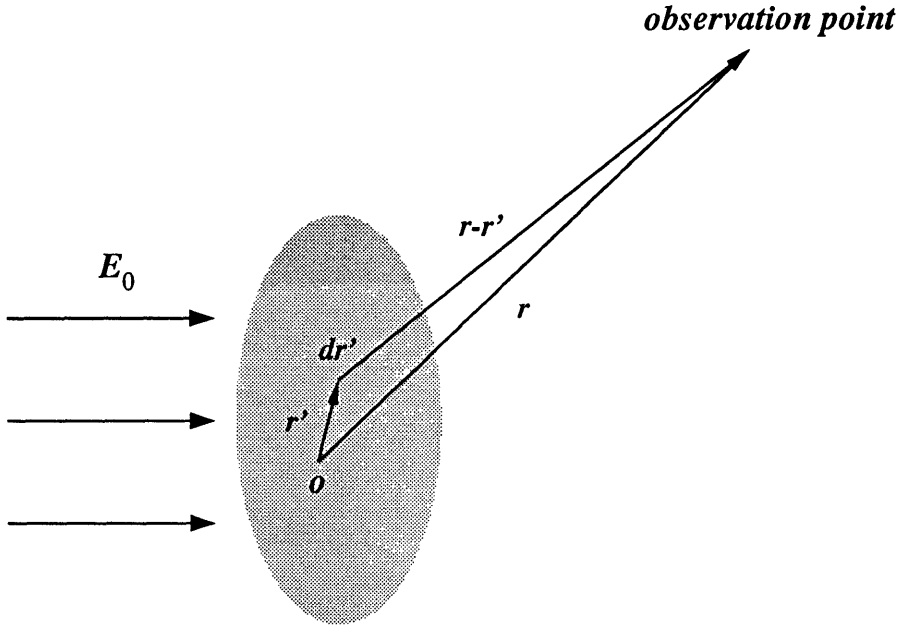

Figure 5-1: Light scattering geometry

where $\delta\tilde{\epsilon}$ is the dielectric constant fluctuation tensor at position $\boldsymbol{r}$ and time t; $\tilde{I}$ is the unit tensor. An incoming light has an electric field

$$\boldsymbol{E}_i = \boldsymbol{E}_0 exp\, i\,(\boldsymbol{k}_i \cdot \boldsymbol{r} - \omega t) \tag{5.3}$$

The electric dipole moment of each differential element is,

$$\begin{aligned} d\boldsymbol{P} &= \frac{1}{4\pi}(\tilde{\epsilon} - 1)\,\boldsymbol{E} d^3\boldsymbol{r} \\ &= \frac{1}{4\pi}(\epsilon_0 - 1)\,\boldsymbol{E} d^3\boldsymbol{r} + \frac{1}{4\pi}\delta\tilde{\epsilon}\boldsymbol{E} d^3\boldsymbol{r} \end{aligned} \tag{5.4}$$

When Eq. (5.4) is plugged into Eq. (5.1) to find the radiation field, the first term of Eq. (5.4) gives the forward plane wave radiation, with a wavelength of $2\pi/\left(\sqrt{\epsilon_0}k\right)$. The second term gives the scattered radiation. Therefore a homogenous, non-fluctuating medium does not scatter light, while density fluctuations of the medium in either space or time scatter light off the forward direction of propagation. The scattered field,

$$\begin{aligned} \boldsymbol{E}_s &= \int_V \frac{-\omega^2}{4\pi c^2 k_s^2 \mid \boldsymbol{r} - \boldsymbol{r}\,' \mid} \\ &\quad [\boldsymbol{k}_s \times [\boldsymbol{k}_s \times \delta\tilde{\epsilon}(\boldsymbol{r}\,', t')\, \boldsymbol{E}_0 exp\; i(\boldsymbol{k}_i \cdot \boldsymbol{r}\,' - \omega t')]]_{t'=t-n\mid \boldsymbol{r}-\boldsymbol{r}\,' \mid /c}\, d^3\boldsymbol{r}\,' \end{aligned} \tag{5.5}$$

where $n = \sqrt{\epsilon_0}$ is the refractive index of the medium. V is the illuminated volume. If we choose the origin of the coordinate system inside the illuminated volume and assume that the dimension of the illuminated volume is small compared to the distance of the field observation point from the origin, $\mid \boldsymbol{r} - \boldsymbol{r}\,' \mid$ in the denominator of Eq. (5.5) becomes $\boldsymbol{r}$. All the light element observed at the observation point have approximately the same wave vector $\boldsymbol{k}_s$. Under these conditions, Eq. (5.5) can be simplified to:

$$\boldsymbol{E}_s = \frac{-E_0\omega^2 sin\Phi}{(4\pi)\, c^2 r} \int_V \delta\epsilon(\boldsymbol{r}\,', t)\, exp(i\boldsymbol{q} \cdot \boldsymbol{r}\,' - i\omega t)\, d^3\boldsymbol{r}\,' \tag{5.6}$$

where $\boldsymbol{q} = \boldsymbol{k}_s - \boldsymbol{k}_i$ is the momentum transfer from the light to the system. Φ is the angle between $\boldsymbol{k}_s$ and $\boldsymbol{E}_0$.

In experiments, we often measure the intensity and the time correlation function of the field at a given $\boldsymbol{q}$, instead of measuring the field directly. The time correlation function of the field is,

$$\langle \boldsymbol{E}_s^*(\boldsymbol{q}, t_1) \cdot \boldsymbol{E}_s(\boldsymbol{q}, t_2) \rangle \tag{5.7}$$

where $\langle\ \rangle$ represents ensemble averaging. It is known that the ensemble averaging of a statistical system at thermal equilibrium can be replaced by time averaging. So in the following text, we will use $\langle\ \rangle$ to represent time averaging. At thermal equilibrium, the process that causes the fluctuations $\delta\epsilon(\boldsymbol{r},t)$ is stationary which means that Eq. (5.7) depends only on the difference $\tau = \mid t_1 - t_2 \mid$. Therefore, we have,

$$\begin{aligned} & \langle \boldsymbol{E}_s^*(\boldsymbol{q},t_1)\cdot\boldsymbol{E}_s(\boldsymbol{q},t_2)\rangle \equiv \langle \boldsymbol{E}_s^*(\boldsymbol{q},0)\cdot\boldsymbol{E}_s(\boldsymbol{q},\tau)\rangle \\ = & \frac{VE_0^2\omega^4 sin^2\Phi}{(4\pi)^2 c^4 r^2}\int_V \langle\delta\epsilon^*(0,0)\,\delta\epsilon(\boldsymbol{r}\,',\tau)\rangle exp(i\boldsymbol{q}\cdot\boldsymbol{r}\,' - i\omega\tau)\,d^3\boldsymbol{r}\,' \end{aligned} \tag{5.8}$$

The intensity of the scattered light may be obtained by setting $\tau = 0$ in Eq. (5.8), and is proportional to the Fourier transform of the equal time correlation function $\langle\delta\epsilon(0)\,\delta\epsilon(\boldsymbol{r})\rangle$.

$$\langle E_s^2\rangle = \frac{VE_0^2\omega^4 sin^2\Phi}{(4\pi)^2 c^4 r^2}\int_V \langle\delta\epsilon^*(0)\,\delta\epsilon(\boldsymbol{r}\,')\rangle exp(i\boldsymbol{q}\cdot\boldsymbol{r}\,')\,d^3\boldsymbol{r}\,' \tag{5.9}$$

5.2 Homodyning vs. Heterodyning

In measuring the time correlation function in a dynamic light scattering experiment, the detector receives light scattered by spatial and time fluctuations of the material that is being investigated. We call this scattered light signal and its field $\boldsymbol{E}_s$. But the detector may also receive lights by other sources, for example, light scattered off the incoming beam by small traces on a not sufficiently clean glass window of the sample cell. We call this kind of light *local oscillator* [19] and call its field and its average intensity $\boldsymbol{E}_l$ and I_l. If the polarization of $\boldsymbol{E}_l$ is in the same direction as $\boldsymbol{E}_s$, so that the two fields can add, the resultant time correlation function will depend on the local oscillator. In most cases, $\boldsymbol{E}_l$ and $\boldsymbol{E}_s$ are statistically independent, and fluctuations of $\boldsymbol{E}_s$ are often negligible. Under these conditions, the time correlation

function of intensity can be reduced to:

$$\begin{aligned} & \langle \mid \boldsymbol{E}_s(0) + \boldsymbol{E}_l(0) \mid^2 \mid \boldsymbol{E}_s(t) + \boldsymbol{E}_l(t) \mid^2 \rangle \\ = \; & I_l^2 + I_s I_l + 2 I_l Re\left(\langle E_s^*(0) E_s(t) \rangle\right) + \langle \mid E_s(0) \mid^2 \mid E_s(t) \mid^2 \rangle \end{aligned} \tag{5.10}$$

In most cases of light scattering experiment, the scattering volume can be divided into many sub-regions that is small compared to the wavelength of light to allow superposition of electric field, but large to permit particle motions in one subregion to be independent of those in another. In this case, it can be proved [19], using central limit theorem, that the last term in Eq. (5.10) can be related to the third term as:

$$\langle \mid E_s(0) \mid^2 \mid E_s(t) \mid^2 \rangle \;=\; I_s^2 + \mid \langle E_s^*(0) E_s(t) \rangle \mid^2 \tag{5.11}$$

The intensity correlation function can be finally written as,

$$\langle i(0) i(t) \rangle = I_s^2 + I_s I_l + I_l^2 + 2 I_l Re\left(\langle E_s^*(0) E_s(t) \rangle\right) + \mid \langle E_s^*(0) E_s(t) \rangle \mid^2 \tag{5.12}$$

There are two limits to the above equation. When the local oscillator is negligible, the auto-correlator lets the signal beat itself, we get the so called *homodyning* time correlation function,

$$\langle i(0) i(t) \rangle \sim 1 + a_1 \mid \langle E_s^*(0) E_s(t) \rangle \mid^2 \tag{5.13}$$

where a_1 is a proportional constant.

In the other limit, when $I_l \gg I_s$, we get the so called *heterodyning* time correlation function.

In many diffusive processes, the field correlation function often takes a form of exponential function as in the case of a dilute suspending particle solution which will

be discussed in the next section , we then have the following forms of decay functions:

$$\langle i(0)\, i(t)\rangle = \begin{cases} B + A\ exp(-2\ t/\tau) & \text{(homodyning)} \\ B + A\ exp(-t/\tau) & \text{(heterodyning)} \\ B + A_1\ exp(-2\ t/\tau) + A_2\ exp(-t/\tau) & \text{(intermediate case)} \end{cases} \tag{5.14}$$

where A, B, A_1 and A_2 are all constants with units of I_s^2, τ is a characteristic time constant related to the decay process.

5.3 Dynamic Light Scattering from a Solution of Polystyrene Latex Spheres

Eq. (5.8) and Eq. (5.9) are general formulas for continues medium, which will be used in Chapter 6 when we discuss light scattering on swollen liquid crystals. As a test and calibration for our light scattering setup, we did dynamic light scattering (DLS) on a very dilute solution of standard polystyrene latex sphere. In this case, Eq. (5.6) should be replaced by a volume integral over each of the particles and a sum over particles,

$$\boldsymbol{E}_s = \frac{-E_0\omega^2 sin\Phi}{4\pi c^2 r} \sum_i f_i(\boldsymbol{q})\, v_i \delta\epsilon_i exp(i\boldsymbol{q}\cdot\boldsymbol{r}_i - i\omega t) \tag{5.15}$$

where

$$f_i(\boldsymbol{q}) = \frac{1}{v_i}\int_i exp(i\boldsymbol{q}\cdot\boldsymbol{r})\, \delta\epsilon(\boldsymbol{r},t)\, d^3\boldsymbol{r} \tag{5.16}$$

is the form factor of particle i whose volume is v_i.

If the particles are all identical, and move independently, Eq. (5.8) can be replaced

by a simple form,

$$\langle \boldsymbol{E}_s^*(\boldsymbol{q},0)\cdot\boldsymbol{E}_s(\boldsymbol{q},\tau)\rangle = \frac{VE_0^2\omega^4 sin^2\Phi}{(4\pi)^2 c^4 r^2} Nv^2\delta\epsilon^2 \mid f(\boldsymbol{q}) \mid^2 exp(i\omega\tau)\langle exp(i\boldsymbol{q}\cdot[\boldsymbol{r}(0)-\boldsymbol{r}(\tau)])\rangle \tag{5.17}$$

where N is the number of particles in the illuminated volume.

$\langle exp(i\boldsymbol{q}\cdot[\boldsymbol{r}(0)-\boldsymbol{r}(\tau)])\rangle$ is called *Van-Hove self space time correlation function*, it can be proved [19] to have the following form,

$$\langle exp(i\boldsymbol{q}\cdot[\boldsymbol{r}(0)-\boldsymbol{r}(\tau)])\rangle = exp\left(-Dq^2t\right) \tag{5.18}$$

where D is the difussion coefficient of the solution. According to the *Stokes-Einstein relation*,

$$D = \frac{k_BT}{6\pi\eta a} \tag{5.19}$$

where η is the viscosity constant of water, a is the radius of the particle.

Therefore, combining Eqs. (5.17)-(5.19) with Eq. (5.13), we get the homodyning time correlation function

$$G(t) \sim 1 + a_2\ exp\left(-2Dq^2t\right) \tag{5.20}$$

where a_2 is another constant depending on the number of *coherent area* [19] the detector covers.

The experimental setup is schematically shown in Fig. 5-2. Light from a Helium-Neon laser is guided by a single mode optical fiber of $100\mu m$ in core diameter to a vertical metal arm. After passing through some optical components, it hits the window of the sample cell at normal incidence. Scattered light were collected between

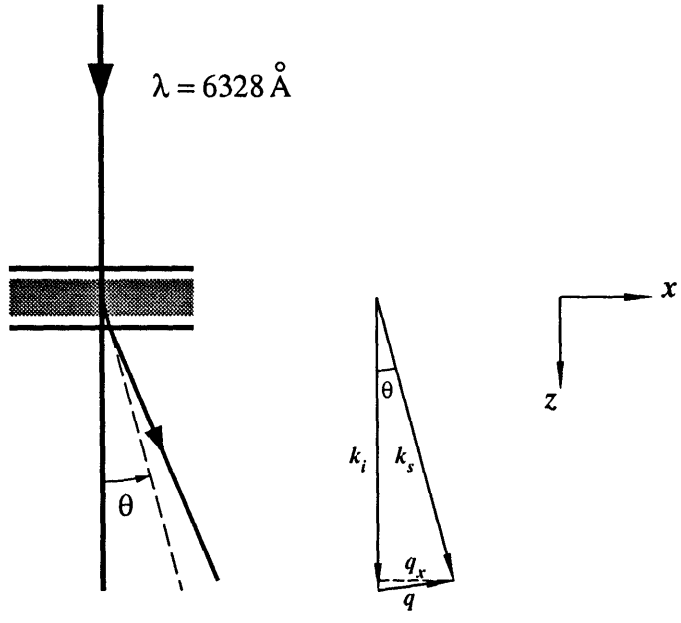

Figure 5-2: Light scattering setup and momentum transfer

$\theta = 3.8°$ and 37° by a multi-mode fiber that transmits the light to a photo multiplier tube (PMT). The magnitude of momentum transfer (see Fig.5-2) is,

$$q = 2nksin\frac{\theta}{2} \tag{5.21}$$

where $k = k_i = k_s$ and n is the index of refraction of the solution. In the case of very dilute polystyrene solution, n takes the value of water.

A auto-correlator is solely responsible for calculating the time correlation function $G(t)$ from digital electronic signals coming from an amplifier and analog-digital converter. The auto-correlator divides the data taking time t (usually 10 to 40 min.) into N small intervals called sample time τ (usually 10 to 10^3 μs) as shown in Fig. 5-3. If the digital counts during interval i is n_i, the correlation of two intervals separated by

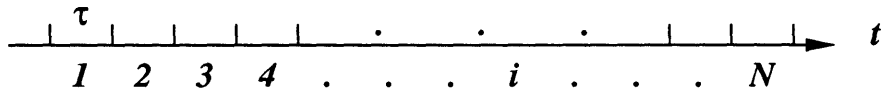

Figure 5-3: Calculating auto-correlation function

l intervals (or l channels) is calculated as:

$$G(l\tau) \sim \sum_{l=0}^{N-1} n_i n_{i+l} \tag{5.22}$$

Since the solution is a isotropic liquid, only the magnitude of the momentum transfer q matters. We measured $G(t)$ at 9 different angles. Fig. 5-4 is one example at $\theta = 37°$. It can be fitted very well, using a single exponential decay function with the background fixed to the measured background which leaves only one free parameter D to vary. Using Eq. (5.19), the radius can be found, $a = 56nm$, while the standard value of the latex sphere in the solution is quoted as $a = 48.0 \pm 2nm$. The discrepancy is small enough to justify the prediction by Eq. (5.20). Actually, in a later experiment, with improved angular calibration we obtained $a = 46nm$. At smaller values of θ, a single exponential function can not provide the best fit, we get good results using double exponential function described in the intermediate case of Eq. (5.14). The slow decay term is a small component. It shows that the detector takes in small

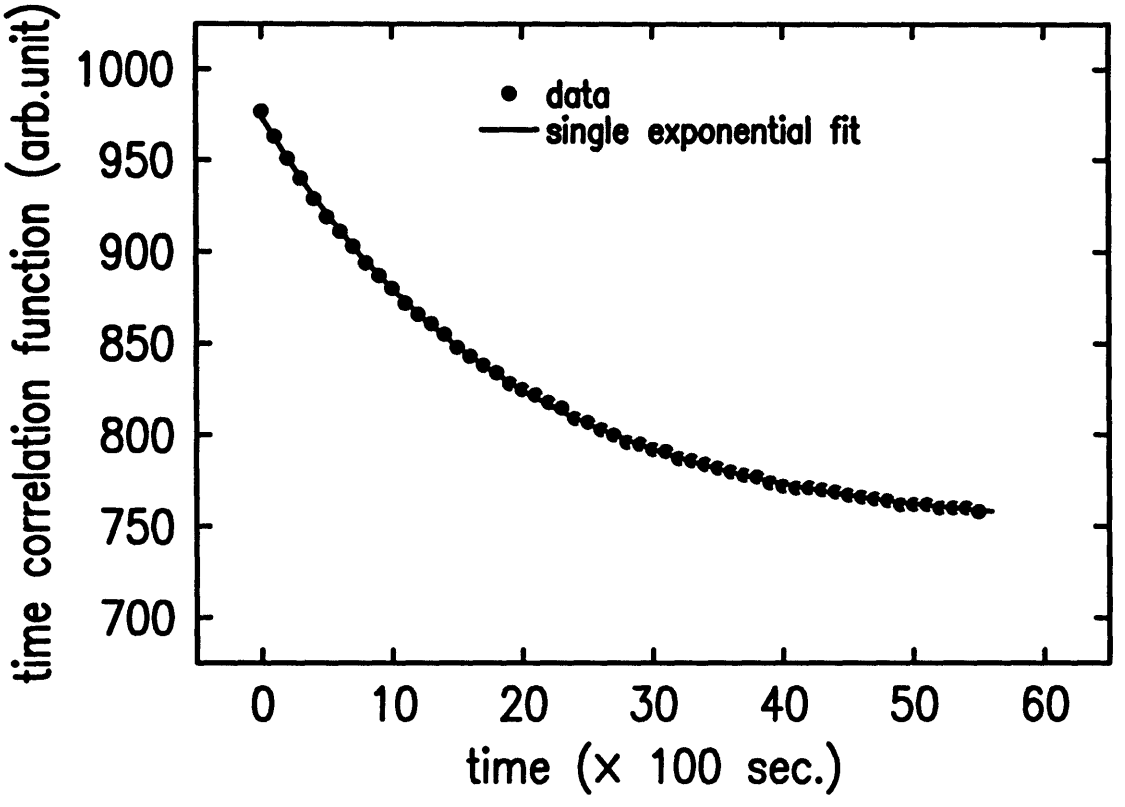

Figure 5-4: Time correlation function from a solution of polystyrene latex spheres

amount of local oscillator light as the angle becomes smaller. Fig. 5-5 shows decay coefficient vs. the momentum transfer obtained from the double exponential fit. It shows a linear dependence on q^2 that goes through the origin, as predicted by theory. Fig. 5-6a shows the radius dependence on angle. We can see that radiusies calculated from a single exponential fit are close to the standard value when θ is above 15°, but departs from the standard value below that angle. The double exponential fits correct the discrepancy when angle becomes smaller. So, we can say that when $\theta > 15°$, the conditions of the setup allows a homodyning case. Fig. 5-6b plot the background to signal ratio, which is the B/A in Eq. (5.14), at different angles. Because the solid angle spanned by the illuminated volume does not change very much as we change the

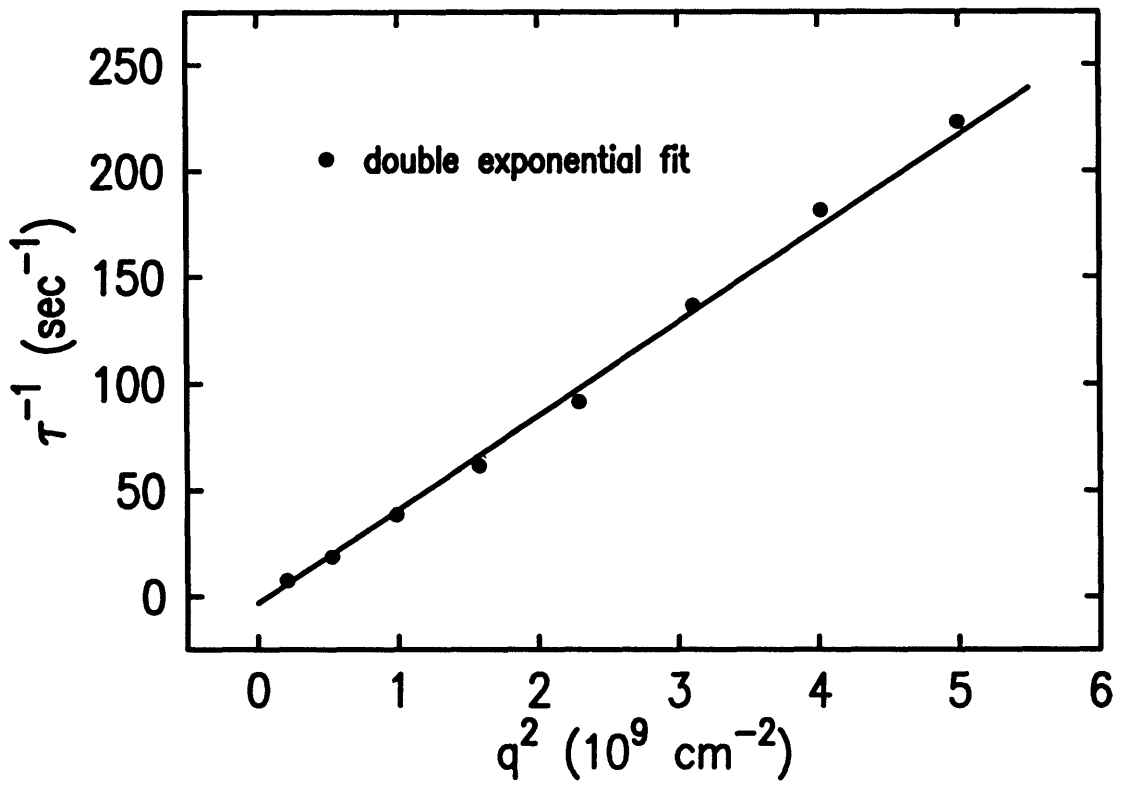

Figure 5-5: Decay rate vs. q for a solution of polystyrene latex sphere

angle, so does the coherence area. So the value of a_2 in Eq. (5.20) varies very slowly. The increase of B/A when θ decrease is caused by other source of light including the local oscillator. By comparing Fig. 5-6b with Fig. 5-6a, we get the following criteria for homodyning; that is, under the current geometry (detector distance, area of exposure, illuminated volume and range of observing angle etc.), if $B/A < 5$, homodyning fitting is valid; if $B/A > 5$, heterodyning component need to be introduced. We will apply this criteria to the dynamic light scattering of lamellar phase as discussed in the next chapter.

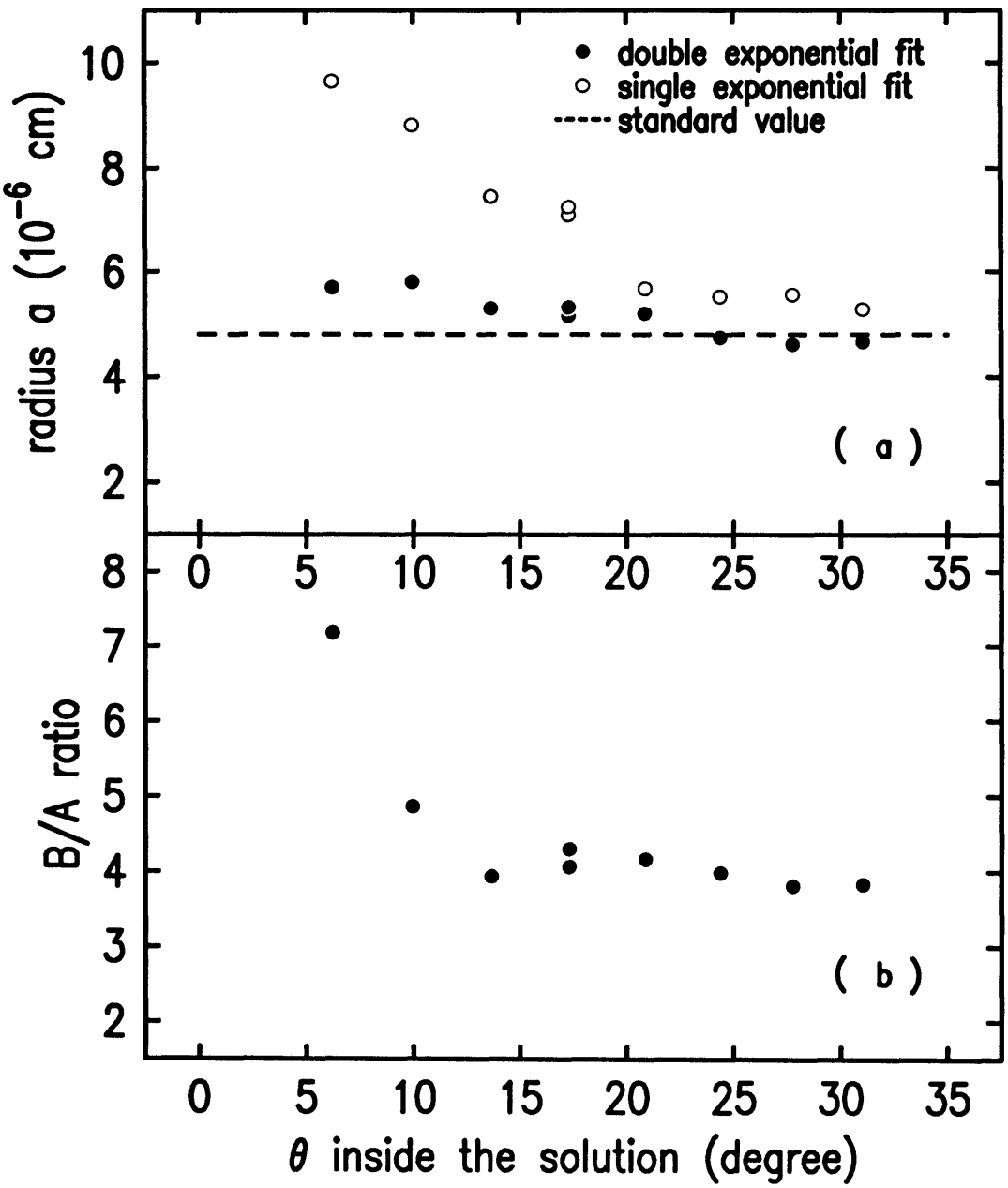

Figure 5-6: (a). Radius vs. angle. (b). B/A ratio vs. angle.

5.4 Polydispersity, Dynamic Light Scattering from Vesicles

In this section, we first develop a fitting function for polydisperse particle solution. Then, we combine this function with the result of time correlation function in the last section and apply them to the data analysis of DLS on vesicle solutions.

For a solution with polydisperse particles, let the particle size distribution be $P(\Gamma)$, where Γ is the diffusion coefficient variable. According to Eq. (5.18),

$$\Gamma = D\,q^2 \tag{5.23}$$

The time correlation function of the electric field scattered by particles having diffusion coefficient in the range of Γ to $\Gamma + d\Gamma$ will be proportional to $exp(-\Gamma\tau)\,d\Gamma$, thus the total normalized correlation function will be,

$$g(\tau) = \int_0^\infty P(\Gamma)\,exp(-\Gamma\tau)\,d\Gamma \equiv \langle exp(-\Gamma\tau)\rangle_{Ave} \tag{5.24}$$

with

$$\int_0^\infty P(\Gamma)\,d\Gamma = 1 \tag{5.25}$$

It is not hard to prove that $g(\tau)$ is the generating function of the moments of the distribution function $P(\Gamma)$. It is also fairly easy to prove that $\log g(\tau)$ is the generating function of the cumulants of $P(\Gamma)$, that is,

$$\begin{aligned} \frac{\partial \log g(\tau)}{\partial \tau}_{|_{\tau=0}} &= \langle\Gamma\rangle_{Ave} \equiv K_1 \\ \frac{\partial^2 \log g(\tau)}{\partial \tau^2}_{|_{\tau=0}} &= \langle(\Gamma - \langle\Gamma\rangle_{Ave})^2\rangle_{Ave} \equiv K_2 \end{aligned} \tag{5.26}$$

$$\frac{\partial^3 \log g(\tau)}{\partial \tau^3}_{|\tau=0} = \langle (\Gamma - \langle \Gamma \rangle_{Ave})^3 \rangle_{Ave} \equiv K_3$$

..... etc.

Therefore, we can expand $\log g(\tau)$ around $\tau = 0$ in terms of the cumulants of $P(\Gamma)$,

$$\log g(\tau) = \sum_{m=0}^{\infty} \frac{K_m}{m!} (-\tau)^m \tag{5.27}$$

That is,

$$g(\tau) = exp\left(-K_1\tau + \frac{1}{2}K_2\tau^2 - \frac{1}{3!}K_3\tau^3 + ...\right) \tag{5.28}$$

So the homodyning time correlation fitting function for polydisperse particle solution can be written as,

$$\langle i(0)\, i(t) \rangle = B + A\left[exp\left(-K_1 t + \frac{1}{2}K_2 t^2 - \frac{1}{3!}K_3 t^3 + ...\right)\right]^2 \tag{5.29}$$

where K_1 is the average diffusion coefficient of the particles, K_2 gives the square of the width of the distribution function $P(\Gamma)$ while K_3 reflects the asymmetry of the distribution function [20]. A function that takes into account both polydispersity and heterodyning component can be written as,

$$\langle i(0)\, i(t) \rangle = B + A_1 [g(t)]^2 + A_2 g(t) \tag{5.30}$$

Vesicles are egg shape particles with lipid bilayer as its outer shell, as shown in Fig. 2-5 in Chapter 3. Its dimension can be from a few hundred to a few thousand angstroms. We use 0.3% SDBS, 0.7% CTAT and 99.% water [5], all by weight to make the vesicle at temperature $T = 19.0°$. Fig. 5-7 shows the phase triangle of the

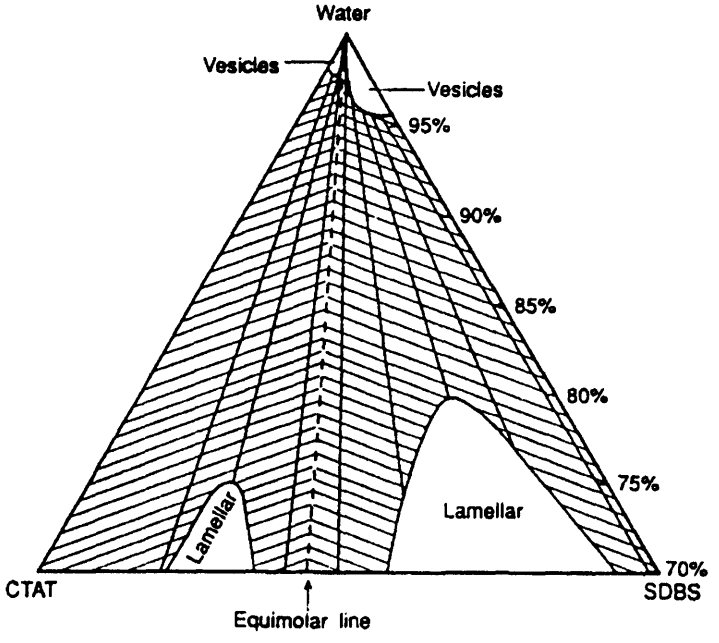

Figure 5-7: Phase triangle of SDBS/CTAT vesicle (from Murthy[5])

three component system and the region of vesicle formation. Fig. 5-8 show one of the auto-correlation functions of intensity scattered by the above vesicle at 12 different angles from $\theta = 32.1°$ to $\theta = 6.8°$. It is fitted with Eq.(5.30) with 4 cumulents. Fig. 5-9 shows one of the similar functions at 9 different angles from $\theta = 8.7°$ to $\theta = 4.4°$ measured a few days later. It is fitted with Eq.(5.30) with 6 cumulants. In both cases, the baseline is fixed as the measured background. Fig. 5-10 show the hydrodynamic effective radius of vesicles a calculated from Eq (5.19) using the fitting results of K_1 for both groups of data. The smooth connection of radius dependence on q shows that the vesicle size does not change over time. The fitting parameters shows a smooth decrease of A_1 and increase of A_2 as θ becomes smaller.

The data around $\theta = 32.1°$ give radius $a = 1015\mathring{A}$. This is about 2 times as large

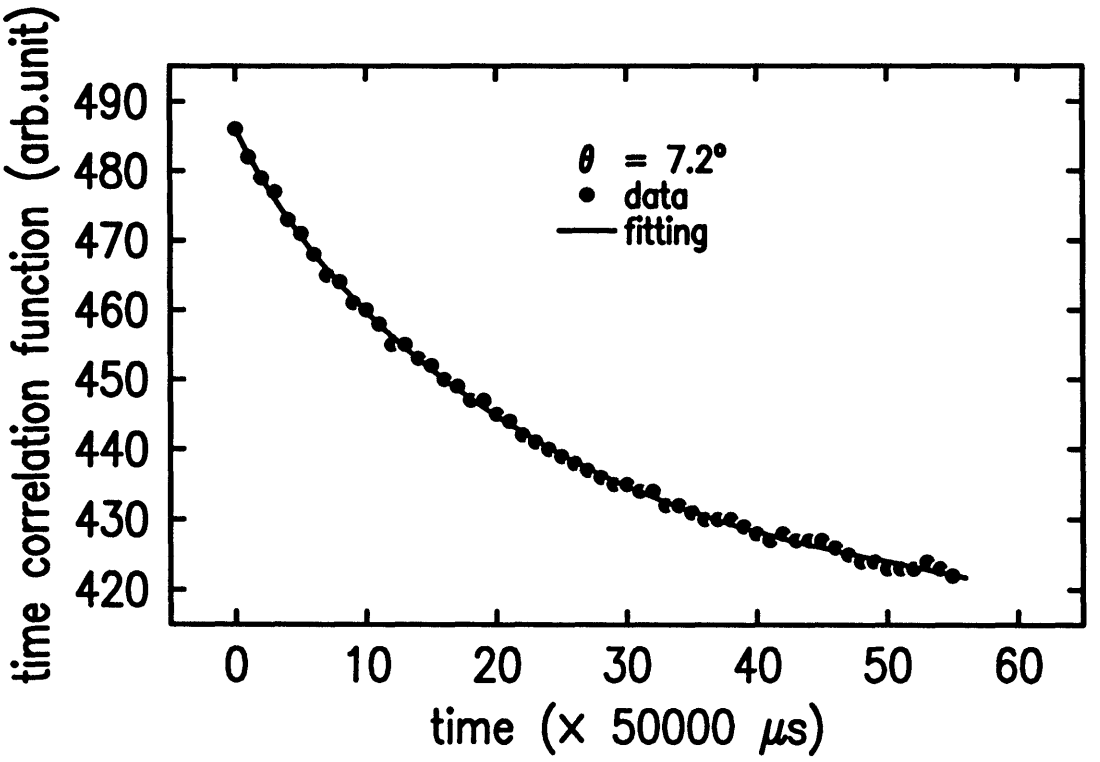

Figure 5-9: Time correlation function of a
solution of SDBS/CTAT vesicles at another angle

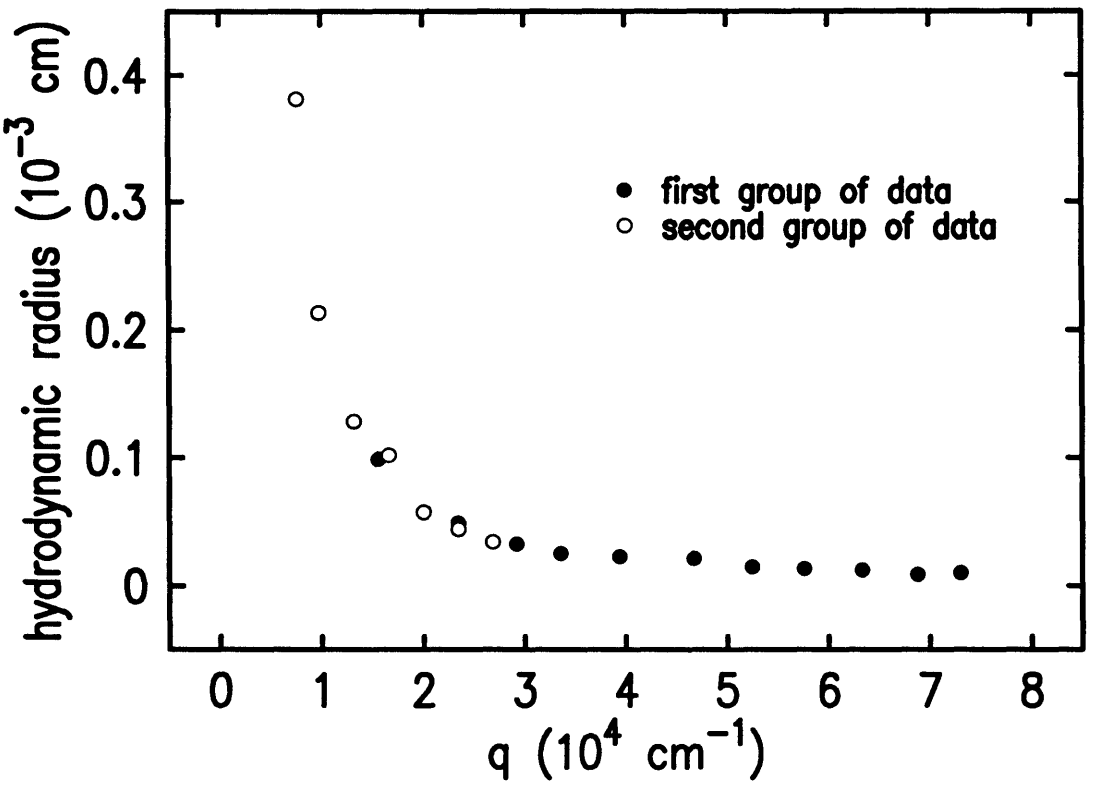

Figure 5-10: Hydrodynamic radius of SDBS/CTAT vesicles vs. q

Chapter 6

Dynamic Light Scattering from the C12E5 System

6.1 Introduction

In Chapter 4, we have studied hydrodynamic modes of thermal fluctuations in swollen lamellar phase with Helfrich inter-membrane interaction. In this chapter, we will discuss our light scattering result from the C12E5/Water system in observing some of the modes. The work has been published in Ref. [22].

6.2 Intensity of Light Scattered from Lamellar Liquid Crystal

Light are scattered by thermal fluctuations of liquid crystals. In this section, we will work out a quantitative expression for the intensity of scattered light.

For the lamellar liquid crystals described in Chapter 3 and Chapter 4, let u be the bilayer displacement. Let $\boldsymbol{i}$ and $\boldsymbol{f}$ be the polarizations of the incident and scattered

light. Also let $\boldsymbol{n}$ be the director (optical axis) and c be the concentration(number of molecules per unit volume) of surfactant molecules that form membranes; in terms of their fluctuating components, these may be written, $\boldsymbol{n} = \boldsymbol{n}_0 + \delta\boldsymbol{n}$, and $c = c_0 + \delta c$, where $\boldsymbol{n}_0$ and c_0 are equilibrium values. Let the molecular dielectric tensor to be,

$$\tilde{\epsilon} = \begin{pmatrix} \epsilon_\perp & 0 & 0 \\ 0 & \epsilon_\perp & 0 \\ 0 & 0 & \epsilon_\parallel \end{pmatrix} \tag{6.1}$$

where the z axis of the matrix representation is along the molecular optical axis. The vector $\boldsymbol{E}_0$ that appears in Eq. (5.3) can be written in terms of $\boldsymbol{i}$ and $\boldsymbol{f}$ as,

$$\boldsymbol{E}_0 = E_0 \left[(\boldsymbol{i} \cdot \boldsymbol{n})\, \boldsymbol{n} + [\boldsymbol{i} - (\boldsymbol{i} \cdot \boldsymbol{n})\, \boldsymbol{n}] \right] \tag{6.2}$$

The vector of the field at the observation point by a differential element should be, according to Eq. (5.5),

$$\begin{aligned} \boldsymbol{E}_r &\sim \boldsymbol{k}_s \times (\boldsymbol{k}_s \times c\tilde{\epsilon} \cdot \boldsymbol{E}_0) \\ &\sim \boldsymbol{k}_s \times \boldsymbol{k}_s \times c \left[\epsilon_\parallel (\boldsymbol{i} \cdot \boldsymbol{n})\, \boldsymbol{n} + \epsilon_\perp [\boldsymbol{i} - (\boldsymbol{i} \cdot \boldsymbol{n})\, \boldsymbol{n}] \right] E_0 \end{aligned} \tag{6.3}$$

Eq. (6.3) has two terms after being expanded, one of them is in the direction of $\boldsymbol{k}_s$ which will be canceled after integration, since electromagnetic wave is a transverse wave. The other term has a component in the $\boldsymbol{f}$ direction with magnitude

$$E_f \sim k_s^2 \left[\epsilon_\perp (\boldsymbol{i} \cdot \boldsymbol{f}) + \Delta\epsilon\, (\boldsymbol{i} \cdot \boldsymbol{n})\, (\boldsymbol{n} \cdot \boldsymbol{f}) \right] c E_0 \tag{6.4}$$

where $\Delta\epsilon = \epsilon_\parallel - \epsilon_\perp$. From Section 5.1, we know that only the terms that contain spatial and time variations in the scattering medium contribute to the scattered field,

these variations in Eq. (6.4) are caused by fluctuations of the molecular director $\boldsymbol{n}$ and the concentration c, therefore,

$$\begin{aligned} \delta E_f \;\sim\; & \epsilon_\perp (\boldsymbol{i}\cdot\boldsymbol{f})\,\delta c + \Delta\epsilon (\boldsymbol{n}\cdot\boldsymbol{i})(\boldsymbol{n}\cdot\boldsymbol{f})\,\delta c \\ & + \Delta\epsilon c\left[(\delta\boldsymbol{n}\cdot\boldsymbol{i})(\boldsymbol{n}_0\cdot\boldsymbol{f}) + (\delta\boldsymbol{n}\cdot\boldsymbol{f})(\boldsymbol{n}_0\cdot\boldsymbol{i})\right] \end{aligned} \tag{6.5}$$

Similar to the procedure in Section 5.1, the scattered intensity at the observation point with polarization in the $\boldsymbol{f}$ direction is,

$$\begin{aligned} I(\boldsymbol{q}) \;\sim\; & \int exp(i\boldsymbol{q}\cdot\boldsymbol{r})\,\langle \delta E_f^* \delta E_f\rangle\, d^3\boldsymbol{r} \\ = \; & \epsilon_\perp^2 (\boldsymbol{i}\cdot\boldsymbol{f})^2 S_{cc}(\boldsymbol{q}) + \Delta\epsilon^2\left[(\boldsymbol{n}_0\cdot\boldsymbol{i})(\boldsymbol{q}_\perp\cdot\boldsymbol{f}) + (\boldsymbol{n}_0\cdot\boldsymbol{f})(\boldsymbol{q}_\perp\cdot\boldsymbol{i})\right]^2 S_{uu}(\boldsymbol{q}) \\ & + 2\Delta\epsilon c(\boldsymbol{i}\cdot\boldsymbol{f})\left[(\boldsymbol{n}_0\cdot\boldsymbol{i})(\boldsymbol{q}_\perp\cdot\boldsymbol{f}) + (\boldsymbol{n}_0\cdot\boldsymbol{f})(\boldsymbol{q}_\perp\cdot\boldsymbol{i})\right] I_m\left[S_{cu}(\boldsymbol{q})\right] \end{aligned} \tag{6.6}$$

We have neglected higher order terms containing $\delta c\Delta\epsilon$.

$$\begin{aligned} S_{cc}(\boldsymbol{q}) &= \int exp(i\boldsymbol{q}\cdot\boldsymbol{r})\,\langle \delta c^*(0)\,\delta c(\boldsymbol{r})\rangle d^3\boldsymbol{r} \\ S_{uu}(\boldsymbol{q}) &= \int exp(i\boldsymbol{q}\cdot\boldsymbol{r})\,\langle \delta u^*(0)\,\delta u(\boldsymbol{r})\rangle d^3\boldsymbol{r} \\ S_{cu}(\boldsymbol{q}) &= \int exp(i\boldsymbol{q}\cdot\boldsymbol{r})\,\langle \delta c^*(0)\,\delta u(\boldsymbol{r})\rangle d^3\boldsymbol{r} \end{aligned} \tag{6.7}$$

Eqs. (6.6)-(6.8) express scattered intensity in terms of the Fourier transforms of the spatial correlation functions of the fluctuating variables u and c. The latter are directly related to the hydrodynamic modes of the system. In fact, viewing the system in terms of hydrodynamic modes is just a way of analyzing the thermal fluctuations.

In particular, undulation mode, expressed by Eq. (4.31) corresponds to $q_z = 0$, thus does not involves concentration fluctuation. That means undulation mode does not contribute to either S_{cc} or S_{uc}. It only contributes to the intensity through the term containing S_{uu} in Eq. (6.6).

On the other hand, the baroclinic mode in the oblique limit expressed by Eq. (4.32), which involves layer displacement fluctuations as well as concentration fluctuations contributes to both S_{cc}, S_{uc} and S_{uu}.

There are other hydrodynamic modes. But they are either too fast, or having a too small amplitude, to have significant contributions to light scattering within the time scale of our experiment.

To measure the effect of pure undulation mode, the first thing we need to do is to isolate the second term in Eq. (6.6). This can be done by setting $\boldsymbol{i} \perp \boldsymbol{f}$. But in this case, the geometric factor in the second term will vanish if $\boldsymbol{q}$ is in the scattering plane defined by the incoming wave vector $\boldsymbol{k}_i$ and the normal of the membrane $\boldsymbol{n}$. So we need to measure off-plane scattering. Secondly, even at $q_z = 0$, S_{uu} may include small amount of contributions from the baroclinic mode. The undulation mode can be separated from the baroclinic contribution by the auto-correlator because the former is much faster at near $q_z = 0$ (see [15]).

So it is clear that only choosing the right $\boldsymbol{q}$ is not enough to isolate a single hydrodynamic mode. Scattering geometry and polarizations of incoming and outgoing light are necessary conditions to be set to isolate certain mode.

If we successfully isolate a mode with a dispersion $\omega(\boldsymbol{q})$, what should the correlation function look like? It can be proved ([21]) that the correlation function of the scattered field,

$$\langle E_s^*(\boldsymbol{q}, 0)\, E_s(\boldsymbol{q}, t)\rangle \;\sim\; exp[i\,\omega(\boldsymbol{q})] \tag{6.8}$$

6.3 Experiment

We focus on measuring the baroclinic mode in the intermediate momentum transfer range. We set $\boldsymbol{k}_s$ in the scattering plane, and keep $\boldsymbol{i}$ and $\boldsymbol{f}$ both perpendicular to the

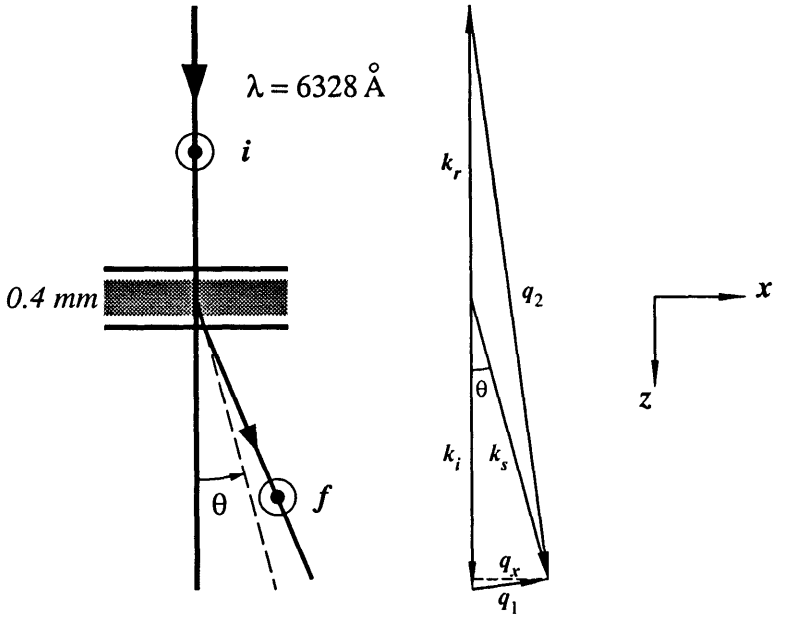

Figure 6-1: Setup

scattering plane. In this case, only the first term in Eq. (6.6) remains, We are only receiving light scattered from the baroclinic mode.

The setup used in the dynamic light scattering on C12E5/Water system is schematically shown in Fig. 6-1. It has been calibrated by experiments on standard polystyrene solutions. Laser beam of $\lambda = 6832\mathring{A}$ is led vertically downward by an optical fiber, so that, at normal incidence, the thin layer of sample in between two quarts glass plates can lie horizontally to avoid phase separation. It is also designed that a microscope can be applied to look at the sample. During the whole process of making sample and taking light scattering data, sample stayed unremoved, so that minimum spatial and temperature disturbance is maintained.

Sample of 2.0 wt.% C12E5 were made as described in Chapter 3 and kept at

$T = 59°$. Scattered light was collected at 13 angles ranging from $\theta = 9°$ to $\theta = 43°$ inside the sample. Strong signals were obtained with a background to signal ratio of at most 5. By comparing the B/A ratio of the autocorrelation function to that polystyrene latex spheres in the same scattering geometry (Fig. 5-6), we determined the scattering to be homodyning. Typical correlation functions are plotted in Fig. 6-2. All of the correlation functions can be fitted very well with two decay times, a larger amplitude slow mode and a smaller amplitude fast mode. The fitting function was

$$y = B + [A_1 exp(-\Gamma_1 t) + A_2 exp(-\Gamma_2 t)]^2 \tag{6.9}$$

with B fixed at the measured background. The values for Γ_1 and Γ_2 are plotted vs. q_x in Fig. 6-3; both modes appeared to depend linearly on q_x^2. One temptation is to associate the large amplitude slow mode (Γ_1) with the baroclinic mode in the oblique limit described by Eqs. (4.32) and (4.27). We obtain $D_{22} = 0.36\,\mathrm{Pa}$ from the slope of the fit to q_x^2, and find $k_c = 2.8 k_B T$ from Eq. (4.27). While these values compare well with those obtained by Nallet *et al.* [15] from studying the baroclinic mode of the SDS system, where the range of swelling was from 4 nm to 35 nm, k_c is two to three times the value obtained for a similar C12E5 system by Strey *et al.* [1] by studying thermally induced deviations from linear swelling with $d = \zeta/\phi$. It is also about three times the value obtained by Nallet *et al.* from their study of the undulation mode. In addition, we also need to explain where the fast mode comes from.

Instead, we applied the more explicit formulation of Eq. (4.21) and one of its approximate solution Eq. (4.30) for system with large layer spacing.

We also did numerical calculations to all the roots of Eq. (4.21), and find, as we shall explain later in this chapter, that the other two roots describe modes which decay too rapidly to see with our autocorrelator.

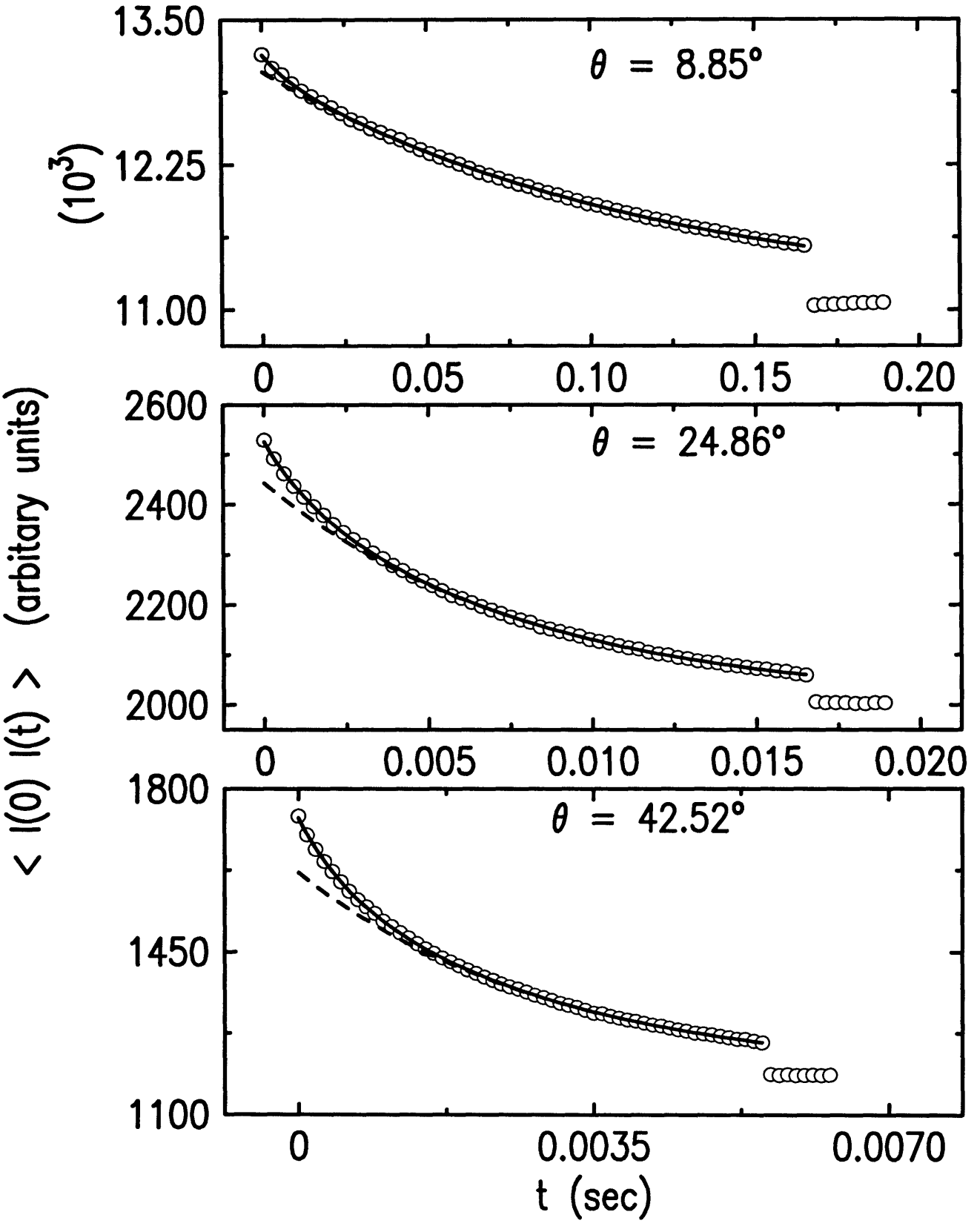

Figure 6-2: Time correlation functions

If Eq. (4.30) describes the only mode we can detect with our correlator, why did we see two decay times in the scattering? The reason is that when light passes through the sample at normal incidence, about 4.5% is reflected back into the sample by the second silica window, and we see scattering at both the angle θ and its complement, as illustrated in Fig. 6-1. The two components have the same q_x value, but the forward scattering has a much smaller q_z than does the backward scattering. Using Eq. (4.30), we can associate the slow and fast decays with backward and forward scattering geometries, respectively.

The scattered intensity for this mode should be inversely proportional to the decay rate Γ, which will tend to make up the weaker incident beam for the backward scattered light. Another factor that make the backward scattered signal relatively stronger is that we set the time scale of the auto-correlator to the slow mode, which tends to discount the forward scattering light. However, that is not enough to explain the observed intensity ratio. One possibility is that since the wave vector for the backward scattering is about 85% of $2\pi/d_{eq}$, the broadening of the Bragg peak may increase the scattering. Since we focused on the dynamic measurement rather than the static measurement, We can only make some qualitative argument about the intensity.

With the two geometries in mind, we first analyzed our data using a numerical solution to Eq. (4.21), choosing the low frequency mode, although when $D_{33} \geq 50\, D_{22}$, the numerical solution is indistinguishable from Eq. (4.30). We chose $K = k_c/d$, D_{22} given by Eq. (4.27), and μ is given by Eq. (4.17) where we neglect the bilayer thickness ζ. When these substitutions are made, the decay time for our concentration fluctuations depends strongly on only two parameters: k_c, and d_{eq}, with a weak dependence on D_{33}. The other quantities are all known by other means. The results of fitting the forward and backward scattering data simultaneously, with $\eta = 0.005$ poise, are shown in Fig. 6-3. When d, D_{33}, and k_c were all allowed to vary we

obtained $k_c = (7.0 \pm 5.0) \times 10^{-12}$ nJ or $(1.5 \pm 1)\, k_B T$, $d_{eq} = (170 \pm 40)$ nm, and $D_{33} = (5.6 \pm 1.4)$ Pa. The large uncertainties arise because the parameters are correlated in the fit. When we restrict d to the 180 nm obtained by Strey *et al.* [1], we find $k_c = (1.35 \pm 0.35)\, k_B T$, and $D_{33} = (5.3 \pm 0.8)$ Pa. It is not obvious that the expression $\mu = {d_{eq}}^2/(12\eta)$ should hold for crumpled bilayers; one might expect the crumpling would result in $\mu = {d_{eff}}^2/(12\eta)$, with $d_{eff} \leq d_{eq}$. As our data could be quantitatively represented by the simpler expression with reasonable values of the parameters, we did not introduce this extra complication.

We now come back to Eq. (4.30). When D_{33} is large, our fit of Eq. (4.30) to the data in Fig. (6-3) is as good as the numerical solution. It is rather insensitive to D_{33}. If we take any value of D_{33} greater than 50 Pa and allow d and k_c to vary, we obtain $d_{eq} = (210 \pm 15)$ nm, and $k_c = (0.75 \pm 0.1)\, k_B T$ with a χ^2 only 20% larger than the best fit for all three parameters. For the parameters we found, the penetration depth $\lambda = (K/D_{22})^{1/2}$ is 210 nm, and D_{22} is 0.8 Pa.

Eq. (4.30) can give a clearer physical picture to the modes. For backward scattering, when q_z is large, the layer compression term dominates in the numerator of Eq. (4.30) while the bending energy of the membrane (or curvature elastic energy) is less important. Because q_z is large, large concentration fluctuations are involved, which scatter the backward beam strongly. This mode is the extension of the oblique baroclinic mode expressed by Eq. (4.32) to a system with large layer spacing. In our case, the curvature energy is small, but not small enough to be neglected when compared with the energy of compression.

For forward scattering, the curvature term dominates and the mode has become mostly one of layer undulation; We are now in a crossover region between the oblique baroclinic mode and pure undulation mode. it can still be detected in our polarization setting ($\boldsymbol{i} \parallel \boldsymbol{f}$) because small concentration fluctuations remain.

Another feature due to the large layer spacing is a more important role of viscous

effect. Large amount of water between layers cause a stronger viscous hindrance to the movement of the membranes. This is reflected in Eq. (4.30). The denominator of Eq. (4.30) is essentially q_z^2 multiplied by a constant in our experiment; the presence of the $\mu\eta q^4$ term makes this constant approximately 3 instead of 1, and therefore makes Γ three times smaller. This term results from the damping due to the slip flow of the water between the bilayers.

Returning to Eq. (4.21), we solved numerically for the other two roots; with these parameters, they had magnitudes of 10^4 sec^{-1} or greater. We also investigated the possibility that our two decay times might be the result of simply forward scattering by two different modes of Eq. (4.21), rather than forward and backward scattering of only the lowest frequency mode. When D_{33} is large enough and $q_x \sim q_z$, the two higher frequency modes are a pair of propagating "second sound" modes. However, for small values of D_{33}, as we apparently have here, all three roots of Eq. (4.21) are imaginary, and two of them are relatively low frequency. It was, in fact, possible to fit our data to forward scattering by the two lowest frequency roots of Eq. (4.21). The parameters we obtained this way were $d_{eq} = 200\,\text{nm}$, $k_c = 0.08\,k_BT$, and $D_{33} = 1.2\,\text{Pa}$, which give $D_{22} = 9.5\,\text{Pa}$, and $\lambda = 14\,\text{nm}$. These are so far from physically reasonable values that we believe our interpretation of forward and backward scattering from the low frequency mode is the correct one.

6.4 Conclusions

We have investigated the spectrum of light scattered from a homeotropically aligned highly swollen lamellar phase ($d \sim 1800\text{Å}$) in a non-ionic binary system (C12E5 and water), where the Helfrich repulsion is the dominant force between bilayers to stabilize the lamellar order. At each scattering angle we observed an intensity autocorrelation function for the scattered light with two decay times. We identified these as coming

from simultaneous observation of the baroclinic mode in both forward and backward scattering.

We conclude that the Brochard-de Gennes model [7] combined with Helfrich's calculation [6] of the entropic and steric inter-bilayer repulsion quantitatively describes dynamical behavior of the baroclinic mode of highly swollen lamellar phases of non-ionic surfactants.

We found that for highly swollen lamellar phase, it is important to consider the curvature elastic energy in calculating the dispersion relation even for the very oblique momentum transfer case. Because the inter-bilayer repulsion is so weak, the curvature energy leads to the interesting property that the mode relaxation speeds up as $q_{\|}$ becomes smaller. The faster forward scattering branch in Fig. 6-3 is in the crossover region between the baroclinic mode for large q_z and the decoupled undulation mode of $q_z = 0$.

Finally, since the slip coefficient scales as d^2, the damping to the fluctuations of bilayers due to the water in between them plays a more important role in highly swollen systems.

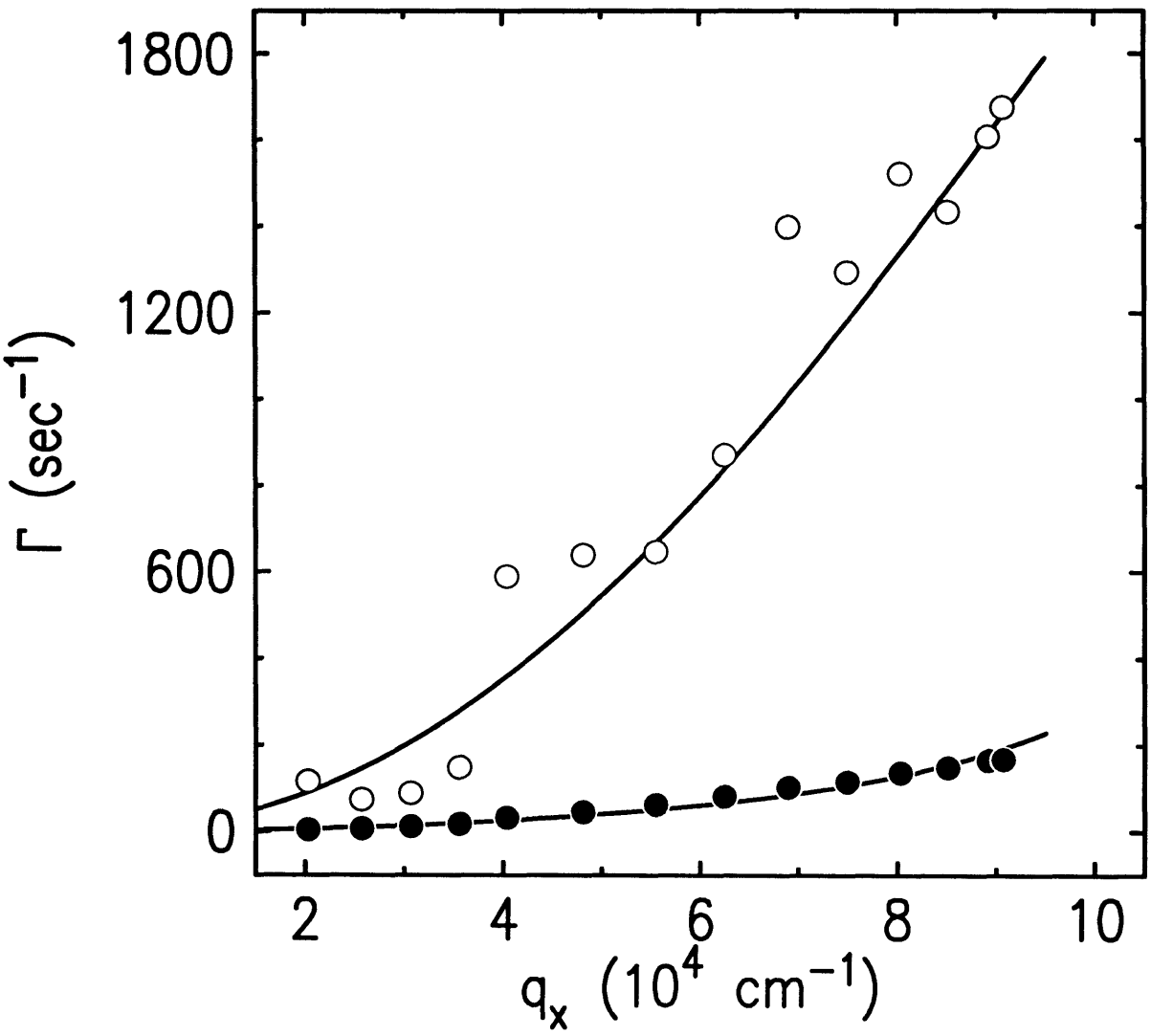

Figure 6-3: q dependence

Chapter 7

Light Scattering from the OBS System

7.1 Introduction

As discussed in Chapter 3, the OBS system has been swollen to produce a layer spacing from 1800$\mathring{A}$ to 1μm. With the layer spacing at this large scale, we can see the Bragg peak simply using visible laser light, while conventional Bragg scattering requires x-rays. In this chapter, we will discuss our experiments and findings of Bragg light scattering from this OBS system. By measuring the positions of the Bragg peaks, we can precisely determine the layer spacings and find a layer spacing dependence on the distance from the top of the liquid. We attempt to explain this observed phenomenon by relating the gravitational compression to the entropic Helfrich repulsion that exists between membranes. Furthermore, we are able to study the intensity lineshape of the Bragg peaks which is closely related to the Landau Peierls instability that is intrinsic to smectic-A liquid crystals.

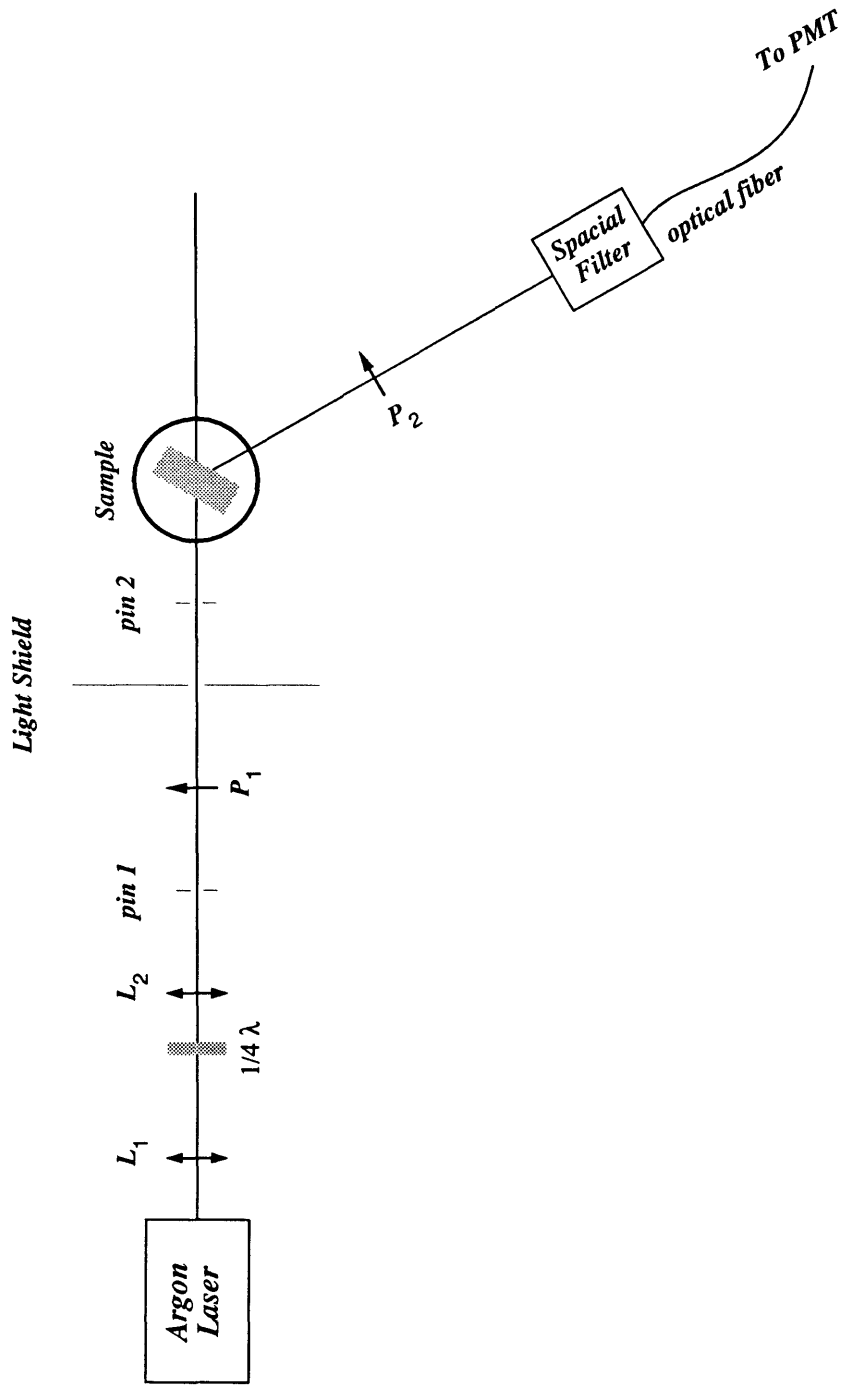

Figure 7-1: Bragg scattering setup

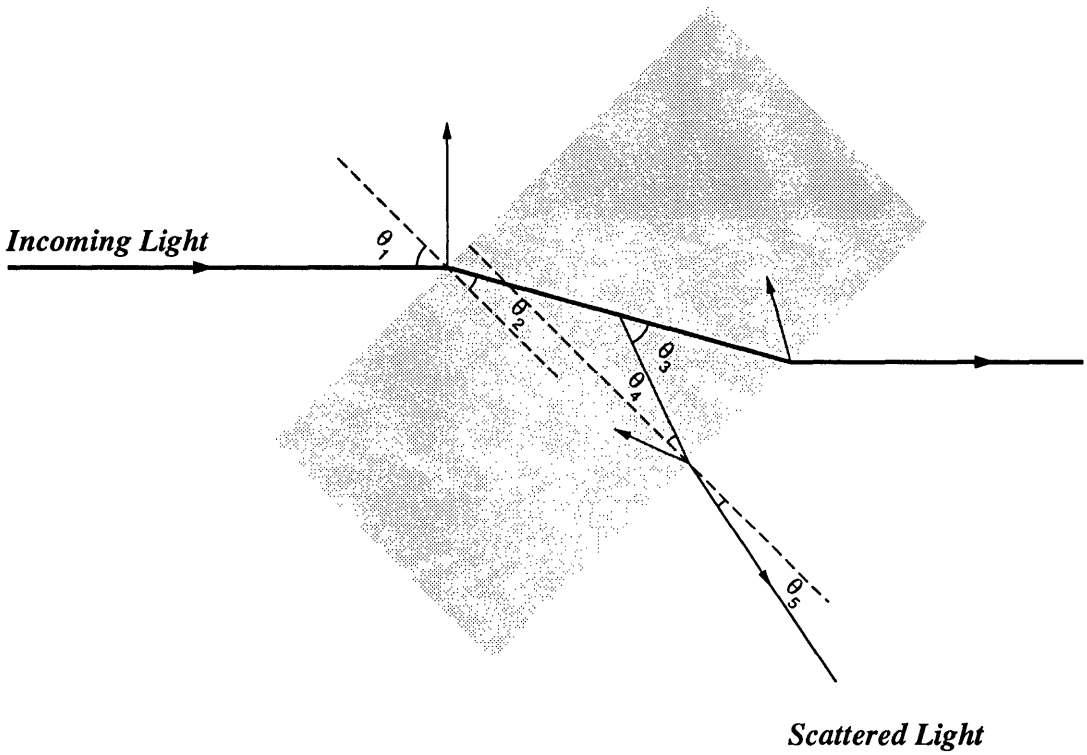

Figure 7-2: Enlarged view of the sample.

7.2 Gravitational Compression of the OBS System

7.2.1 Experiment

In Chapter 2, we discussed how to make OBS swollen phase and found the layer spacing dependence on depth of the illuminated volume from the top of the liquid. To measure this dependence accurately, we build a second light scattering setup which

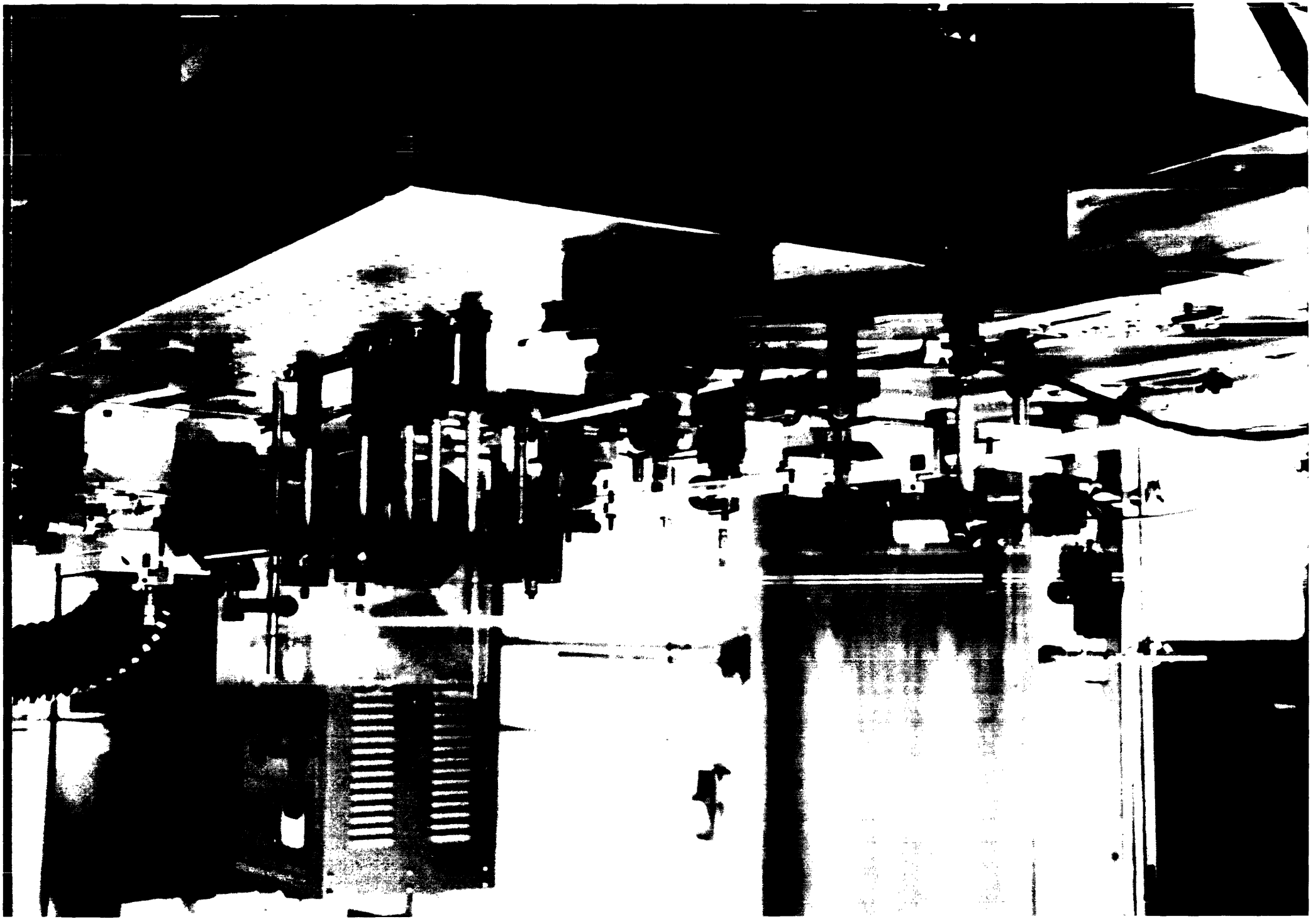

would also be used to measure the Bragg peak lineshape. The top view of the setup is shown in Fig. 7-1. A photograph of the setup is added at the end of this chapter. The setup consists of two metal arms, an arm for incoming light and an arm for receiving the signal. A tall light scattering cell of dimensions $2 \times 10 \times 30mm$ is placed on a stage that can both be moved along the vertical direction and rotated about the vertical axis (z axis). The scattering plane lies horizontally (that is, in the $x - y$ plane in contrast with the first setup). Lenses L_1 and L_2 are used to collimate the beam to a cross section with radius $1mm$ and 0.13° divergence. A 1/4 wave plate changes the linearly polarized beam from the Argon laser into a circularly polarized beam, so that polarizer P_1 can define the polarization of the light incident on the sample. The small pin hole and the fiber tip in the spatial filter define an angular resolution of 0.08° for each angle. Fig. 7-2 shows an enlarged view of the light path near and inside the sample. Instead of putting incoming light at normal incidence onto the glass window of the sample cell, we turn the sample cell to an angle θ_1 so that the angle between the scattered light inside the sample and the normal of the sample-air interface θ_4 is less than the angle of total reflection. In Fig. 7-2, we did not draw the glass windows because they does not change the directions of light paths. To measure the height dependence, we keep θ_1 constant, move the sample in the z direction, and measure the angle of peak intensity by changing θ_5 (the signal receiving arm). Thus,

$$\theta_2 = sin^{-1}\left(\frac{sin\theta_1}{n_1}\right) \tag{7.1}$$

$$\theta_4 = sin^{-1}\left(\frac{sin\theta_5}{n_1}\right) \tag{7.2}$$

$$\theta_3 = \theta_2 + \theta_4 \tag{7.3}$$

where n_1 is the index of refraction of the sample. It is a good approximation to use the index of refraction of decane ($n_1 = 1.412$), since it constitutes more than 90wt.%

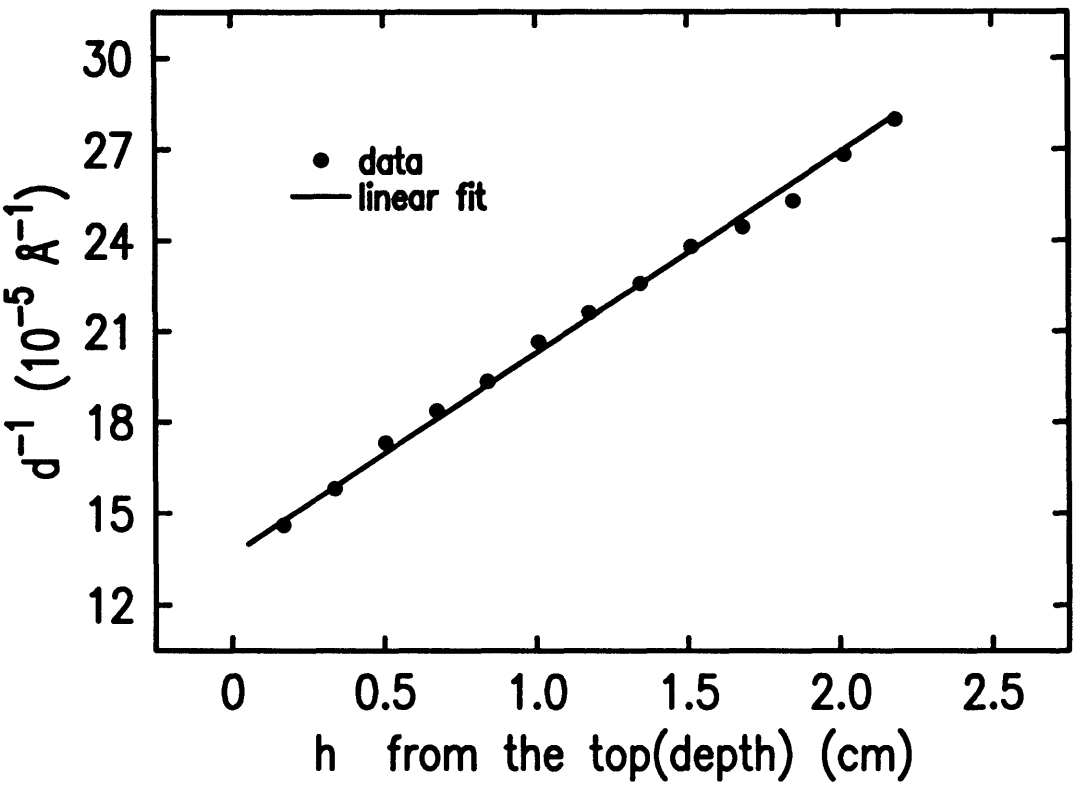

Figure 7-3: Layer spacing distribution

of the phase. The magnitude of momentum transfer q can be found,

$$q = \frac{4\pi n_1}{\lambda} sin\frac{\theta_3}{2} \tag{7.4}$$

At the position of peak intensity, with momentum transfer q_0, the layer spacing of the lamellar phase is $d = 2\pi/q_0$. We plot the layer spacing distribution in Fig. 7-3 where h is the vertical distance of the beam spot from the top surface of the liquid (see Fig. 7-4). it shows that h depends on $1/d$ linearly. The relation can be written as:

$$h = 1.51 \times 10^{-4} d^{-1} - 2.06 \tag{7.5}$$

Both h and d are in cm.

7.2.2 Gravity as a Compressor of Lamellar Phases

To understand the layer spacing dependence in the last section, we model our system as numerous lamellar pieces of finite sizes floating in the background of decane (92wt%) and pentanol (8wt%) solution in random directions shown in Fig. 7-4. The background solvent exerts a hydrodynamic pressure which equals the sum of the atmospheric pressure ($\sim 10^6 erg\ cm^{-3}$) and the pressure due to the weight of the solvent itself ($\sim 10^3 erg\ cm^{-3}$ for a maximum $2.5cm$ height). The latter changes with height, but changes only by 10^{-3} of the total pressure while the layer spacing changes by a factor of 2. Thus it is reasonable to assume that the solvent pressure is not the cause of layer spacing variation. In fact, the solvent pressure is much greater than the inter-membrane forces which is on the order of $D_{22} \sim 1 erg\ cm^{-3}$, so it is reasonable to assume that the solvent in between bilayers and the solvent in the background outside each lamellar piece are freely exchangeable (see Fig. 7-4), so that the solvent pressure acts on each membrane directly. Then, what force serves to compress the whole lamellar piece?

The local density of the inverse bilayer ρ_s can be estimated between 0.82 and 1.25 $g\ cm^{-3}$ using the densities given in Ref. [10]. The uncertainty is introduced because the presence of the co-surfactant pentanol changes the volume of surfactant layers (see Fig. 3-4) and we do not know the percentage of pentanol in the layers. But still, as this density is greater than the background density ρ_b of $0.74 gcm^{-3}$, each bilayer tends to sink. The whole lamellar piece will sink with an effective density:

$$\rho_{eff} = \alpha \frac{w}{d} (\rho_s - \rho_b) \tag{7.6}$$

where w is the thickness of the inverse bilayers. We introduced a factor $\alpha < 1$ to take into consideration that the hydrophobic tail of OBS and that of the pentanol are soluble in decane solution. We can view these lamellar pieces as the basic constituents

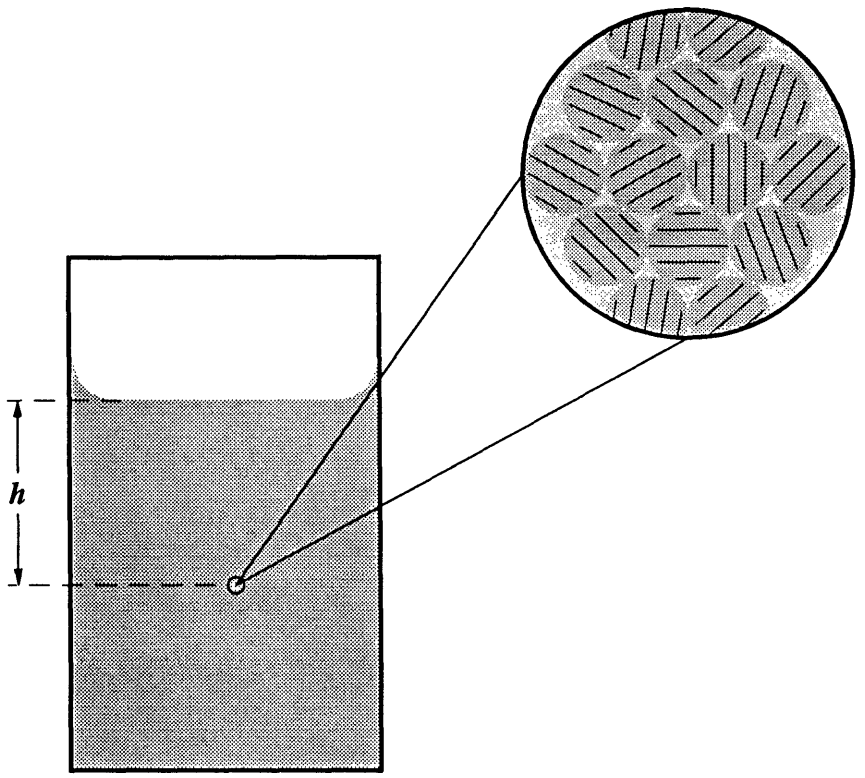

Figure 7-4: A schematic sketch of the lamellar fluid

of a sub-phase of lamellar particles closely packed with density ρ_{eff}.

Since ρ_{eff} can be very small, the reader may wonder whether thermal effects expressed by the Boltzman factor can sustain the lamellar fluid to a certain height. We did the following calculation: Let N be the number density of lamellar particles due to thermal excitation at given height x from the bottom of the container, we have,

$$N = N_0 \, exp\left(-\frac{\rho_{eff} v g x}{k_B T}\right) \tag{7.7}$$

where N_0 is the number density at the bottom, v is the average volume of a lamellar particle. The above equation defines a length,

$$x_0 = \frac{k_B T}{\rho_{eff} v g} \tag{7.8}$$

as the average height the lamellar particles can be excited to by the Boltzman factor.

ρ_{eff} can be calculated from Eq. (7.6). The discounted net density $\alpha(\rho_s - \rho_b)$ is estimated to be 0.1 $g\ cm^{-3}$, the layer thickness $w = 20\mathring{A}$ [9]. Thus, at a typical layer spacing $d = 4000\mathring{A}$, $\rho_{eff} \sim 5 \times 10^{-4}\ g\ cm^{-3}$.

The sizes of the lamellar particles are obtained from the fitting of the Bragg peaks with the Landau-Peierls theory, which will be discussed in Section 7.4. The result is: the average dimension of lamellar particles is 19 μm. Thus, $v \sim 2.9 \times 10^{-8}\ cm^{-3}$. Using these values, we got $x_0 \sim 2.8 \times 10^{-5}\ cm$. So, if the lamellar pieces could be squeezed into zero volume, they would all stay within $2.8 \times 10^{-4}\ cm$ from the bottom of the container. Therefore, the lamellar particles are too heavy to be excited by the Boltzman factor.

Since lamellar pieces can not penetrate into each other, each of them will be under a pressure due to their own density ρ_{eff}. This pressure is locally hydrodynamic in the sense that it exerts the same amount of pressure in all directions, because the lamellar pieces are macroscopically small.

It should be emphasized that this pressure is different from the previously mentioned hydrodynamic pressure of the decane/pentanol diluent, since the latter acts on both sides of all layers, although its value is much greater, it is not directly related to the layer spacing change.

Now, let us estimate the magnitude of this pressure. At layer spacing $d = 4000\mathring{A}$, $h = 1.72\ cm$, the average density of the lamellar particles $\rho_{eff} \sim 5 \times 10^{-4}\ g\ cm^{-3}$,

this gives the pressure due to gravity,

$$p_g \simeq \rho_{eff} h g \simeq 0.86\ erg\ cm^{-3} \tag{7.9}$$

On the other hand, the counter pressure from the internal Helfrich repulsion p_h is:

$$p_h = \frac{\partial V_h}{\partial d} = \frac{3\pi^2}{64}\frac{(k_B T)^2}{k_c d^3}, \tag{7.10}$$

where V_h is the Helfrich free energy.

At layer spacing $d = 4000\mathring{A}$, if we let $k_c = 0.5 k_B T$, Eq. (7.10) gives $p_h = 0.92 ergcm^{-3}$. So, p_g and p_h have the same of order of magnitude. It is quite possible that the layer spacing variation with height is the result of a force balance between gravity and the Helfrich interaction.

We have not been able to explain the linear behavior h *vs.* d more quantitatively. Further experimental and theoretical investigation is being conducted.

7.3 Co-surfactant Concentration in Membranes

The finding of the layer spacing distribution provides us an experimental framework to study several physical variables as functions of d. In this section, we propose a model about the variation of the concentration of co-surfactant, pentanol, in the membranes as d changes.

Similar to the pseudo-phase model for microemulsion system [23], We treat the surfactant membranes and the decane/pentanol solvent between the membranes as two separate phases (pseudo-phase) in equilibrium as shown in Fig. 3-4 in Chapter 3. The alcohol (pentanol) equilibrium between the two phases obeys the equation:

$$\mu_A^o = \mu_A^s \tag{7.11}$$

where μ_A^o and μ_A^s are the chemical potentials of pentanol in the oil (decane/pentanol) phase and surfactant membrane phase respectively. In the oil phase,

$$\mu_A^o = \mu_A^{Ref_o} + k_B T \log \phi_A^o \tag{7.12}$$

where $\mu_A^{Ref_o}$ is the chemical potential of pure bulk pentanol and ϕ_A^o is the volume fraction of pentanol in the oil phase. Because pentanol is soluble in decane and its density is close to decane, gravity should have little effect on its concentration in the oil phase. Therefore, ϕ_A^o and μ_A^o should be constants throughout the lamellar fluid.

On the other hand, the chemical potential of pentanol in the membranes can be calculated, including the contribution from thermal fluctuations of membranes, as,

$$\mu_A^s = \mu_A^{Ref_s} + k_B T \log \phi_A^s + A \frac{3\pi^2}{128} \frac{(k_B T)^2}{k_c d^2}, \tag{7.13}$$

where $\mu_A^{Ref_s}$ is the chemical potential of pure pentanol aligned in a layer shape and ϕ_A^s is the area fraction occupied by pentanol in the membrane phase. A is the average area of surfactant/pentanol head.

From Eq. (7.11) to (7.13), we get,

$$k_B T \log \phi_A^s + A \frac{3\pi^2}{128} \frac{(k_B T)^2}{k_c d^2} = -\beta \tag{7.14}$$

where β is only a function of temperature. With condition, $A/d^2 \ll 1$, the above equation yields,

$$\phi_A^s = \phi_0 \left(1 - \frac{3\pi^2}{128} \frac{k_B T}{k_c} \frac{A}{d^2}\right) \tag{7.15}$$

where $\phi_0 = exp(-\beta/k_B T)$. Eq. (7.15) shows that lamellar layers at higher positions have slightly more co-surfactant than those at lower positions. Physically speaking, thermal fluctuations of large amplitude at higher positions (corresponding to larger

layer spacing) reduce the free energy of the layer, therefore, the layer needs slightly more co-surfactant to keep the chemical potential of the co-surfactant the same as the value in the oil phase.

Eq. (7.15) can be tested in future experiment.

7.4 Landau-Peierls Instability

In this section, we turn our attention to the measurement and analysis of the lineshape of the Bragg peaks. It was proposed by Landau and Peierls [25, 26] theoretically that translational order as it occurs in a three dimensional solid can not exist in two dimensions because it is destroyed by thermal fluctuations. For a two dimensional system, it was predicted that a transition occurs to a state of quasi-long-range order in which the positional correlation functions do not extend to infinity, but decay algebraically as some power of distance. This behavior is called the Landau-Peierls instability. A closely related phenomenon has been predicted and observed [8] in a thermotropic smectic-A liquid crystal for the first time and later in swollen lyotropic lamellar phases [27, 11]. These liquid crystal structures are close analogies of two dimensional systems in that the calculations of the thermal fluctuations are similiar, and the thermal fluctuations prevent the smectic ordering to long range.

To understand the Landau-Peierls instability in liquid crystals, we recall Ref. [8] and Eq. (4.3) in Chapter 4 of this thesis. A stacked membrane system can be described by a group of harmonic modes, each mode defined by $u(\boldsymbol{q})$, with an energy,

$$E_{\boldsymbol{q}} = \frac{1}{2}\left(Bq_{\parallel}^2 + \frac{1}{2}\kappa q_{\perp}^4\right) u^2(\boldsymbol{q}) \tag{7.16}$$

When we take ensemble average over both sides of the above equation, and apply the equipartition theorem, the real space mean square amplitude of fluctuations can be

found,

$$\begin{aligned}\langle u^2 \rangle &= \frac{1}{(2\pi)^3} k_B T \int_{-q_0}^{q_0} dq_{\|} \int_{q_{min}}^{q_{max}} \left(B q_{\|}^2 + \frac{1}{2} K q_{\perp}^4 \right)^{-1} 2\pi q_{\perp} dq_{\perp} \\ &= \frac{k_B T}{4\pi\sqrt{BK}} k_B T \log\left(\frac{L}{a}\right) \end{aligned} \tag{7.17}$$

where q_0 is the upper cut off for $q_{\|}$. The cut off wave vectors for $q_{\perp}$ are $q_{min} = \frac{2\pi}{L}$ and $q_{max} = \frac{2\pi}{a}$ with L the dimension of domain size and a the distance between the head group molecules.

Clearly, if L is infinite, the amplitude of fluctuations will be divergent so that thermal fluctuations will destroy any long range order. Thus for a smectic-A or a layered structure phase in three dimensions, there is no true long range order.

To calculate the Bragg peak lineshape, we first calculate the the positional correlation function [8]:

$$\mathcal{G}(\boldsymbol{r}) = \langle e^{iq_0[u(r)-u(0)]} \rangle \tag{7.18}$$

$\mathcal{G}$ is calculated in Appendix C with harmonic approximation, the result is the Caille [28] function,

$$\mathcal{G}(\boldsymbol{r}) \sim e^{-2\gamma\eta} \left(\frac{1}{x^2+y^2}\right)^{\eta} exp\ -\left[\eta E_1\left(\frac{x^2+y^2}{4\lambda z}\right)\right] \tag{7.19}$$

with $\lambda = \sqrt{K/B}$ and η given by

$$\eta = \frac{k_B T q_0^2}{8\pi\sqrt{BK}} \tag{7.20}$$

and γ is Euler's constant; $E_1(x)$ is an exponential integral function (see Abramowitz

& Stegun [29]),

$$E_1(x) \equiv \int_{-x}^{\infty} \frac{e^{-t}}{t} dt \tag{7.21}$$

$$= -\gamma - \log x - \sum_{n=1}^{\infty} \frac{(-1)^n x^n}{n(n!)} \tag{7.22}$$

The Fourier transformation of $\mathcal{G}(\boldsymbol{r})$ gives the lineshape $S(\boldsymbol{q})$, it has simple forms in directions both parallel and perpendicular to the normal of the membranes (Appendix C),

$$S\left(0, 0, q_{\|}\right) \sim \frac{1}{\mid q_{\|} - q_0 \mid^{2-\eta}} \tag{7.23}$$

and

$$S(q_x, q_y, q_0) \sim \frac{1}{q_{\perp}^{4-2\eta}} \tag{7.24}$$

In the above calculations, we have assumed a single domain liquid crystal of infinite size. In a real system such as the OBS system in our experiment, lamellar pieces have finite sizes and light signals are scattered from many lamellar pieces randomly oriented in space, we have to consider the finite size effect and powder averaging.

First of all, we discuss the finite size effect. Dutta and Sinha [30] have analyzed the finite size effect in 2-D crystals. Their result includes introducing a Gaussian factor $exp - (r^2\pi/L^2)$ in the Fourier transformation integral in calculating $S(\boldsymbol{q})$. Although each crystal piece is sharp-edged, the Gaussian form comes from the averaging of many domains of randomly distributed sizes[30]. Safinya *et al.* [27] considered this Gaussian factor in calculating $S(\boldsymbol{q})$ in liquid crystals,

$$S_{\text{F.S.}}(\boldsymbol{q}) \sim \int_{-\infty}^{\infty} d^3\boldsymbol{r} e^{-(r^2\pi/L^2)} \mathcal{G}(\boldsymbol{r}) e^{i(\boldsymbol{q}-\boldsymbol{q}_0)\cdot\boldsymbol{r}} \tag{7.25}$$

where $\boldsymbol{q}_0$ is in the z direction and $\mathcal{G}$ has the form of Eq. (7.19) in the same coordinate system. L is the dimension of the liquid crystal pieces. In order to examine the asymptotic behavior of $S_{\text{F.S.}}$ at large $\mid \boldsymbol{q} - \boldsymbol{q}_0 \mid$, we rewrite Eq. (7.25),

$$S_{\text{F.S.}}(\boldsymbol{q}) \sim \int d^3\boldsymbol{r}\ \mathcal{G}(\boldsymbol{r})\, exp\left[i\,\frac{(\boldsymbol{q}-\boldsymbol{q}_0)}{\pi/L} - \frac{\boldsymbol{r}}{L}\right]\cdot\frac{\boldsymbol{r}}{L}\pi \tag{7.26}$$

We can always choose $\mid \boldsymbol{q} - \boldsymbol{q}_0 \mid \gg \pi/L$, so that $r < L \mid \boldsymbol{q} - \boldsymbol{q}_0 \mid / \left(\frac{\pi}{L}\right)$ covers the integration volume beyond which $\mathcal{G}(\boldsymbol{r})$ is too small to have a significant contribution to the integral. Within this integration volume, the second term in the exponential brackets in Eq. (7.26) contributes little to $S_{\text{F.S.}}$ in the contour integral, therefore can be neglected, Eq. (7.26) becomes,

$$S_{\text{F.S.}}(\boldsymbol{q}) \sim \int\ \mathcal{G}(\boldsymbol{r})\, exp\ i(\boldsymbol{q}-\boldsymbol{q}_0)\cdot\boldsymbol{r} \tag{7.27}$$

Eq. (7.27) is indistinguishable from the case when the lamellar pieces are infinitely large. The conclusion is, the finite size has only a very small effect on the lineshape far away from the Bragg peak. Eq. (7.23) and (7.24) should be applicable at large $\mid \boldsymbol{q} - \boldsymbol{q}_0 \mid$. On the other hand, as pointed out by Dutta and Sinha, finite-size effect becomes important at small $\mid \boldsymbol{q} - \boldsymbol{q}_0 \mid$. They round off the otherwise cusped $S(\boldsymbol{q})$ near the Bragg point.

The powder averaging effect is incorporated by integrating Eq. (7.25) over $\boldsymbol{q}$ in all solid angles [27],

$$\langle S(\boldsymbol{q})_{\text{F.S.}}\rangle_{\text{P.A.}} \equiv \mathcal{S}(q) \sim \int d\Omega_{\boldsymbol{q}} \int d^3\boldsymbol{r} e^{-(r^2\pi/L^2)}\ \mathcal{G}(\boldsymbol{r})\, e^{i(\boldsymbol{q}-\boldsymbol{q}_0)\cdot\boldsymbol{r}} \tag{7.28}$$

$$\sim \int d^3\boldsymbol{r}\ e^{-(r^2\pi/L^2)}\ \mathcal{G}(\boldsymbol{r})\, e^{i\boldsymbol{q}_0\cdot\boldsymbol{r}} \int_0^\pi d(cos\zeta)\ e^{qrcos\zeta} \tag{7.29}$$

$$\sim \int_0^\infty dr\ e^{-r^2\pi/L^2} r^{1-2\eta} sin(qr) \int_0^1 d\alpha\ \frac{cos(q_0 r\alpha)}{(1-\alpha^2)^\eta}$$

$$\times exp - \eta E_1 \left[\frac{r}{4\lambda}\left(\frac{1}{\alpha} - \alpha\right)\right] \tag{7.30}$$

where ζ is the angle between $\boldsymbol{r}$ and $\boldsymbol{q}$. The last equation is written in spherical coordinates whose polar axis is in the direction of $\boldsymbol{q}_0$, and $\alpha = cos\theta$.

There is no analytical solution to Eq. (7.30). A numerical fitting program based on Eq. (7.30) is written (see Appendix B) which requires large amount of CPU time (up to days on a SUN workstation). Numerical fitting to our experimental data is currently being conducted.

In fitting our experimental data, we have also tried a simpler but less rigrous approach. The narrow central peaks of the experimental lineshapes which will be presented in the next section, show that the sizes of the lamellar pieces are reasonablely large, so that we can first consider the powder-averaged Landau-Peierls' lineshape at large $q - q_0$, which is a power law,

$$\mathcal{I}(p) \sim \frac{1}{p^{\phi}} \tag{7.31}$$

where $p = \mid q - q_0 \mid$ and $\phi = 1 - \eta$ according to Safinya *et al.* [27]. Eq. (7.31) would have a one dimensinal Fourie transform, provided $0 < \phi < 1$, given by:

$$\begin{aligned} \mathcal{G}(z) &= \frac{1}{2\pi}\int_{-\infty}^{\infty} \frac{e^{ipz}}{p^{\phi}} dq \\ &\sim \frac{1}{\mid z \mid^{1-\phi}} \end{aligned} \tag{7.32}$$

We could transform this back to the momentum space, but with a gaussian cutoff to incorporate the finite size effect, that gives,

$$\mathcal{S}(p) = \int_{-\infty}^{\infty} \mid z \mid^{\phi-1} e^{-z^2/L^2} e^{-iqz} dz$$

$$\sim \Gamma(\phi/2)\, L^{\phi} M\left(\frac{\phi}{2}; \frac{1}{2}; -\frac{(q-q_0)^2 L^2}{4}\right) \tag{7.33}$$

where M is the Kummer's function [31].

In the case of lamellar phases obeying the Helfrich formulation for the membrane-membrane interaction (see Eq. (4.12)),

$$B \equiv D_{22} \sim \frac{1}{k_c d^3} \tag{7.34}$$

The value of η can be calculated theoretically by combining Eq. (7.34) and Eq. (7.20). It turns out to be independent of k_c, d and T for layer spacings as large as our OBS system. For a smaller layer spacing, η does depend slightly on d, $\eta \simeq 1.33\,(1-\zeta/d)^2$ when the layer thickness ζ can not be neglected [27]. For highly swollen lamellar phases, the predicted value of η depends solely on the coefficient of the Helfrich interaction. This could give a value of $\eta > 1$.

Interestingly, $\phi = 1 - \eta$ sets a upper limit for η. That is, η has to be smaller than 1 for Eq. (7.31) to generate a Bragg peak. Because Eq. (7.31) is an approximation at large p, whether this upper limit is a true condition or not is not clear.

Experimentally, the value of $\eta > 1$ has never been observed. Larche *et al.*[11] measured the Bragg peak in a similar OBS system with an oriented sample and found $\eta = 0.7$. In the next section, we will discuss our Bragg peak measurements from our OBS powder sample. The layer spacing distribution allows us to measure Bragg peaks from $d = 4000\mathring{A}$ to $d = 10000\mathring{A}$ with the same sample.

7.4.1 Bragg Peak Measurement

The Bragg light scattering setup is the same as described in Fig. 7-1 and Fig. 7-2 except that:

1). The polarizations $\boldsymbol{i}$ and $\boldsymbol{f}$ are set in the plane of scattering.

2). $\theta_1 = tan^{-1}\left(\frac{1}{n_1}\right)$, the Brewster angle.

These two conditions guarantee that the multiple reflections from the two interfaces, which would contribute to the broadening of the peak, are minimized.

Signals were recorded by the same photo multiplier and auto-correlator that were used in the dynamic light scattering of C12E5 lamellar phases described in Chapter 6. The baseline of the time auto-correlation function should be proportional to the scattered intensity. The Argon laser provides a well collimated beam with power $\sim$ 100 mW, but unfortunately, the laser light has an intrinsic 10% modulation at 120 Hz. We replace the Argon laser by a new Helium-Neon red laser to do dynamic light scattering and find that the characteristic correlation time ranges from 0.02 sec at positions far away from the peak to 0.5 sec near the peak point. This decay rate dependence on q near Bragg peak deserves further analysis (see Section 7.5). For the intensity measurement, the blue light of the Argon laser provides a more suitable range of angles to observe. But the modulation at 120 Hz and the variation of the decay rate with q may introduce errors in the determination of base line by the auto-correlator. To minimize this effect, we choose sample time τ to be much greater than the decay time even at angles very close to the center of Bragg peak.

Because the lamellar pieces are much smaller than the path length of the container and the sample is an extremely dilute, transparent fluid, the lamellar phase stays in a powder form randomly distributed in orientation, instead of being oriented by the glass walls. This is supported by the observation of a smooth Bragg ring on a paper screen. The Bragg rings measured when the glass walls are turned in direction also satisfy the Bragg angle conditions for powder sample, Eqs. (7.3) and (7.4).

Since we are only changing the receiving arm, $\boldsymbol{q}$ changes both in magnitude and in direction. Due to the uniform distribution of lamellar piece orientation, the intensity of the scattered light is independent of the direction of $\boldsymbol{q}$. Its dependence on q should

in principle be given by Eq. (7.30).

Let I_L be the measured intensity flux in the lab, let I_R be the real intensity flux before the scattered light comes out of the sample. The differential intensity per unit solid angle can be calculated according to (see Fig. 7-2):

$$\frac{dI_R}{d\theta_4} = n_1 \left(\frac{1}{1-r^2}\right)\left(\frac{cos\theta_4}{cos\theta_5}\right) \frac{dI_L}{d\theta_5} \tag{7.35}$$

where r is the reflection coefficient,

$$r = \frac{tan\,(\theta_4 - \theta_5)}{tan\,(\theta_4 + \theta_5)} \tag{7.36}$$

Now, we consider the instrumental resolution and the finite size effect. The incoming beam is collimated to within a 0.13° divergence. This is converted to an uncertainty of momentum transfer $\Delta q = 158cm^{-1}$ for a typical layer spacing $d = 5434.4\mathring{A}$ using Eq. (7.3). In the receiving arm, P_1 and the spatial filter (see Fig. 7-1) define a direction for the scattered beam at each angle so that any light rays deviating from the line by more than 0.08° can not get into the fiber tip in the spatial filter. This corresponds to a momentum resolution $\Delta q = 123cm^{-1}$. The total instrumental resolution should then be below $300cm^{-1}$ which is small compared with the Bragg peak width ($\sim 10^3$ to $10^4 cm^{-1}$). On the other hand, the finite size effect may not be as small. This will be seen from the data.

We measured the differential intensities vs. q for 3 different layer spacings and plot the Bragg peaks from Fig. 7-5 to Fig. 7-7. The solid lines are least square fits to the Kummer's function expressed by Eq. (7.33) plus a constant background term and a linear background term. The results of the fitting parameters are presented below each graph, d, L and η are readily obtained, and are put at the upper left cornor of each graph.

The Kummer's function resembles a power law at large $\mid q - q_0 \mid$, but rounds off at small $\mid q - q_0 \mid$. This can be seen from the graphs. Since $L \sim 12$ to $21\mu m$, the departure of the lineshape from a power law ocurs within $\mid q - q_0 \mid < \pi/L \simeq 2 \times 10^3 cm^{-1}$. The central broadening characterized by π/L should be the combined effect of the finite size and the finite instrumental resolution. From the last paragraph, we can see that the instrumental resolution is too small to cause the observed broadening, therefore, the finite size effect dominates the broadening, thus L should give the average dimension of the lamellar pieces which is about $19 \pm 7\ \mu m$.

The value of η varies for different d, which gives the uncertainty of η, therefore, $\eta = 0.47 \pm 0.09$. The value of η measured by Larche *et al.* [11] in an oriented OBS sample is $\eta = 0.7$.

7.5 Dynamics Near the Bragg Peak

As we approach the end of this thesis, we present a preliminary result of dynamic light scattering near the Bragg peak. The set up and sample are the same as in the last section. The diffusion time constant also shows a peak at the intensity Bragg peak. Fig. 7-8 shows the diffusive frequency of the time correlation function vs. q. It can be fitted by $(q - q_0)^2$ on both sides of the peak as shown in the second and third graph in Fig. 7-8.

7.6 Conclusion

We discovered a layer spacing distribution as a function of depth of the observed phase region in a vertical cell containing OBS 4-component lamellar phases. We attempt to interpret the the finding as the result of force balance between the gravitational pressure of the lamellar fluid and the internal Helfrich repulsion between membranes.

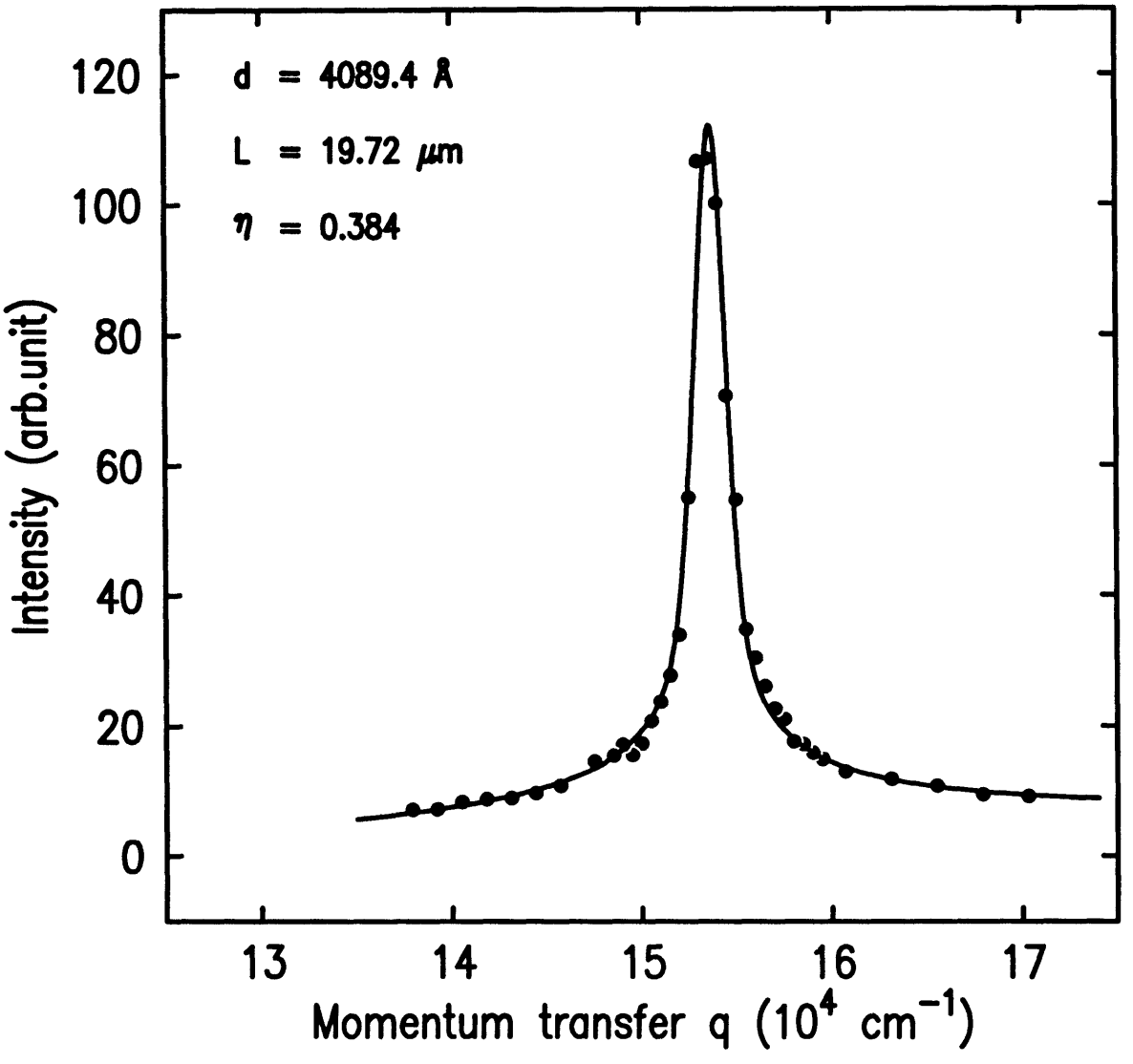

χ^2 = 0.2314
Constant BG term = −13.4±5.1
Linear BG term = 14±5.2
Coefficient = 111.4±4
Q0 = 153645±31
Q0*L = 303±18
Phi = 0.616±0.028

Figure 7-5: Bragg peak and the fit using Kummer's function

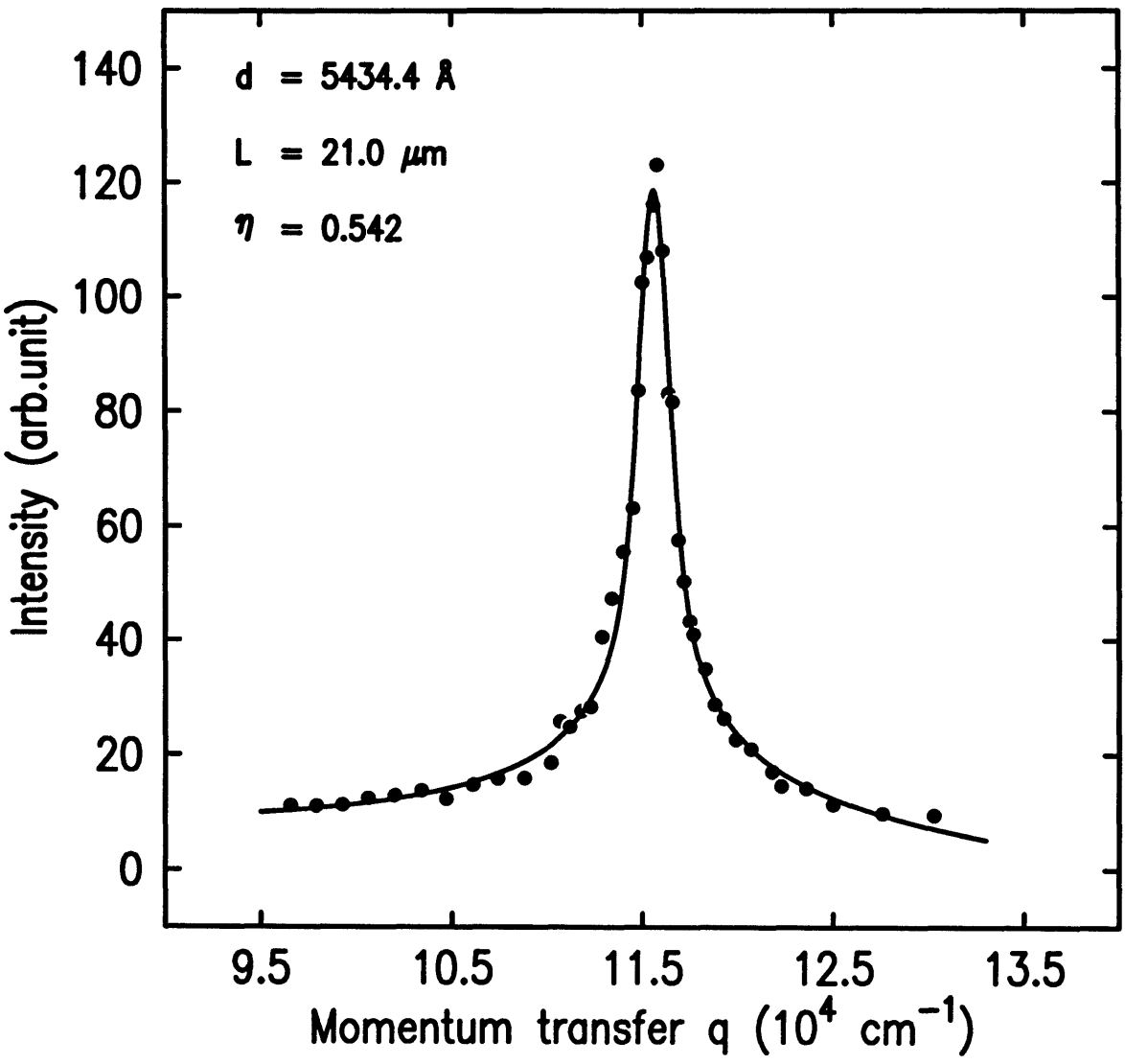

χ^2 = 0.2444
Constant BG term = 8.5±4.3
Linear BG term = −18.6±4.4
Coefficient = 128.7±4.5
Q0 = 115618±28
Q0*L = 243±16
Phi = 0.458±0.028

Figure 7-6: Bragg peak and the fit using Kummer's function

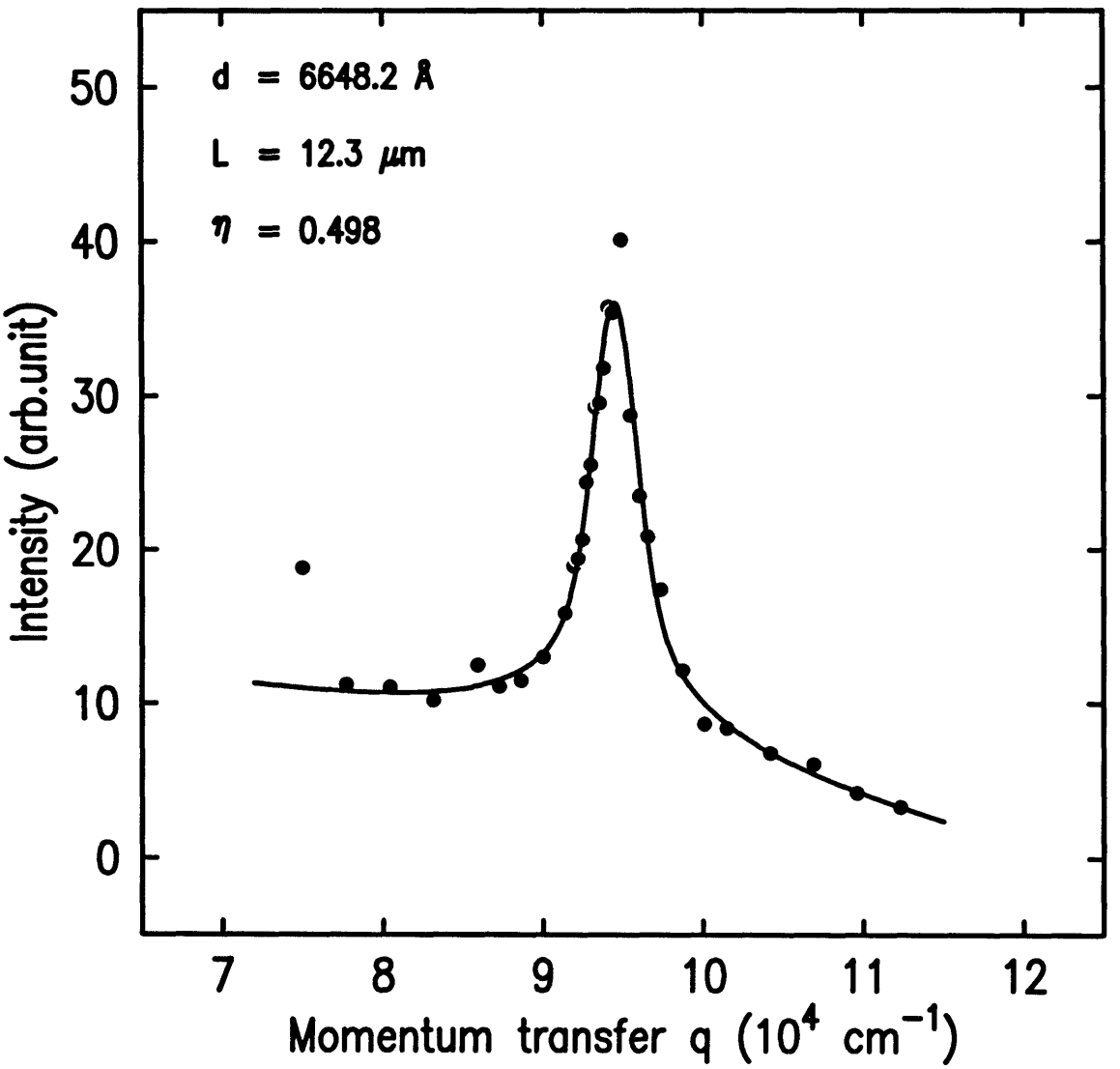

χ^2 = 0.0882
Constant BG term = 22.2±3.9
Linear BG term = −20±2.4
Coefficient = 33.9±2.4
Q0 = 94509±54
Q0*L = 116±11
Phi = 0.502±0.069

Figure 7-7: Bragg peak and the fit using Kummer's function

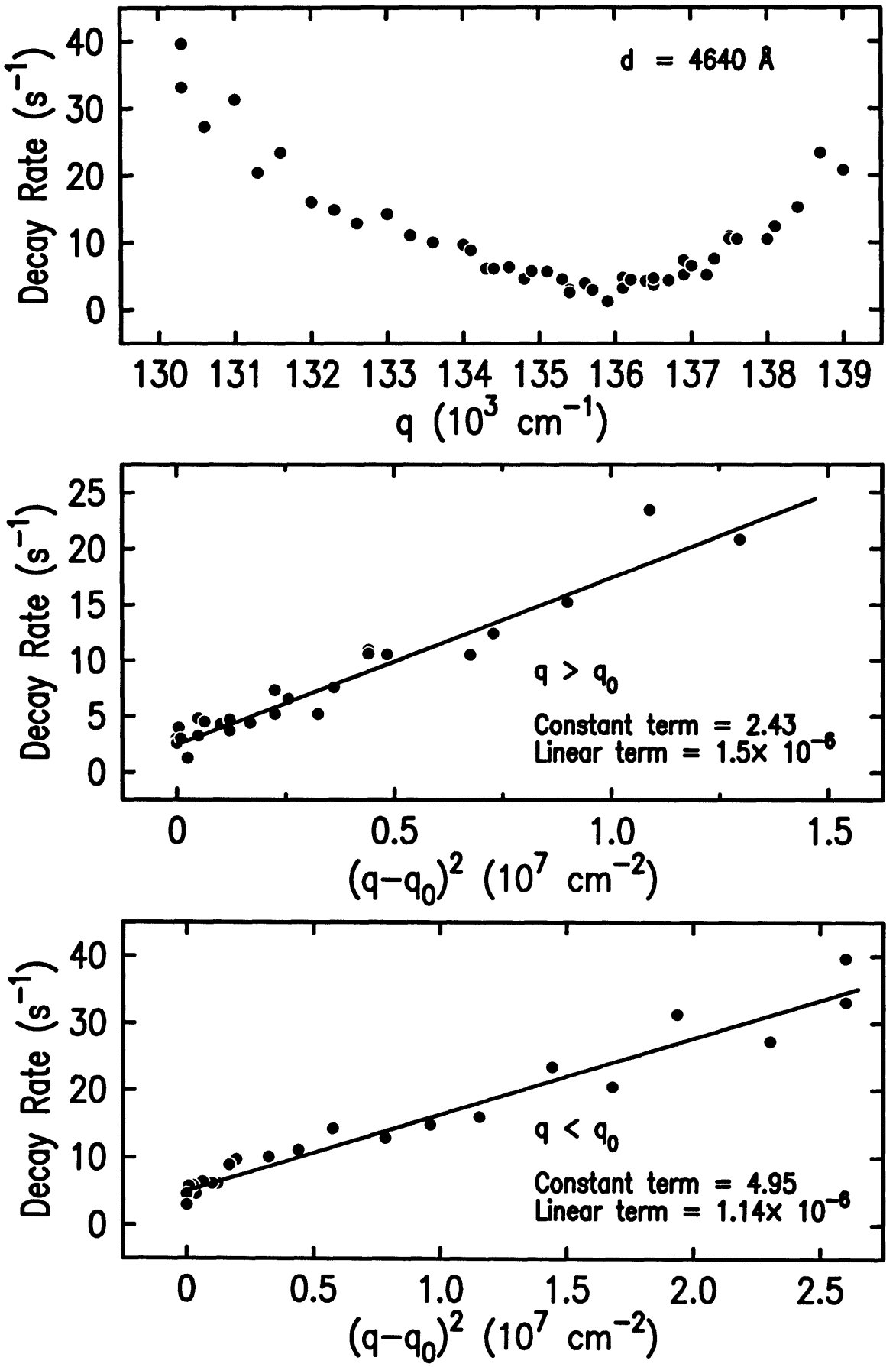

Figure 7-8: Dynamics near the Bragg peak

We also propose a model to calculate the amount of co-surfactant pentanol in the membranes as a function of the layer spacing.

Furthermore, a layer spacing distribution over depth enables us to measure consistently the Bragg peak lineshapes at different layer spacings. We have discussed the framework of the Landau-Peierls instability as applied to highly swollen lamellar phase, the effects of finite size and powder averaging, and are able to fit our experimental data with a Kummer's function, which is a good approximation to describe the Landau-Peierls instability in our system. We find that the power law exponent $\eta = 0.47 \pm 0.09$, independent of the layer spacing within our experimental accuracy, in the range of $d = 4000\mathring{A}$ to $d = 1\mu m$.

Finally, we have conducted dynamic light scattering near the Bragg peak at one layer spacing, and find an approximate relation, $\omega \sim (q - q_0)^2$, where ω is the imaginary decay frequency of the dynamic process measured.

Appendix A

Molecular Properties of C12E5 and OBS

1). C12E5

Full Name: Pentaethylene Glycol Monododecyl Ether.

Moleuclar Form: $CH_3(CH_2)_{11}(OCH_CH_2)_5OH$.

Molecular Weight: 406.61.

Density: 0.963 at room temperature.

Purchased from Fluka.

2). OBS

Full Name: 4-Octylbenzenesulfonic Acid, Sodium Salt.

Moleuclar Form: $CH_3(CH_2)_7C_6H_4SO_3Na$.

Molecular Weight: 292.38.

Purity: 98%

Purchased from Aldrich Chem. Co.

Appendix B

Comments on Computer Files Related to the Thesis

The computer we use is a NeXT Workstation, with address name:

complex.mit.edu.

The general directory is: /home/cyzh/

The thesis is in: /home/cyzh/phd.d/

The oven temperature calibration: /home/cyzh/temp.d/

The DLS from polystyrene latex sphere: /home/cyzh/polyst.d/

The DLS from vesicles: /home/cyzh/vesicle.d

The DLS from C12E5/Water system: /home/cyzh/c12e5lam4.d/

The OBS sample height dependence: /home/cyzh/obs4.20.d/

The OBS Bragg light scattering: /home/cyzh/obs105.d/obs10.5*.d/

The dynamics near the Bragg peak: /home/cyzh/obs525.d/

The fitting program for Eq. (7.30): /home/cyzh/plot_func/lpsph.5.c

The fitting program for the Kummer's function: /home/cyzh/plot_func/kummer.5.c

Appendix C

Notes on Landau-Peierls Line Shape Calculation

Landau Peierls Calculation in a Smectic-A

[Written by J. D. Litster]

The elastic free energy for layer displacements is

$$\int \mathcal{F}_{el}\, d\boldsymbol{r} \;=\; \sum_{q} (B q_{\|}^2 \;+\; \chi_a H^2 q_{\perp}^2 \;+\; K_1 q_{\perp}^4)\, u^2(\boldsymbol{q}) \tag{1}$$

The scattering with respect to the Bragg peak is given by the Fourier transform of the correlation function:

$$\mathcal{G}(\boldsymbol{r}) = \langle e^{-iq_0[u(r)-u(0)]} \rangle \tag{2a}$$

$$= e^{q_0^2[\langle u(r)-u(0)\rangle - \langle u(0)^2\rangle]} \text{ (harmonic approximation)} \tag{2b}$$

$$= \exp\left[\frac{kTq_0^2}{(2\pi)^3} \int \frac{e^{-q\cdot r} - 1}{B q_{\|}^2 + K_1 q_{\perp}^4}\, d\boldsymbol{q} \right] \text{ (when } H = 0) \tag{2c}$$

Thus we need to evaluate:

$$\frac{kTq_0^2}{(2\pi)^3} \int \frac{e^{q\cdot r} - 1}{B q_{\|}^2 + K_1 q_{\perp}^4}\, d\boldsymbol{q} \tag{3}$$

which is most easily done in cylindrical coordinates, with $x^2 + y^2 = r^2$ and $\lambda = \sqrt{K_1/B}$.

$$\frac{1}{(2\pi)^3} \int_0^{2\pi} d\theta \int_0^{\infty} q_{\perp}\, dq_{\perp} \int_{-\infty}^{\infty} dq_z \frac{e^{-iq_z z - iq_{\perp} r\cos\theta} - 1}{B q_z^2 + K_1 q_{\perp}^4}$$

$$= \frac{1}{2\pi^2 B} \int_0^{\infty} q_{\perp}\, dq_{\perp} \int_0^{\infty} dq_z \frac{\cos(q_z z)\, J_0(q_{\perp} r) - 1}{q_z^2 + \lambda^2 q_{\perp}^4} \text{ (using G\&R 8.411.1)}$$

$$= \frac{1}{4\pi B\lambda} \int_0^{\infty} dq_{\perp} \frac{J_0(q_{\perp} r) e^{-\lambda z q_{\perp}^2} - 1}{q_{\perp}} \text{ (using G\&R 3.723.2 and 2.124.1)}$$

Note that in these expressions z is really $|z|$. The Bessel function can be expanded according to Abramowitz & Stegun formula 9.1.12. Also using Abramowitz & Stegun formulas 5.1.11 and 5.1.39 along with G&R 3.381.4, one obtains for Eq. (3):

$$\frac{kTq_0^2}{4\pi B\lambda} \left[\int_0^{q_{max}} dq_{\perp} \frac{e^{-\lambda z q_{\perp}^2} - 1}{q_{\perp}} + \sum_{m=1}^{\infty} \frac{(-1)^m r^{2m}}{4^m (m!)^2} \int_0^{\infty} e^{-\lambda z q_{\perp}^2} q_{\perp}^{2m-1} dq_{\perp} \right]$$

$$= -\frac{kTq_0^2\lambda}{4\pi K_1} \left[\int_0^{\lambda z q_{max}^2} \frac{1 - e^{-t}}{2t} dt - \sum_{m=1}^{\infty} \frac{(-1)^m}{2(m!)^2} \left(\frac{r^2}{4\lambda z} \right)^m \int_0^{\infty} e^{-t} t^{m-1} dt \right]$$

$$= -\frac{kTq_0^2\lambda}{8\pi K_1} \left[\gamma + \ln(\lambda z q_{max}^2) + E_1(\lambda z q_{max}^2) - \sum_{m=1}^{\infty} \frac{(-1)^m}{m\, m!} \left(\frac{r^2}{4\lambda z} \right)^m \right]$$

$$= -\eta \left[2\gamma + \ln(\lambda z q_{max}^2) + E_1(\lambda z q_{max}^2) + \ln\left(\frac{r^2}{4\lambda z} \right) + E_1\left(\frac{r^2}{4\lambda z} \right) \right]$$

where $\eta = kTq_0^2\lambda/(8\pi K_1)$ and $\gamma = 0.5772156649\ldots$ is Euler's constant.

Thus the correlation function is

$$\mathcal{G}(\boldsymbol{r}) = e^{-2\gamma\eta}\left[\frac{4}{q_{max}^2(x^2+y^2)}\right]^{\eta} e^{-\eta E_1\left(\frac{x^2+y^2}{4\lambda z}\right)} \tag{4a}$$

$$= e^{-2\gamma\eta}\left[\frac{4}{q_{max}^2(x^2+y^2)}\right]^{\eta} \text{ for } z=0 \tag{4b}$$

$$= e^{-\gamma\eta}\frac{1}{|q_{max}^2\lambda z|^{\eta}} \text{ for } x^2+y^2=0 \tag{4c}$$

This gives the structure factor $\mathcal{S}(q_x,\, q_y,\, q_z)$ proportional to

$$e^{-2\gamma\eta}\int_{\infty}^{\infty} e^{iq_x x}dx \int_{\infty}^{\infty} e^{iq_y y}dy \int_{\infty}^{\infty} e^{i(q_z-q_0)z}dz \left(\frac{1}{x^2+y^2}\right)^{\eta} e^{-\eta E_1\left(\frac{x^2+y^2}{4\lambda z}\right)}$$

$$= 8e^{-2\gamma\eta}\int_0^{\infty}\cos(q_x x)\,dx \int_0^{\infty}\cos(q_y y)\,dy \int_0^{\infty}\cos[(q_z-q_0)z]\,dz\,\frac{e^{-\eta E_1\left(\frac{x^2+y^2}{4\lambda z}\right)}}{(x^2+y^2)^{\eta}} \tag{5a}$$

If we change to cylindrical coordinates, $r^2 = x^2+y^2$, the integration over the azimuthal angle θ can be done to get:

$$\mathcal{S}(\boldsymbol{q}) \propto 4\pi\, e^{-2\gamma\eta}\int_0^{\infty} r\,dr\,\frac{J_0(q_\perp r)}{r^{2\eta}}\int_0^{\infty}\cos[(q_{\|}-q_0)z]\,dz\,e^{-\eta E_1\left(\frac{r^2}{4\lambda z}\right)} \tag{5b}$$

so that for $q_x = q_y = 0$, by setting $\beta^2 = r^2\,|q_{\|}-q_0|\,/\lambda$ and $|q_{\|}-q_0|\,z = \alpha$, we find

$$\mathcal{S}(0,\,0,\,q_{\|}) \propto 4\pi\, e^{-2\gamma\eta}\frac{\lambda^{1-\eta}}{|q_{\|}-q_0|^{2-\eta}}\int_0^{\infty}\beta^{1-2\eta}d\beta\int_0^{\infty}\cos\alpha\; e^{-\eta E_1\left(\frac{\beta^2}{4\alpha}\right)}d\alpha$$

$$\propto |q_{\|}-q_0|^{-2+\eta} \tag{6}$$

Similarly when $q_{\|} = q_0$, by setting $\beta = rq_\perp$ and $q_\perp^2\lambda z = \alpha$, we obtain

$$\mathcal{S}(q_x,\,q_y,\,q_0) \propto 4\pi\, e^{-2\gamma\eta}\frac{1}{\lambda q_\perp^{4-2\eta}}\int_0^{\infty}\beta^{1-2\eta}J_0(\beta)d\beta\int_0^{\infty} e^{-\eta E_1\left(\frac{\beta^2}{4\alpha}\right)}d\alpha$$

$$\propto q_\perp^{-4+2\eta} = (q_x^2+q_y^2)^{-2+\eta} \tag{7}$$

If we fix the magnitude of $\boldsymbol{q}$ but allow it to range over all orientations, we may use Eq. (5b) to calculate the scattering that would be observed for a powder sample as:

$$\mathcal{S}(q) \propto 2\pi\, e^{-2\gamma\eta}\int_0^{\pi}\sin\theta\,d\theta\int_0^{\infty} r\,dr\,\frac{J_0(qq_0 r\sin\theta)}{r^{2\eta}}\int_0^{\infty}\cos[(q\cos\theta-1)q_0 z]\,e^{-\eta E_1\left(\frac{r^2}{4\lambda z}\right)}dz \tag{8a}$$

$$= 2\pi\, e^{-2\gamma\eta}\int_{-1}^{1}dt\int_0^{\infty} r\,dr\,\frac{J_0(qq_0 r\sqrt{1-t^2})}{r^{2\eta}}\int_0^{\infty}\cos[(qt-1)q_0 z]\,e^{-\eta E_1\left(\frac{r^2}{4\lambda z}\right)}dz \tag{8b}$$

where $q = |\boldsymbol{q}|\,/q_0$.

For computational purposes it may be helpful to put all quantities in dimensionless form. This can be done with the following substitutions: $\rho = q_0 r$, $\zeta = q_0 z$, $\ell = q_0 \lambda$, and retaining $q = |\boldsymbol{q}| / q_0$. When these substitutions are made, we find

$$\mathcal{S}(q) \propto \frac{2\pi\, e^{-2\gamma\eta}}{q_0^{3-2\eta}} \int_{-1}^{1} dt \int_0^\infty \rho\, d\rho\, \frac{J_0(q\rho\sqrt{1-t^2})}{\rho^{2\eta}} \int_0^\infty \cos[(qt-1)\zeta]\, e^{-\eta E_1\left(\frac{\rho^2}{4\ell\zeta}\right)} d\zeta \tag{9a}$$

$$\propto \int_0^\infty \rho^{1-2\eta}\, d\rho \int_0^\infty e^{-\eta E_1\left(\frac{\rho^2}{4\ell\zeta}\right)} d\zeta \int_{-1}^{1} J_0(q\rho\sqrt{1-t^2})\, \cos[(qt-1)\zeta]\, dt \tag{9b}$$

$$= 2\int_0^\infty \cos(\zeta)\, d\zeta \int_0^\infty \rho\, d\rho \left[\frac{1}{\rho^2} e^{-E_1\left(\frac{\rho^2}{4\ell\zeta}\right)}\right]^\eta \int_0^1 J_0(q\rho\sqrt{1-t^2})\, \cos(q\zeta t)\, dt \tag{9c}$$

Eq. (9c) can be used to do a numerical integration to calculate the line shape for a powder sample with very high spectrometer resolution. There are two parameters: η and ℓ.

Consider:

$$\begin{aligned} &2\cos(\zeta) \int_0^1 J_0(q\rho\sqrt{1-t^2})\, \cos(q\zeta t)\, dt \\ &= \int_{-\pi}^{\pi} J_0(q\rho\sin\theta)\, [\cos(\zeta)\, \cos(q\zeta\cos\theta) + \sin(\zeta)\, \sin(q\zeta\cos\theta)]\, \sin\theta\, d\theta \end{aligned} \tag{10}$$

From G&R 8.514.5, 8.514.6, 8.440, and 1.320.3:

$$\cos(q\zeta\cos\theta) = J_0(q\zeta) + 2\sum_{k=1}^{\infty} (-1)^k\, J_{2k}(q\zeta)\, \cos(2k\theta) \tag{11a}$$

$$\sin(q\zeta\cos\theta) = 2\sum_{k=0}^{\infty} (-1)^k\, J_{2k+1}(q\zeta)\, \cos[(2k+1)\theta)] \tag{11b}$$

$$J_0(q\rho\sin\theta)\, \sin\theta = \sin\theta \sum_{n=0}^{\infty} \frac{(-1)^n}{n!\, n!} \left(\frac{q\rho}{2}\right)^{2n} \sin^{2n}\theta \tag{11c}$$

$$\sin^{2n+1}\theta = \frac{1}{2^{2n}} \sum_{m=0}^{n} \frac{(-1)^{n+m}(2n+1)!}{(2n-m+1)!\, m!} \sin[(2n-2m+1)\theta] \tag{11d}$$

$$J_0(q\rho\sin\theta)\, \sin\theta = \sum_{n=0}^{\infty} \frac{1}{2^{2n}(n!)^2} \left(\frac{q\rho}{2}\right)^{2n} \sum_{m=0}^{n} \frac{(-1)^m(2n+1)!}{(2n-m+1)!\, m!} \sin[(2n-2m+1)\theta] \tag{11e}$$

It is clear that the $\cos(q\zeta\cos\theta)$ term in Eq. (10) contributes nothing, while from the $\sin(q\zeta\cos\theta)$ term we obtain π whenever $n - m - k = 0$. So Eq. (10) becomes:

$$2\pi\sin(\zeta) \sum_{n=0}^{\infty} \frac{(-1)^n}{2^{2n}(n!)^2} \left(\frac{q\rho}{2}\right)^{2n} \sum_{m=0}^{n} \frac{(2n+1)!}{(2n-m+1)!\, m!} J_{2n-2m+1}(q\zeta) \tag{12}$$

which should converge fairly rapidly.

Following this, the powder structure factor of Eq. (9c) becomes

$$\mathcal{S}(q) \propto 2\pi \int_0^\infty \sin(\zeta)\, d\zeta \int_0^\infty \rho\, d\rho \times \left\{ \left[\frac{1}{\rho^2}\, e^{-E_1\left(\frac{\rho^2}{4\ell\zeta}\right)} \right]^\eta \sum_{n=0}^{\infty} \frac{(-1)^n}{(n!)^2} \left(\frac{q\rho}{4}\right)^{2n} \sum_{m=0}^{n} \frac{(2n+1)!}{(2n-m+1)!\, m!} J_{2n-2m+1}(q\zeta) \right\} \tag{13a}$$

$$= 2\pi \int_0^\infty \sin(\zeta)\, d\zeta \int_0^\infty \rho\, d\rho \times \left\{ \left[\frac{1}{\rho^2}\, e^{-E_1\left(\frac{\rho^2}{4\ell\zeta}\right)} \right]^\eta \sum_{k=0}^{\infty} J_{2k+1}(q\zeta) \sum_{n=k}^{\infty} \frac{(-1)^n (2n+1)!}{(n!)^2 (n+k+1)!\,(n-k)!} \left(\frac{q\rho}{4}\right)^{2n} \right\} \tag{13b}$$

However a little playing with this expression showed that the series did not compute very well, largely because of large terms of alternating sign. A more sensible approach would be to start with the momentum space function for a powder pattern, namely $\delta(q - q_1)$, and find its Fourier transform:

$$\frac{1}{(2\pi)^3} \int_0^\infty q^2\, \delta(q - q_1)\, dq \int_0^{2\pi} d\phi \int_{-\pi}^{\pi} e^{-iqr\cos\theta}\, d\theta = \frac{q_1^2}{2\pi^2} \frac{\sin q_1 r}{q_1 r}$$

thus convolving Eq. (5a) with $\delta(q - q_1)$ is the same as multiplying $\mathcal{G}(\mathbf{r})$ by $(\sin q_1 r)/(q_1 r)$, with $r = \sqrt{x^2 + y^2 + z^2}$, before taking the Fourier transform.

Now the scattered intensity is the convolution of $\mathcal{S}(\boldsymbol{q})$ with the instrumental resolution function. Since the Fourier transform of $\mathcal{S}(\boldsymbol{q})$ is $\mathcal{G}(\boldsymbol{r})$, which is known, the simplest way to calculate the scattering $\mathcal{I}(\boldsymbol{q})$ is to transform the resolution function to real space, multiply it by $\mathcal{G}(\boldsymbol{r})$, and transform back. If we let $\mathcal{R}(\boldsymbol{r})$ be the real space transform of the resolution function, we find

$$\mathcal{I}(\boldsymbol{q}) \propto e^{-2\gamma\eta} \int_{\infty}^{\infty} e^{iq_x x} dx \int_{\infty}^{\infty} e^{iq_y y} dy \int_{\infty}^{\infty} e^{i(q_z - q_0)z} dz \; \mathcal{R}(\boldsymbol{r}) \left[\frac{1}{x^2+y^2} \, e^{-E_1\left(\frac{x^2+y^2}{4\lambda z}\right)} \right]^{\eta} \tag{14}$$

We consider some simple cases.

First, if the spectrometer selects only $\boldsymbol{q} = q_{\|}\,\mathbf{1}_z$, $\mathcal{R}(\boldsymbol{q})$ is $\delta(q_x)\,\delta(q_y)\,\delta(q_z - q_{\|})$ and $\mathcal{R}(\boldsymbol{r}) = (2\pi)^{-3}\exp(-iq_{\|}z)$. The integrand $\mathcal{G}(\mathbf{r})$ is an even function of x, y, z, so the result becomes

$$\mathcal{I}(\boldsymbol{q}) \propto \int_{0}^{\infty} \cos(q_x x)\, dx \int_{0}^{\infty} \cos(q_y y)\, dy \int_{0}^{\infty} \cos(q_z - q_0)z \, dz \; \mathcal{R}(\boldsymbol{r}) \left[\frac{1}{x^2+y^2} \, e^{-E_1\left(\frac{x^2+y^2}{4\lambda z}\right)} \right]^{\eta} \tag{15}$$

The spectrometer resolution function used for the Risø measurements on 8OCB was gaussian (representing slits) in the transverse directions, while an exponential fall off convolved with a gaussian was a good representation for the longitudinal resolution. The real space resolution function was

$$\mathcal{R}(\boldsymbol{r}) = \frac{1}{(2\pi)^3} \, \frac{e^{-\sigma_z^2 z^2/2}}{1+Q^2z^2} \, e^{-\sigma_x^2 x^2/2} \, e^{-\sigma_y^2 y^2/2} \tag{16}$$

which corresponds to momentum space resolutions of $(2\pi\sigma_z^2)^{1/2}\, e^{-q_z^2/(2\sigma_z^2)} \otimes e^{-q_z/Q}$ in the q_z direction, $(2\pi\sigma_x^2)^{1/2}\, e^{-q_x^2/(2\sigma_x^2)}$ in q_x, and $(2\pi\sigma_y^2)^{1/2}\, e^{-q_y^2/(2\sigma_y^2)}$ in q_y. Using this $\mathcal{R}(\mathbf{r})$, one gets

$$\begin{aligned} \mathcal{I}(\boldsymbol{q}) \propto e^{-2\gamma\eta} \int_{0}^{\infty} e^{-\sigma_x^2 x^2/2} \cos(q_x x) \int_{0}^{\infty} e^{-\sigma_y^2 y^2/2} \cos(q_y y) \int_{0}^{\infty} \frac{e^{-\sigma_z^2 z^2/2}}{1+Q^2z^2} \cos(q_z - q_0)z \\ \left[\frac{1}{x^2+y^2} \, e^{-E_1\left(\frac{x^2+y^2}{4\lambda z}\right)} \right]^{\eta} dx\, dy\, dz \end{aligned} \tag{17}$$

To use this in numerical calculations, it is useful to put things into dimensionless form. So put $x_1 = \sigma_x x/\sqrt{2}$, $y_1 = \sigma_y y/\sqrt{2}$, $z_1 = \sigma_z z/\sqrt{2}$, $F = \sqrt{2}Q/(q_0\,\sigma_z')$, $\lambda' = \lambda q_0$, $\sigma_x' = \sigma_x/q_0$, $\sigma_y' = \sigma_y/q_0$, $\sigma_z' = \sigma_z/q_0$, $q_x' = q_x/q_0$, $q_y' = q_y/q_0$, and $q_z' = (q_z - q_0)/q_0$. These give

$$\begin{aligned} \mathcal{I}(\boldsymbol{q}) \propto e^{-2\gamma\eta} \int_{0}^{\infty} e^{-x_1^2} \cos\left(\frac{\sqrt{2}x_1\, q_x'}{\sigma_x'}\right) \int_{0}^{\infty} e^{-y_1^2} \cos\left(\frac{\sqrt{2}y_1\, q_y'}{\sigma_y'}\right) \int_{0}^{\infty} \frac{e^{-z_1^2}}{1+F^2z_1^2} \cos\left(\frac{\sqrt{2}z_1\, q_z'}{\sigma_z'}\right) \\ \left[\frac{1}{\left(\frac{x_1}{\sigma_x'}\right)^2 + \left(\frac{y_1}{\sigma_y'}\right)^2} \, e^{-E_1\left(\frac{\sigma_z'}{2\sqrt{2}\lambda' z_1}\left[\left(\frac{x_1}{\sigma_x'}\right)^2 + \left(\frac{y_1}{\sigma_y'}\right)^2\right]\right)} \right]^{\eta} dx_1\, dy_1\, dz_1 \end{aligned} \tag{18}$$

One way to include the effect of a finite sample size is to limit the region of space integrated over in calculating $\mathcal{S}(\mathbf{q})$ from $\mathcal{G}(\mathbf{r})$. Thus Eg. (18) can be used to make an approximate correction for a finite sized sample. If we suppose the effects of the finite sample size can be represented as a gaussian cutoff, the result will be given by Eq. (18). Let us suppose a "sample size" given by a spherical gaussian, $\exp -(x^2+y^2+z^2)/L^2$. Then, if $L' = q_0 L$, we would have

$$\begin{aligned}
\mathcal{I}(\boldsymbol{q}) &\propto e^{-2\gamma\eta} \int_0^\infty e^{-x_1^2} \cos(x_1\, q'_x\, L') \int_0^\infty e^{-y_1^2} \cos(y_1\, q'_y\, L') \int_0^\infty e^{-z_1^2} \cos(z_1\, q'_z\, L') \\
&\quad \left[\frac{1}{x_1^2+y_1^2}\, e^{-E_1\left(\frac{(x_1^2+y_1^2)L'}{4\lambda' z_1}\right)} \right]^\eta dx_1\, dy_1\, dz_1 \\
&= \frac{e^{-2\gamma\eta}}{8} \int_{-\infty}^\infty e^{-x_1^2}\, e^{ix_1\, q_x\, L} \int_{-\infty}^\infty e^{-y_1^2}\, e^{iy_1\, q_y\, L} \int_{-\infty}^\infty e^{-z_1^2}\, e^{iz_1\,(q_z - q_0)\,L} \\
&\quad \left[\frac{1}{x_1^2+y_1^2}\, e^{-E_1\left(\frac{(x_1^2+y_1^2)L}{4\lambda z_1}\right)} \right]^\eta dx_1\, dy_1\, dz_1 \\
&= \frac{e^{-2\gamma\eta}}{8} \int_0^\infty r_1^2\, e^{-r_1^2}\, dr_1 \int_0^{2\pi} d\phi \int_{-\pi}^{\pi} \sin\theta\, d\theta \left[\frac{1}{r_1^2 \sin^2\theta}\, e^{-E_1\left(\frac{r_1 L \sin^2\theta}{4\lambda\cos\theta}\right)} \right]^\eta \\
&\quad \exp i\{q\, L\, r_1[\sin\theta\, \sin\vartheta\, \cos(\phi-\varphi) + \cos\theta\, \cos\vartheta] - q_0\, L\, r_1\, \cos\theta\} \\
&= \frac{\pi}{2}\, e^{-2\gamma\eta} \int_0^\infty r_1^2\, e^{-r_1^2}\, dr_1 \int_0^{\pi} \sin\theta\, d\theta \left[\frac{1}{r_1^2 \sin^2\theta}\, e^{-E_1\left(\frac{r_1 L \sin^2\theta}{4\lambda\cos\theta}\right)} \right]^\eta \\
&\quad J_0(q\, L\, r_1\, \sin\theta\, \sin\vartheta) \cos(q\, L\, r_1\, \cos\theta\, \cos\vartheta - q_0\, L\, r_1\, \cos\theta)
\end{aligned} \tag{19}$$

where θ, ϕ are the co-latitude and azimuth for $\mathbf{r}_1$, and ϑ, φ are the co-latitude and azimuth for $\mathbf{q}$. Because of the azimuthal symmetry it was possible to integrate over ϕ in Eq. (19) and obtain the Bessel function. For an aligned sample, we can chose an orientation for $\mathbf{q}$ by specifying ϑ. If we replace $\cos\theta$ by x and r_1 by r, we obtain the integral:

$$\begin{aligned}
\mathcal{I}(\mathbf{q}) &\propto \frac{\pi}{2}\, e^{-2\gamma\eta} \int_0^1 dx \int_0^\infty r^2\, e^{-r^2}\, dr \left[\frac{1}{r^2(1-x^2)}\, e^{-E_1\left(\frac{rL(1-x^2)}{4\lambda x}\right)} \right]^\eta \\
&\quad J_0(q\, L\, r\, \sqrt{1-x^2}\, \sin\vartheta)\, \cos(q\, L\, r\, x\, \cos\vartheta - q_0\, L\, r\, x)
\end{aligned} \tag{20}$$

If we had a powder aligned sample, we should integrate over all orientations of $\mathbf{q}$ to get, where y is $\cos\vartheta$:

$$\begin{aligned}
\mathcal{I}(\mathbf{q}) &\propto \frac{\pi}{8}\, e^{-2\gamma\eta} \int_{-1}^1 dx \int_0^\infty r^2\, e^{-r^2}\, dr \left[\frac{1}{r^2(1-x^2)}\, e^{-E_1\left(\frac{rL(1-x^2)}{4\lambda x}\right)} \right]^\eta \\
&\quad e^{-iq_0\, L\, r\, x} \int_{-1}^1 dy\, J_0\left(q\, L\, r\, \sqrt{(1-x^2)(1-y^2)}\right)\, e^{iq\, L\, r\, x\, y} \\
&= \frac{\pi}{2}\, e^{-2\gamma\eta} \int_0^1 dx \int_0^\infty r^2\, e^{-r^2}\, dr \left[\frac{1}{r^2(1-x^2)}\, e^{-E_1\left(\frac{rL(1-x^2)}{4\lambda x}\right)} \right]^\eta \\
&\quad \cos(q_0\, L\, r\, x) \int_0^1 dy\, J_0\left(q\, L\, r\, \sqrt{(1-x^2)(1-y^2)}\right)\, \cos(q\, L\, r\, x\, y)
\end{aligned} \tag{21}$$

The integral over y can be done using 6.677.6 of G&R (p 737), to get:

$$\mathcal{I}(\mathbf{q}) \propto \int_0^1 dx \int_0^\infty r^2\, e^{-r^2}\, dr \left[\frac{1}{r^2(1-x^2)}\, e^{-E_1\left(\frac{rL(1-x^2)}{4\lambda x}\right)}\right]^\eta \frac{\sin(q\,L\,r)\,\cos(q_0\,L\,x\,r)}{q\,L\,r} \tag{22}$$

Eq. (20) and Eq. (22) are in a form that might be tractable by numerical means in a data fitting program. Or, the order of integration in Eq. (22) might be reversed for numerical calculations

$$\mathcal{I}(\mathbf{q}) \propto \frac{1}{qL} \int_0^\infty r\, e^{-r^2}\, \sin(q\,L\,r)\, dr \int_0^1 \left[\frac{1}{r^2(1-x^2)}\, e^{-E_1\left(\frac{rL(1-x^2)}{4\lambda x}\right)}\right]^\eta \cos(q_0\,L\,x\,r)\, dx \tag{23}$$

To get an idea of the effect of sample size L on the scattering, we might consider the integral

$$\mathcal{I}_a(\mathbf{q}) = \frac{1}{qL} \int_0^\infty r\, e^{-r^2}\, \sin(q\,L\,r)\, dr \int_0^1 \cos(q_0\,L\,x\,r)\, dx \tag{24}$$

The integral over x can be done immediately, and the remaining one over r is given in G&R 3.896.4. One finds

$$\mathcal{I}_a(\mathbf{q}) = \frac{\sqrt{\pi}}{4}\, \frac{\sinh(q_0^2\,L^2\,X/2)}{q_0^2\,L^2\,X/2}\, e^{-q_0^2\,L^2\,(1+X^2)/4} \tag{25}$$

where $X = q/q_0$. The resulting *Mathematica* output, normalized to the peak height at $X = 1$, is shown below.

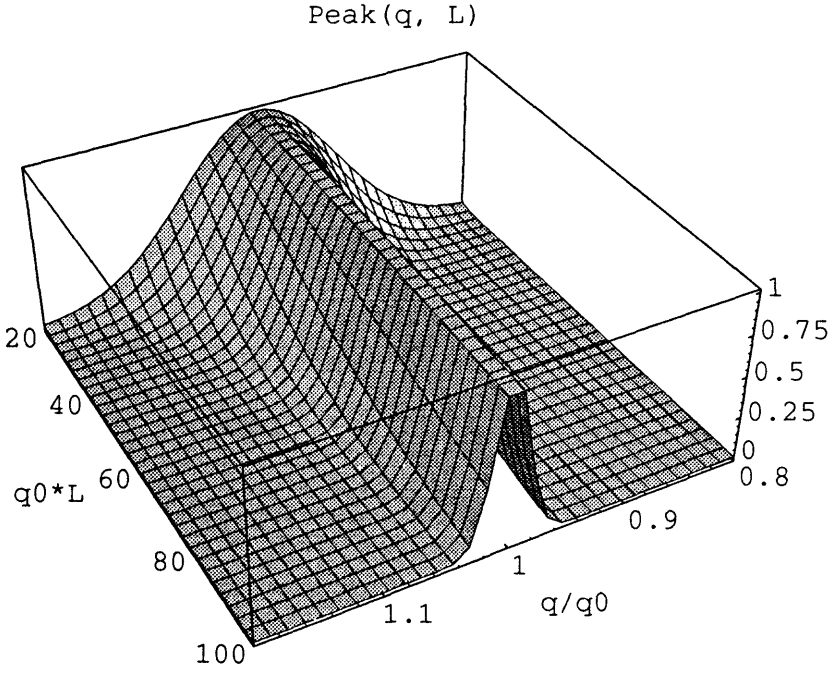

It appears as if the sharpness of the data is going to require $q_0 L > 100$, so that the $\sin(q L r)\cos(q_0 L r x)$ term is going to oscillate rapidly compared to changes in remainder of the integrand in Eq. (22), which is plotted below:

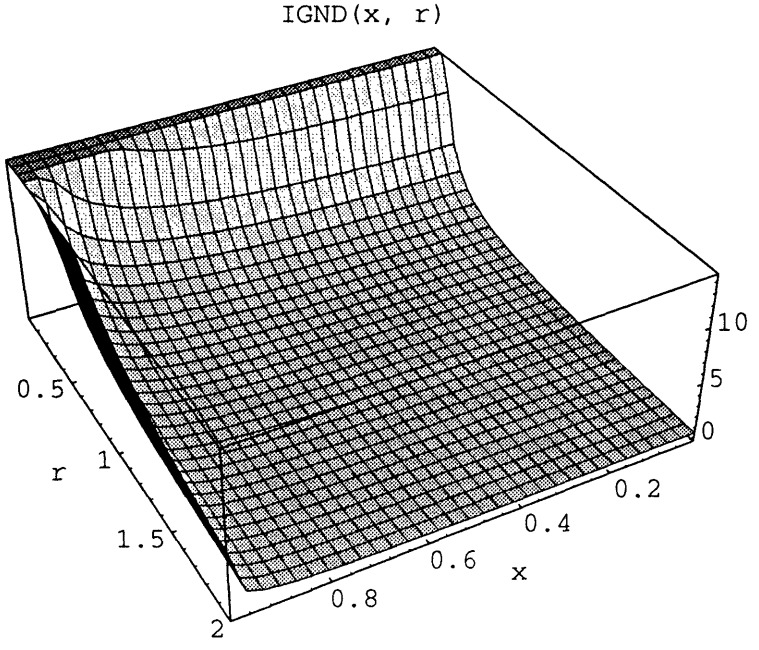

The oscillating part of the integrand in Eq. (22), $\sin(q L r)\cos(q_0 L x r)$, is plotted below for $q L = 10$ and $q_0 L = 20$. Since the useful values of $q_0 L$ for Chao's data appear to be around 300, the impracticality of a brute force numerical integration becomes clear.

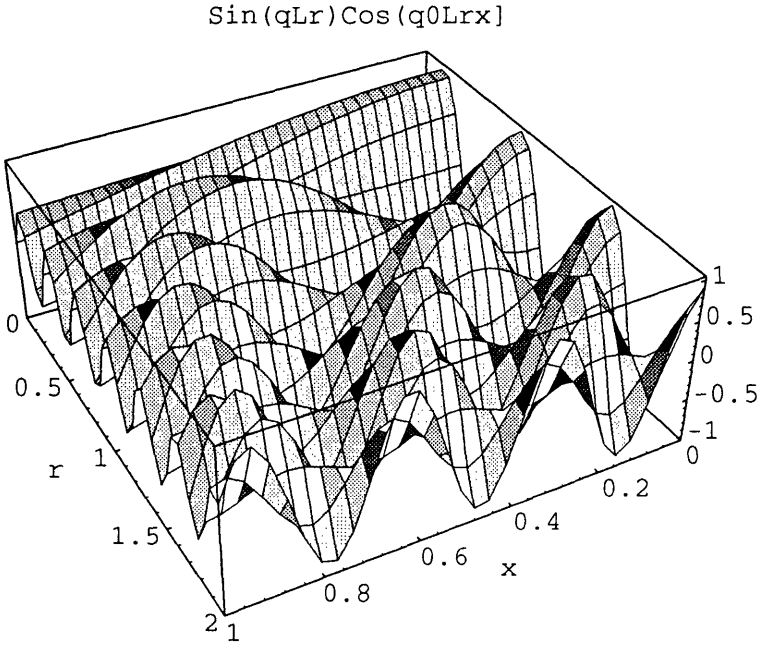

A simple thing to try is to assume the infinite sized sample would give a power law, say

$$\mathcal{I}(q) = \frac{1}{\mid q \mid^{\varphi}}$$

This would have a one dimensional Fourier transform, provided $0 < \varphi < 1$, given by:

$$\mathcal{G}(z) = \frac{1}{2\pi} \int_{-\infty}^{\infty} \frac{e^{iq\,z}}{\mid q \mid^{\varphi}}\, dq = \frac{\Gamma(1-\varphi)}{\pi \mid z \mid^{1-\varphi}} \cos\left(\frac{(1-\varphi)\pi}{2}\right)$$

where G&R 3.761.9 has been used. We could transform this back to $\mathcal{I}(q)$, but with a gaussian cutoff of the form $\exp -z^2/L^2$. That gives, using G&R 3.952.8:

$$\begin{aligned}
\int_{-\infty}^{\infty} \mid z \mid^{\varphi-1}\ e^{-z^2/L^2}\, e^{-iqz}\, dz &= 2\int_0^{\infty} x^{\varphi-1}\, e^{-z^2/L^2}\, \cos(qz)\, dz \\
&= \Gamma(\varphi/2)\, L^{\varphi}\, {}_1F_1\left(\frac{\varphi}{2};\, \frac{1}{2};\, -\frac{q^2L^2}{4}\right) \\
&= \Gamma(\varphi/2)\, L^{\varphi}\, M\left(\frac{\varphi}{2};\, \frac{1}{2};\, -\frac{q^2L^2}{4}\right) \qquad (26)
\end{aligned}$$

where M is the Kummer function [J. Spanier and K. B. Oldham, *An Atlas of Functions*, Hemisphere, New York, 1987], also called a degenerate hypergeometric function. Thus we may fit our data to something like:

$$\mathcal{I}(q) \propto M\left(\frac{\varphi}{2};\, \frac{1}{2};\, -\frac{(q-q_0)^2L^2}{4}\right) \qquad (27)$$

This requires $\varphi < 1$; otherwise there is a singularity at the origin one can't integrate across.

Bibliography

[1] R. Strey, R. Schomacher, D. Roux, F. Nallet, and U. Olsson, J. Chem. Soc. Faraday Trans. II **86**, 2253 (1990).

[2] J.N. Israelachvili *Intermolecular and Surface Forces*, Academic Press, New York, 1985, Chapter 15.

[3] D. Roux and M.E.Cates, *Proceedings of the 4th Nishinomyia-Yukawa Symposium* Springer Verlag.

[4] P.Snabre and G.Porte, Europhys. Lett., **13(7)**, 641(1990).

[5] E.W.Kaler, A.K.Murthy, B.E. Rodriguez and J.A.Zasadzinski, Science, **245**, 1371(1989).

[6] W. Helfrich, Z. Naturforsch **33a**, 305 (1978).

[7] F. Brochard and P.G. de Gennes, Pramana, Suppl. No. **1**, 1 (1975).

[8] J. Als-Nielsen, J.D. Litster, R.J. Birgeneau, M. Kaplan, C.R. Safinya, A. Lindegaard-Anderson and S. Mathiesen, Phys. Rev. B**22**, 312(1979).

[9] J.Marignan, A.Delichere and F. C.Larche, J. Phys. Lett. France **44**, L-609(1983).

[10] F.C. Larche, S. El Qebbaj, and J. Marignan, J. Phys. Chem. **90**, 707 (1986).

[11] F.C. Larche, J. Appell, G. Porte, P. Bassereau, and J. Marignan, Phys. Rev. Lett. **56**, 1700 (1986).

[12] A. M. Bellocq and D. Roux, *Microemulsions: Structure and Dynamics*, Stig E. Friberg and Pierre Bothorel Eds. (CRC Press, 1987).

[13] Science **198**, 293(1977).

[14] D. Roux and C.R. Safinya, J. Phys. (Paris) **49**, 307(1988).

[15] F. Nallet, D. Roux, and J. Prost, J. Phys. **50**, 3147 (1989).

[16] T.C. Lubensky, J. Prost, and S. Ramaswamy, J. Phys. **50**, 3147 (1989).

[17] M. Born, E. Wolf, *Principles of Optics*, Pergamon, New York, Third Edition.

[18] J.D. Litster, *Basic Formulae for Light Scattering*, Private Communication.

[19] B. Berne, R. Pecora, Chapter 4 *Dynamic Light Scattering, with Applications to Chemistry, Biology, and Physics*, Wiley-Interscience, New York, 1976.

[20] R. Pecora, *Dynamic Light Scattering, Applications of Photon Correlation Spectroscopy*, Plenum, New York, 1985.

[21] B. Berne, R. Pecora, Chapter 10 *Dynamic Light Scattering, with Applications to Chemistry, Biology, and Physics*, Wiley-Interscience, New York, 1976.

[22] C. Y. Zhang, S. Sprunt and J. D. Litster, Phys. Rev. E **48**, 2850(1993).

[23] J. Biais, P. Bothorel, B. Clin, P. Lalanne, J. Dispersion Sci. Techonology **2(1)**, 67(1981).

[24] C. Taupin, L. Auvray, and J.-M. Meglio; chapter 11, *Micellar Solutions and Microemulsions*, S. H. Chen and R.Rajagopalan Eds. (Springer-Verlag, 1990).

[25] L.D. Landau, in *Collected Papers of L.D. Landau*, edited by D.ter Haar (Gordon and Breach, New York, 1965), p.209.

[26] R.E. Peierls, Helv. Phys. Acta Suppl. **7**, 81(1934).

[27] C.R. Safinya, D.Roux, G.S.Smith, S.K.Sinha, P.Dimon, N.A.Clark and A.M.Bellocq, Phys. Rev. Lett. **57**, 2718(1986).

[28] A. Caille, C.R. Acad. Sci. Ser. B **274**, 891(1972).

[29] Abramowitz and Stegun, *A Handbook of Mathematical Functions.*

[30] P. Dutta and S.K. Sinha, Phys. Rev. Lett. **47**, 50(1981).

[31] J. Spanier and K.B. Oldham, *An Atlas of Functions*, Hemisphere, New York, 1987.